Influence of Surface Geometry and Heating on the Flow Structure in Wall-Bounded Flows

Shivani Tara Gajusingh

A Thesis

in

The Department

of

Mechanical and Industrial Engineering

Presented in Partial Fulfillment of the Requirements
for the Degree of Master of Applied Science (Mechanical Engineering) at
Concordia University
Montreal, Quebec, Canada

December 2006

Your file Votre référence
ISBN: 978-0-494-28937-2
Our file Notre référence
ISBN: 978-0-494-28937-2

Abstract

Influence of Surface Geometry and Heating on the
Flow Structure in Wall-Bounded Flows

Shivani Tara Gajusingh

The present research is aimed at improving the knowledge and understanding of the physical processes that control heat transfer across the solid-fluid interface, which is very important in order to develop efficient heat exchangers. To achieve this objective, the research has been divided into three phases, which investigated the fundamental physical phenomena from different aspects.

The first phase provided the first detailed investigation of the impact of different wall roughness on the turbulent properties in a smooth channel. The results show the different wall roughness has significant effects on the mean streamwise velocity and Reynolds stress distribution. For other turbulent properties, the enhancement was observed near the rough wall, however, it was restricted to the inner region.

The second phase provided the first quantitative comparison of the mean and turbulent properties in the presence and absence of wall heating under same operating conditions. The results show that both mean and turbulent characteristics are affected by wall heating. The results also showed that an originally laminar flow becomes turbulent with the addition of heat. However for an originally turbulent flow, addition of heat reduces the magnitudes of the mean streamwise velocity and turbulent properties.

The third phase provided the first detailed comparison on the turbulent characteristics with and without a baffle. The results showed a significant enhancement of all turbulent characteristics in the region downstream of the baffle. These results demonstrate that higher turbulence produced by a baffle would be responsible for the enhanced heat transfer rate at the wall.

Acknowledgment

I would like to extend my sincere gratitude to Kamran Siddiqui for his support and guidance over the past two years as my thesis supervisor. His trust and confidence in me has allowed me to accomplish my goals and develop my intuition and knowledge as an engineer. I would also like to thank the members of my examining committee, Georgios Vatistas, Fariborz Haghighat, and Henry Hong, for their suggestions.

I would also like to thank the members of Environmental Thermofluidics research group, Junaid Bukhari, Nasiruddin Shaikh and Majid Nabavi for their help with PIV measurements and Matlab codes. I would like to show my appreciation to the members of Concordia's Machine Shop and technical staff: Brian Cooper, Gilles Huard and Alex Macpherson. Special thanks to Alex Macpherson for his continuous guidance and help with the design and fabrication with my experimental apparatus.

I would like to thank my parents, family and friends for without their support I would not be able to complete my studies. I would specially like to thank Sabrina Poirier for her continuous support throughout my years at Concordia University.

I dedicate this thesis to my parents

whose continuous support has made this possible.

Table of Contents

List of Figures

List of Tables

List of Symbols

C	Specific Heat	(kJ/kg · °C)
Δt	Time separation between two images of an image pair	(ms)
E_K	Mean turbulent kinetic energy	(cm^2/s^2)
h	Heat transfer coefficient	($W/m^2 \cdot °C$)
$\dot{m}$	Mass flow rate	(kg/s)
P	The rate of turbulent kinetic energy production	(cm^2/s^3)
Re	Reynolds Number based on hydraulic diameter	dimensionless
Re_θ	Reynolds Number based on momentum thickness	dimensionless
Re_τ	Reynolds Number based on friction velocity	dimensionless
Ri	Gradient Richardson number	dimensionless
St	Stanton Number $St = \frac{h}{\rho C U_\infty}$	dimensionless
u	Streamwise component of the instantaneous velocity	(cm/s)
u'	Streamwise component of the turbulent velocity	(cm/s)
u_*	Friction velocity	(cm/s)
U	Mean streamwise velocity	(cm/s)
U_∞	Freestream velocity	(m/s)
w	Vertical component of the instantaneous velocity	(cm/s)
w'	Vertical component of the turbulent velocity	(cm/s)
x	Horizontal axis	(cm)
z	Vertical axis	(cm)

Greek Symbols

δ	Boundary layer thickness	(cm)
ε	The rate of turbulent kinetic energy dissipation	(cm^2/s^3)
ν	Kinematic viscosity of water	(cm^2/s)

θ	Momentum thickness	(cm)
ρ	Density	(kg/m^3)
ω'	Turbulent vorticity	(s^{-1})

Subscripts

w	water
p	particle

Chapter 1 - Introduction

The performance of energy utilizing systems plays an important role in contributing to the greenhouse gas emissions. Any improvement in these systems would reduce energy consumption and hence cut down gas emissions. Heat exchangers are used in a wide range of engineering applications, such as power generation, auto and aerospace industry, electronics, and HVAC. The primary function of a heat exchanger is to transfer heat from one fluid to the other efficiently, which in most of the cases are separated by a solid wall. In many applications such as power generation and HVAC, the efficiency of heat exchangers plays an important role in controlling the overall performance of the system. An efficient heat exchanger in such systems could result in the reduced consumption of the energy resource, which would provide both economical and environmental benefits.

Due to the complex nature of flow and the unavailability of advanced instrumentation and measurement techniques, the fundamental heat transfer process between the heat exchanger wall and fluid has not been fully explored and is not well understood. As a result, bulk heat transfer characteristics are used as a criterion to improve the thermal design of heat exchangers, which is an approximate approach. The present research is aimed at improving the knowledge and understanding of the physical processes that control heat transfer across the solid-fluid interface, which is very important in order to develop efficient heat exchangers. To achieve this objective, the research has been divided into three phases, which investigated the fundamental physical phenomena from different aspects. The initial phase of the research examined the simultaneous impact of a wall bounded flow with the top and bottom walls of different surface roughness. The

second phase is focused on the direct impact of wall heating on the flow characteristic in the near wall region. Lastly, the final phase investigated the impact of a single rectangular baffle on the flow structure downstream of the baffle. As these phases investigated the flow and/or thermal behavior involved in the heat exchanger design from different perspectives, the introduction and literature review of each of the three phases has been discussed separately.

1.1 Internal Flows with Walls of Different Wall Roughness

Internal flows are observed in a wide range of engineering applications. In these applications, the flow passes over solid walls of different materials and roughness. The impact of surface roughness on the flow characteristics has been studied extensively over the past several decades. The results showed that the surface roughness has an impact on the wall shear stress and near-surface turbulent properties. However, there is no consensus on the extent from the wall up to which the influence of surface roughness is significant. Townsend (1976) proposed wall similarity hypothesis which states that at sufficiently high Reynolds number, the turbulent flow in the region outside the roughness sublayer is independent of the wall roughness. Some experimental studies supported this hypothesis. For example, Keirsbulck *et al.* (2002) investigated the flow over smooth and rough surfaces and observed that the roughness effect on the turbulent intensities and Reynolds stress were confined to the near-wall region. They also observed that the vertical component of velocity was more sensitive to the wall roughness than the horizontal component. Perry *et al.* (1987) analyzed the turbulent structure in zero-pressure-gradient boundary layer over different surface roughness using spectral analysis.

They found that the turbulent velocity spectra for smooth and rough wall cases support Townsend's (1976) similarity hypothesis. However, there are several other studies which observed that the wall roughness is not restricted to the near-wall inner region, but also extends to the outer region. For example, Krogstad *et al.* (1992) observed that wall roughness influences the mean velocity profile and turbulent stresses into the outer region. They further observed that wall roughness has significant impact on the magnitude of the vertical turbulent intensity, moderate on the Reynolds stress and slight on the horizontal turbulent intensity. Krogstad and Antonia (1999) and Bergstrom *et al.* (2002) also reported that the roughness effects were not limited to the roughness sub-layer but extended into the outer region.

Recently, Bakken *et al.* (2005) studied the effect of Reynolds number in the outer layer over different wall roughness. They observed that the wall effects are restricted to the inner region up to a distance equal to five times the roughness length scale. They argued that the outer layer in a channel could behave differently from a boundary layer. They attributed this behavior to the differences in the outer boundary layer conditions. That is, in a channel flow, the length scales become independent of the streamwise position once the flow is fully developed. This behavior is not observed in a boundary layer where the wall shear stress controls the growth rate in the outer layer. Krogstad *et al.* (2005) and Ashrafian and Andersson (2006) also observed that the effects of different wall roughness are restricted only in the inner region. A common feature in these three studies is that the roughness of both bounding walls was kept the same. Bakken *et al.* (2005) further argued that the deviation from the similarity hypothesis could be due to the reason that in

channels with only one rough surface, the difference in the drag between this rough surface and other relatively smooth surface causes an asymmetry which could affect the outer layer structure. Krogstad *et al.* (2005) attributed the discrepancy in the agreement with the similarity hypothesis to the reason that the surface roughness effects on the outer layer could be dependent on the flow type.

Hanjalic and Launder (1972) experimentally investigated the flow in a channel bounded by walls of different roughness. They observed asymmetry in the mean velocity and turbulent characteristics across the channel in both inner and outer regions. They found that the turbulent shear stress near the rough wall was four times greater than that near the smooth wall. The locations of the maximum mean velocity and zero stress were also shifted towards the smooth wall. They argued that smooth and rough surfaces generate dissimilar flows which interact with each other resulting in strong diffusional transport of turbulent shear stress and kinetic energy from the rough towards the smooth wall. Bhaganagar *et al.* (2004) numerically investigated the effect of different wall roughness in a channel flow. They found that turbulent intensities, turbulent vorticity and turbulent energy budget are influenced by the difference in the wall roughness, however the influence of roughness was restricted to the inner region, except for the turbulent intensities, whose effect was extended to the outer region. Miyake *et al.* (2001) also numerically investigated the effect on different wall roughness on the flow and thermal characteristics in a channel. They found that the influence of roughness on both velocity and thermal fields was restricted to the near wall region. For the turbulent shear stress,

they observed an asymmetry across the channel with the zero stress location shifted towards the smooth wall.

Hanjalic and Launder (1972) and Miyake *et al.* (2001) considered ribs of square cross-section on the rough wall, whereas, Bhaganagar *et al.* (2004) considered roughness elements of "egg-carton" shape. The roughness of the other wall (i.e. the smooth wall) in these studies was almost negligible compared to the size of the roughness element on the rough wall. Thus, the cases considered in these studies, indicated the impact of distinctly smooth and rough surfaces on the flow structure. In many practical applications, the walls of a channel are not necessarily of the same material or roughness. In this case, the flow is bounded by walls of different roughness. Furthermore, in these applications, the roughness is typically natural and not altered by artificial elements. Thus, the actual size of the roughness elements on both surfaces is usually very small, thus, in the absolute terms, both surfaces are considered to be smooth. However, one wall is relatively rougher than the other. The impact of wall roughness on the flow behavior in such situation has not been reported.

1.2 Impact of Wall Heating

Significant work has been done over the past several decades, to understand the internal flows and the flow structure over a solid wall. These studies can broadly be categorized into two groups. The first group is focused on the investigation of the flow structure in an unheated channel or above an unheated wall, with the main emphasis on the impact of wall roughness on the flow structure in the inner and outer layers adjacent to the wall.

This work is outlined in the previous section (section 1.1). The second group is focused on the investigation of the flow and thermal structure when heat is added from the wall. Nicholl (1970) studied the effects of heat on a turbulent boundary layer for stable and unstable stratifications in a wind tunnel. The wall and free stream temperature difference ranged from 20 to 100 °C. He observed that for unstable stratification, the mean velocity and turbulent intensities near the upstream edge of the heated plate are larger in magnitude than that observed further downstream. He argued that when the boundary layer first encounters the heated surface, the interaction of convective layer and boundary layer turbulence induce intense local convective activity, which reduces with the downstream distance. At a distance of 74 cm from the upstream heated edge, he compared the mean and turbulent intensity profiles for heated and unheated conditions and observed no significant difference in the magnitudes. Arya (1975) investigated the effects of buoyancy on the mean and turbulence structure in a developed turbulent flow over a horizontal flat plate. Experiments were conducted for stable, neutral and unstable conditions. He observed that the thickness of the viscous sublayer increased with stability, whereas, the coefficients of skin friction and heat transfer decreased with stability. The turbulent characteristics, however, were presented only for the stably stratified conditions and it was concluded that the turbulence was suppressed with increasing stability. Perry and Hoffman (1976) investigated the flow over a constant temperature wall to determine the scaling laws for the mean and fluctuating temperature and velocities using X–wire probes. They showed that the temperature and velocity profiles correlate well with inner and outer layers scaling. They also observed that the fluctuating properties are more sensitive to the spurious pressure gradients than the mean

flow. Rued *et al.* (1987) conducted experimental and numerical investigation of the flow in a square channel with one heated wall. The velocity field was measured using laser Doppler anemometry. Their study was focused on the effects of wall intersections (i.e. the corner effects) on the flow and heat transfer. They observed an increase in the Nusselt number in the corner region of the channel where the heated and unheated walls intersect. They attributed this enhanced heat transfer to non-symmetry and anisotropy at the corner and the proximity of the unheated wall.

Fukui and Nakajima (1985) investigated the impact of unstable thermal stratification on the flow and thermal structure in the wall region. They measured velocity and temperature fluctuations in the wall region of fully-developed turbulent flow between horizontal parallel plates for a range of Reynolds and Richardson numbers. They found that in the inner region, the normalized horizontal velocity fluctuations increased with an increase in the Richardson number. The opposite trend was observed for the vertical velocity fluctuations in the inner region. That is, the normalized velocity magnitude decreased with an increase in the Richardson number. In the outer region, the horizontal velocity fluctuations collapsed for all cases, whereas, the trend of the vertical velocity fluctuations was reversed. That is, the vertical velocity magnitude increased with the Richardson number. They concluded that during unstable stratification, the dependency of the turbulent intensities differ in the inner and outer regions. They also observed that unstable stratification has no effect on the temperature fluctuation in the inner region but the magnitude of temperature fluctuations decreased with the Richardson number in the outer region.

Hirota *et al.* (1997) measured velocity and temperature in a square duct using hot-wire probes for fully turbulent flow at a single Reynolds number. Their investigation was focused on the flow structure in the plane normal to the flow direction. Based on the comparison of mean and fluctuating velocities for heated and unheated cases, they concluded that heat addition has no significant influence on the flow properties in this plane. They also observed that the eddy diffusivity for the heated case is higher than the unheated case in the middle of the channel and which become comparable near the wall. They also suggested that the influence of secondary flow on heat transport is weaker than that on the momentum transport. Ichimiya and Yamada (2005) numerically investigated the flow structure in a square duct for both thermally insulated walls and uniform temperature walls. They also studied the velocity field in a plane normal to the direction of the flow. Similar to Hirota *et al.* (1997), they observed that buoyancy influences the secondary flow development in the downstream direction.

In spite of several studies describing the flow structure above the heated wall, the question as to how the addition of heat affects the flow structure has not been well established to date. A direct comparison between the flow properties in the presence and absence of wall heating would provide a better insight into the impact of wall heating on the flow structure. In most of the previous studies however, the flow structure was investigated either in the absence or presence of heat, and no such comparison was made. Nicholl (1970) conducted such comparison for mean and turbulent intensity profiles; however, he did not observe any appreciable difference.

1.3 Influence of a Baffle

As mentioned previously, heat exchangers are used in a wide range of engineering applications. An enhancement of heat transfer between the two fluids would therefore result in a more efficient heat exchanger. This can be achieved by improving the thermal contact of the heat exchanger fluid with the wall by increasing the surface heat transfer coefficient, which is typically done by manipulating the heat transfer surface. Examples of manipulated surfaces include treated surfaces, rough surfaces, extended surfaces, coiled tubes, surface vibration, fluid vibration, jet impingement and vortex generators. Previous studies have shown that the vortex generator is an effective mean of increasing the surface heat transfer. The vortex generator is basically a solid object attached to the wall that obstructs the flow. The vortex generator causes flow separation generating longitudinal vortices downstream of the generator. The circulation created by the vortex enables rapid transfer of fluid parcels to and from the heat transfer surface and thus, enhances the heat transfer. Different designs of vortex generators have been proposed in the literature and most common are cubical and delta winglets.

There has been extensive research, both experimentally and numerically, on determining the optimum configuration and shape of vortex generators for the given flow arrangement. The early work in this area goes back about two decades. Eibeck and Eaton (1987) studied the heat transfer effects of an isolated longitudinal vortex embedded in a turbulent boundary layer. The measurements were made in the direction normal to the flow at different downstream locations. Several types of half delta wing vortex generators

with angles of attacks equal to 5, 12 and 20° were examined. They found that under different conditions, the Stanton number increased up to 24% and decreased as much as 14%. The overall effect was a net increase in the spanwise-averaged heat transfer coefficient. They observed that the distortion of the turbulence field has no significant effect on the heat transfer, and argued that the distortion of the mean velocity field caused by the longitudinal vortex affects the Stanton number. Pauley and Eaton (1988) studied 16 different vortex pair configurations and two regular arrays which are often used to prevent boundary layer separation on lifting control surfaces. They analyzed the results using vorticity contour plots, and separated them into three categories: common flow down, common flow up and co-rotating vortices. They found that the common flow down caused the strongest distortion of the boundary layer over the greatest streamwise extent. They also found that these vortices did not interact strongly with one another, and that their strength increased linearly with the angle of attack, up to an angle of attack of 18°. Furthermore, the common flow up pairs of vortices found to interact strongly with one another but weakly with the viscous flow near the wall. In the case of co-rotating vortices, it was found that a single pair of co-rotating vortices would merge to form a single vortex if the initial spacing is not too large. The vortices in the array were found to be essentially independent.

Wroblewski and Eibeck (1991) experimentally investigated the heat transfer in a turbulent boundary layer, using half delta wings at an angle of attack of 12° as the vortex generators. The measurements were made in a plane normal to the direction of the flow at a Reynolds number of 1.82×10^6. They found that in the vortex core, the Reynolds

stress components were nearly equal and suggested that the turbulence is isotropic in this region. In the same region, they also found that the heat transport was enhanced and despite the high levels of turbulence, the Reynolds stress was small, indicating that the turbulent transport of momentum was suppressed.

Fiebig *et al.* (1991) experimentally investigated the effect of triangular and rectangular vortex generators on the flow structure, flow losses and heat transfer augmentation in a compact heat exchanger. They found that the drag induced by the vortex generator was proportional to the projected area, and was independent of the Reynolds number as well as its geometrical shape. They also observed that the heat transfer enhancement depends on the angle of attack of the generator, and showed that heat transfer increases with the angle of attack up to 60^{o}. They also found that the heat transfer enhancement was higher for the case of triangular vortex generator as compared to the rectangular one. Tiggelbeck *et al.* (1992) experimentally investigated the flow structure and heat transfer in a channel with multiple vortex generators of delta winglet type. They observed that near the rear edge of the winglets, the Nusselt number had a local enhancement of 310% in the case of one row of delta winglets, which increased to 460% with two rows of delta winglets.

Tsay *et al.* (2005) numerically investigated the heat transfer enhancement due to a vertical baffle in a backward-facing step flow channel. The effect of the baffle height, thickness and the distance between the baffle and the backward facing step on the flow structure was studied in detail for a range of Reynolds number varying from 100 to 500.

They found that an introduction of a baffle into the flow could increase the average Nusselt number by 190%. They also observed that the flow conditions and heat transfer characteristics are strong function of the baffle position. O'Brien *et al.* (2004) conducted an experimental study in a narrow rectangular duct fitted with an elliptical tube inside a fin tube heat exchanger, for a range of Reynolds numbers varying from 500 to 6300. A pair of delta winglets was used as the vortex generator. They estimated the local surface heat transfer coefficient and pressure drop, and found that the addition of a single winglet pair could increase the heat transfer by 38%. They also found that the increase in the friction factor due to the addition of a winglet pair was less than 10% over the range of Reynolds numbers studied. Dupont *et al.* (2003) investigated the flow in an industrial plate-fin heat exchanger with periodically arranged vortex generators for a range of Reynolds number varying from 1000 to 5000. They found that the vortex intensity increases with the Reynolds number.

Shafiqul *et al.* (2002) experimentally investigated the mean streamwise velocity and mean turbulent kinetic energy in a channel with square ribs with two pitch-to-height ratios. PIV was used as the measuring technique to study the flow characteristic in the vicinity of the ribs. Measurements were made at two Reynolds numbers, 7000 and 20000. They found that the ribs produce turbulence which created circulation. In the separated region downstream of the rib, eddies were formed. The largest magnitude of turbulent kinetic energy was observed near the reattachment point of the flow. They also noted that a high Reynolds number would accelerate the flow over the ribs and increase the pressure rise. They observed that the velocity gradients are strong in the separation

region which leads to a shorter reattachment length. The reattachment length was measured from the velocity vector fields in the developing, fully developed and exit regions of the flow for a range of Reynolds numbers between Re = 1400 to 50000. they observed that after Re=15000, there was a little difference in the reattachment lengths at different spanwise locations, indicating that and it become independent of the Reynolds number and pitch-to-height ratio.

Acharya *et al.* (2000) conducted experiments using internally ribbed channel with cylindrical vortex generators placed above the ribs. They studied the effect of the spacing between the vortex generators and the ribs. They found that the heat and mass transfer depend on both the generator-rib spacing to rib height (s/e) ratio and the Reynolds number. They showed that at low Reynolds number (Re = 5000), the heat transfer enhancement was observed for all s/e ratios. However, at high Reynolds number (Re = 30,000), the enhancement was observed only for the largest s/e ratio (s/e = 1.5). For this ratio, the generator wakes and rib shear layer interact with each other and promote mixing and thus, enhance heat transfer. For the smallest s/e ratio (s/e = 0.55), due to the smaller gap between the generator-ribs, at high Reynolds numbers the ribs act as a single element and prevent the redevelopment of the shear layer causing reduced heat transfer.

Tiwari *et al.* (2003) numerically simulated the effect of the delta winglet type vortex generator on the flow and heat transfer in a rectangular duct with a built-in circular tube. They observed that the vortices induced by the vortex generator resulted in an increase in the span-averaged Nusselt number at the trailing edge of the vortex generator by a factor

of 2.5 and the heat transfer enhancement of 230% in the near wake region. Lin *et al.* (2002) numerically studied the performance of a wave-type vortex generator installed in a fin-tube heat exchanger. They found that an increase in the length or height of the vortex generator increases the heat transfer, as well as the friction losses. They reported up to 120% increase in the heat transfer coefficient at a maximum area reduction of 20%, accompanied by a 48% increase in the friction factor.

Leonardi *et al.* (2003) conducted a numerical investigation of a flow over square bars attached to a wall. The same flow configuration was later investigated experimentally by Leonardi *et al.* (2004). Both studies were focused on the effect of the distance between bars to bar height (*w/k*) ratio on the flow behavior. Both investigations were made at the same Reynolds number of 4200. They found that the dependence of the flow behavior on *w/k* is very strong. At small values of *w/k*, the turbulent intensities and flow structure resemble the flow over a smooth wall. At high values of *w/k*, they observed that the normal wall motion induced by the bars was confined to smaller regions in the vicinity of the bars, and the overlying flow was similar to that over a smooth wall.

Nasiruddin and Siddiqui (2006) numerically investigated the impact of a baffle (which acts as a vortex generator) on the heat transfer in a smooth circular tube. A variety of baffle designs were considered that correspond to different baffle heights and orientations. The influence of these baffle designs on the vortex characteristics and the heat transfer rate was studied in detail. The results show that for the vertical baffle, an increase in the baffle height causes a substantial increase in the Nusselt number but the

pressure loss is also very significant. For inclined baffle at a given area blockage, they observed that the maximum Nusselt number was enhanced by a factor of 2.2 compared to that in the absence of a baffle. For the baffle inclined toward the upstream side, it was observed that the pressure loss was independent of the inclination angle. However, for the baffle inclined towards the downstream side, the pressure loss increased with an increase in the inclination angle. The results showed that a baffle inclined towards the downstream side with an angle of 15 degree is the optimal design. The heat transfer rate for this configuration was on average 70% higher than the heat exchanger with no baffle, with a minimal increase in the overall pressure loss. They also found that for a given baffle configuration, the Nusselt number increased with a decrease in the Reynolds number. They also investigated the impact of a second baffle on the overall Nusselt number enhancement and observed that when a second baffle is introduced to the flow, the average Nusselt number for the two baffles case was 20% higher than the one baffle case, and 82% higher than the no baffle case. The average pressure loss for the two and one baffle cases was 5.0 Pa and 2.8 Pa higher than the no baffle case, respectively.

The literature review in section 1.3 shows that significant research work has been done to investigate the impact of vortex generator on the flow behavior and heat transfer augmentation. However, most of these studies were focused on the estimation of the Nusselt number enhancement and less attention has been paid on the detailed investigation of the influence of vortex generator on the overall flow structure in general and in particular, the flow structure in the near-wall region. Furthermore, the studies that reported flow characteristics were focused on the flow behavior in the presence of the

vortex generator and no significant quantitative comparison has been made with that in the absence of the vortex generator.

1.4 Objectives

The literature review in the preceding sections shows that several studies have investigated the flow behavior with different surface conditions and with the addition of heat. However, most of these studies were focused on the investigation of the flow characteristics for the modified surface condition and/or in the presence of surface heating. A quantitative comparison of the flow behavior under modified condition with that of the non-modified condition is not well reported in the literature. This quantitative comparison is very crucial in order to improve our knowledge about which flow properties are influenced and altered due to these modifications and also to understand the underlying physical mechanisms that are responsible for this behavior. This issue is very critical in the near-surface region, which regulates the heat transfer across the fluid-solid interface. The present research is aimed at improving the knowledge and understanding of the physical processes that control heat transfer across the solid-fluid interface, which is very important in order to develop efficient heat exchangers. As mentioned earlier, to achieve this objective, the research has been divided into three phases with each phase focused on the fundamental physical phenomena from different aspects. The specific objectives of these phases are,

1. To investigate the simultaneous impact of different surface roughness on the flow behavior inside the channel.

2. To investigate the impact of wall heating on the flow characteristics in the near-wall region.
3. To investigate the impact of a vortex generator on the flow structure in the downstream region.

1.5 Thesis Layout

The layout of the remaining thesis is as follows. Chapter two gives a detailed description of the experimental setup, instrumentation and techniques. It includes, details about the channel and its configuration for the experiments conducted for each phase, the measurement techniques employed, and the equations used to compute the turbulent properties in chapters three to five. Chapter three describes the results obtained from the first phase, i.e. the simultaneous impact of walls of different surface roughness on the internal flows. The results of the second phase, i.e. the direct impact of heat addition on the near wall flow properties, are presented in chapter four. The final phase, i.e. the impact of a baffle on the channel flow, is presented in chapter five. The results from all three phases are summarized in chapter six along with some recommendations for the future work.

Chapter 2 - Experimental setup and techniques

The experiments were conducted in a closed loop apparatus consisting of five main sections. The components of the apparatus are described in the following subsections. Section 2.1 describes components that are common to all three phases mentioned in the previous chapter. Section 2.2 describes components or modifications to components described in section 2.1 that are specific to one particular phase.

2.1 The Experimental Apparatus

The experiments were conducted in a square channel with the inner cross-section of 7 cm × 7 cm. The channel consists of a 15 cm long settling chamber, 10 cm long trip section and 100 cm long test section. Water was used as the working fluid that was circulating through the channel in a closed loop. The schematic of the experimental apparatus is shown in figure 2.1. The main components of the channel and other accessories are described below.

2.1.1 The Settling Chamber

The settling chamber is made of aluminum and encompasses a honeycomb to straighten the flow before entering the trip section. A bleeder valve is installed at the top wall of the chamber to remove any trapped air locked in the channel.

2.1.2 The Trip Section

The trip and test section are made in the same fashion. That is, the top and two side walls are made of ½ inch thick non-tempered glass and the bottom wall is made of ½ inch thick

aluminum plate. The upstream end of the trip section is connected to the settling chamber by two Plexiglas flanges bolted together. The downstream end is connected to the test section in the same manner allowing it to be easily removed. This component is used for other experiments but it is considered as part of the channel for the experiments presented in this thesis.

2.1.3 The Test Section

The surface of the bottom aluminum plate of the test section was coated black with a marker to minimize the laser reflection. An aluminum end plate is attached at the downstream end of the test section and is bolted onto another aluminum plate. The settling chamber and the test section were both bolted onto 5 cm × 1.3 cm thick support plates. The length of the support plates were 7.5 cm and 94 cm beneath settling chamber and test section, respectively. These support plates are bolted to an exterior common base. All components of the channel with the exception of the trip section were fixed to one of the two bases, that is, either the upper base for components downstream of the pump (i.e. settling chamber, trip and test section), or to a lower base for components downstream of the test section (i.e. pump and water tank).

The glass walls and aluminum plates of the channel were joined together by an epoxy (Loctite D-609). The edge between the glass and the aluminum was also reinforced with a layer of silicone (Loctite 59530) because this edge is most susceptible to leaks.

2.1.4 The Pump

A magnetic pump (Little Giant 58002 4MD series) was used to circulate water from a water tank through the channel. A rubber pad is inserted between the pump and the lower base to minimize vibrations. A valve downstream of the pump outlet was used to vary the inlet flow rate to the channel. A valve was installed at the exit of the test section to set the channel's outlet flow rate, same as the inlet flow rate to avoid any pressure build up within the channel. This valve is also used to help eliminate any trapped air in the channel via the bleed valve mounted on top of the settling chamber.

2.2 The Experimental Apparatus Alterations for each Phase

2.2.1 Phase I

For the experiments conducted in this phase, no alterations were made to the apparatus described in section 2.1. As this phase was focused on the impact of surface roughness, the roughness of both surfaces was measured using Surftest SJ-301 (Mitutoyo), which measures the roughness height with the accuracy of 0.01 μm. The results show that the roughness at both the glass and aluminum surfaces is of *k*-type. The RMS roughness height for the glass plate is equal to 0.02 μm and that of the aluminum plate is 0.56 μm. The glass wall was found to be extremely smooth. Although the roughness length of both surfaces was small, the relative roughness which is defined as the ratio between the roughness lengths of aluminum to that of glass was very large. That is, the aluminum wall was approximately 28 times rougher than the glass wall. The complete experimental set-up for this phase is shown in figure 2.1.

2.2.2 Phase II -The Heating System

This phase was focused on the investigation of the impact of wall heating on the flow behavior. Therefore, an electric heater (240V Dimplex DBH-0750W) was attached to the bottom of the test section aluminum plate in order to supply the test section with a constant heat flux (see figure 2.2). Once turned on, the heater supplied a constant heat flux to the bottom side of the aluminum plate. A minimum of 90 minutes waiting time after turning on the heater was considered before data acquisition to allow uniform heat flux from the bottom wall.

2.2.3 Phase III - The Baffle

This phase was focused on the investigation of the impact of a baffle on the flow structure downstream of the baffle. Therefore, a baffle was installed in the test section. The baffle was made of Plexiglas with a rectangular geometry. The dimensions of the baffle were 1 cm in height, 0.5 cm in thickness and 5 cm in width. The baffle was adhered to 5 mm thick sheet of Plexiglas with the dimensions of 5 cm x 100 cm using silicone. This combined assembly was then slide into the channel from the downstream end (see figure 2.3 (a)). The setup of the test section with the instrumentation for this phase is shown in figure 2.3(b). The location of the baffle was 50 cm from the upstream edge of the test section. The baffle was used as a vortex generator.

2.3 The Measurement Technique

The two-dimensional velocity fields were measured using digital particle image velocimetry (DPIV). The measurements were made in a plane parallel to the side walls along the centerline of the test section. For each experimental run, 3000 images were

acquired at a rate of 30Hz. For every experimental run, the data acquisition was started at least ten minutes after the flow rate adjusted for that particular run allowing the flow inside the channel to reach steady state.

2.3.1 DPIV Technique

Digital Particle Image Velocimetry (DPIV) is a non-intrusive technique that measures flow velocities in a plane simultaneously at many points in a flow field. In this technique, the flow under investigation is seeded with tiny tracer particles that follow the flow. The set-up of a typical DPIV system is shown in figure 2.4. The set-up in the present experiments consisted of a Continuum Minilite 25 mJ Nd:YAG laser that was used as the light source of the DPIV measurements. A CCD camera (JAI CV-M2) with the resolution of 1600 × 1200 pixels was used to image the flow. The camera was mounted in the horizontal position. That is, the images were acquired with the dimensions of 1600 pixels in horizontal and 1200 pixels in vertical, with respect to the flow field. The camera was connected to a PC equipped with a frame grabber (DVR Express, IO Industries, London, ON, Canada) that acquires 8-bit images at a rate of 30 Hz. The water was seeded with silver-coated glass spheres, with the mean diameter of 15 μm (Potter Industries, Paoli, PA). These glass spheres were used as the tracer particles for the DPIV measurements. A four-channel digital delay generator (555-4C, Berkeley Nucleonics Corporation, San Rafael CA) was used as synchronizer to control the timing of the laser light pulses. In the PIV technique, a pulsed laser light sheet illuminates a plane in the flow. The tracer particles within the light sheet start glowing, and the camera records the positions of these particles. A short time later (known time delay), a second pulse illuminates the same plane and the camera captures the second image of the tracer

particles, whose positions are shifted in the second image due to the flow. These first and second images are called an image pair. In a given set of experiments, a series of image pairs are acquired.

2.3.1.1 Tracer Particles

The DPIV technique uses the motion of the tracer particles to measure the flow velocities. Therefore, it is important that these particles should follow the flow accurately, i.e. the particles should be neutrally or near-neutrally buoyant. In the present study, silver coated glass spheres with the mean diameter of 15 μm were used as the seed particles. The specific gravity of these particles is 1.65. Therefore, they were not perfectly neutrally buoyant. If particles are not perfectly neutrally buoyant, then it is important to compute the time response of the particle. That is, how quickly the particles response to any change in the flow behavior. The particle response time can be calculated using the following equation,

$$T_p = \frac{d_p^{\,2}}{36\nu_w}\left(1+2\frac{\rho_p}{\rho_w}\right) \tag{2.1}$$

where, T_P is the particle response time (Snyder and Lumley, 1971), d_p is the particle diameter, ν_w is the kinematic viscosity of fluid, and ρ_p and ρ_w are densities of particle and fluid, respectively (Siegel and Plueddemann, 1991). In the present study, the time response of the particles was estimated to be 0.021ms. At the highest Reynolds number where the fastest flow variations are expected, the Kolmogorov time scale (i.e. the smallest flow time scale) was computed to be approximately 47 ms. The comparison shows that the response time of these tracer particles is more that three orders of

magnitude smaller than the Kolmogorov time scale of the given flow. Thus, it was concluded that the tracer particles accurately followed the fluid motion in all cases.

2.3.1.2 Interrogation and Search Regions

In DPIV technique, to measure the velocity vectors, the first and second images of an image pair are divided into interrogation and search regions, respectively. The DPIV technique computes velocity vectors by cross-correlating an interrogation region in the first image with its corresponding search region in the second image. The size of the interrogation region is set in a way that the displacement of tracer particles within this region is expected to be approximately uniform. Typically, the size of the search region is twice the size of the interrogation region so that all particles in the interrogation region in first image, remain within in the search region in the second image. A typical DPIV image pair with the interrogation and search regions is shown in figure 2.5.

In the present study, the size of the interrogation region was set equal to 32 × 32 pixels and the size of the search region was set equal to 64 × 64 pixels. A 50% window overlap was used in order to increase the nominal resolution of the velocity field to 16 × 16 pixels. Due to the difference in the velocity magnitudes for all cases, a constant time separation between the two images of the image pair will give different particle shifts for different cases. That is, when the velocity magnitude is small, the particle shift will be smaller. Very small particle shift increases the uncertainty in the velocity measurements. Thus, the time separation between the two images of an image pair was varied in each case, in order to obtain reasonable particle shifts. The time delay for each case is given in the table of their respective chapter.

The velocity fields obtained from DPIV technique contains few spurious vectors mainly due to noise. These velocity fields are then processed through a correction scheme written in MatLab to correct spurious vectors found in the raw data. These corrected velocity fields are then analyzed to obtain different flow characteristics that include, mean velocity field, the turbulent velocity field and corresponding turbulent properties. The correction scheme used to correct the spurious vectors was developed by Siddiqui *et al.* (2001). In this scheme, the magnitude and angular orientation of each velocity vector is compared with the median of the neighboring vectors (eight or fewer depending on the location of the given vector). If the magnitude or orientation of the given vector is outside the specified range, then the given vector is considered to be spurious and is replaced by the median of the neighboring vectors. Once these erroneous vectors are replaced, then all the vectors are interpolated onto the grid points by performing the Adaptive Gaussian Window (AGW) interpolation. Figure 2.6(a) shows a raw velocity field. Few spurious velocity vectors near the top, bottom and middle are clearly visible. The velocity field after the implementation of the correction scheme is shown in figure 2.6(b). Comparison shows that the correction scheme accurately detects and corrects the spurious vectors. In all experimental cases, the spurious vectors were found to be less than 1%. Finally, the magnitude of both velocity components is converted from pixels into cm/s based on the length scale conversion between the pixels and cm, and the time delay between the two images of an image pair.

The total error in the velocity measurements due to the DPIV measurement scheme was calculated using the scheme in Siddiqui *et al.* (2001). They describe the error as the sum of errors due to gradients, particle density, particle diameter, out-of-plane motion, peak locking and AGW interpolation. The error for each particular case is tabulated in their respective tables (i.e. the errors for the experimental runs for the first phase are found in Table 3.1 and so forth). The complete procedure of the error estimation is presented in Appendix A.

2.3.2 Field of View of the Camera

2.3.2.1 Walls of Different Roughness – Phase I

The field of view of the camera for this phase of experiments was set equal to 9.4 cm horizontal and 7 cm vertical. The horizontal position of the camera was set in a way that the upper edge of the image coincides with the inner side of the top glass wall and the lower edge of the image coincides with the upper side of the aluminum wall. The measurement window was located at a distance of 65.5 cm from the upstream edge of the test section as shown in figure 2.1.

2.3.2.2 Heat Addition – Phase II

The field of view of the camera for this phase of experiments was set equal to 3.2 cm horizontal and 2.4 cm vertical. The horizontal position of the camera was set in a way that the lower edge of the image coincides with the upper side of the aluminum wall. The measurement window was located at a distance of 57 cm from the upstream edge of the test section as shown in figure 2.2.

2.3.2.3 Insertion of a Single Baffle – Phase III

The field of view of the camera for this phase of experiments was set equal to 12.2 cm horizontal and 5.4 cm vertical. The horizontal position of the camera was set in a way that the lower edge of the image coincides with the upper side of the aluminum wall. The measurement window was located at a distance of 47.4 cm from the upstream edge of the test section as shown in figure 2.3. The upstream edge of the camera field of view was 2.6 cm upstream of the baffle.

2.3.3 Temperature Measurements

Temperature measurements were made during the second set of experiments only. The temperature data was acquired via a 16-channel data acquisition card (PCI-6036E, National Instruments) using the LabView data acquisition software. Eight k-type thermocouples were used to obtain the temperature gradient in the near wall region. The first thermocouple was placed at the wall and the other thermocouples were placed horizontally in the vertical plane with a separation distance of 2 mm. The accuracy of the thermocouples is ±0.1 ^{o}C. The heater was turned on 1 ½ hours before the channel was filled with water and the measurements taken. The data was acquired 15 minutes after the flow rate was set to ensure uniformity of the flow rate.

2.4 Post Processing of the Velocity Data

The mean velocity and velocity gradients were computed by temporally averaging the velocities and velocity gradients at each grid point. The turbulent velocity fields were computed by subtracting the time-averaged mean velocity at each grid point, from the

corresponding instantaneous velocity. Various turbulent characteristics were computed from the turbulent velocity fields. The equations used to compute various turbulent properties are described below. It is important to note that since the data of the experiments corresponding to phases I and II were located in the fully developed region, the data was also spatially averaged in the horizontal direction. That is, at each depth, one tempo-spatially averaged value was computed. This was not done in the experiments of phase III, where the flow characteristics were analyzed at different spatial locations downstream of the baffle.

The energy production was computed using the following equation

$$P = -\overline{u'w'}\frac{dU}{dz} \tag{2.2}$$

where $-\overline{u'w'}$ is the Reynolds stress and $\frac{dU}{dz}$ is the mean streamwise velocity gradient (Pope 2000)

PIV velocity fields provide four velocity gradients in a plane. Doron *et al.* (2001) compared five different methods of estimating the energy dissipation and showed that the "direct" method which uses velocity gradients computed from the two-dimensional turbulent velocity field obtained from PIV measurements was the most accurate. The Energy dissipation rate was computed using the direct method as,

$$\varepsilon = 3\nu\left[\overline{\left(\frac{\partial u'}{\partial x}\right)^2} + \overline{\left(\frac{\partial w'}{\partial z}\right)^2} + \overline{\left(\frac{\partial u'}{\partial z}\right)^2} + \overline{\left(\frac{\partial w'}{\partial x}\right)^2} + 2\overline{\left(\frac{\partial u'}{\partial z}\frac{\partial w'}{\partial x}\right)} + \frac{2}{3}\overline{\left(\frac{\partial u'}{\partial x}\frac{\partial w'}{\partial z}\right)}\right] \tag{2.3}$$

where $\frac{\partial u'}{\partial x}$ is the streamwise velocity gradient in the horizontal direction, $\frac{\partial u'}{\partial z}$ is the streamwise velocity gradient in the vertical direction, $\frac{\partial w'}{\partial x}$ is the transverse velocity gradient in the horizontal direction and $\frac{\partial w'}{\partial z}$ is the transverse velocity gradient in the vertical direction and ν is the kinematic viscosity. The overbar denotes time averaging.

The friction velocity was computed using the relation,

$$u_* = \sqrt{\nu \left. \frac{dU}{dz} \right|_{z=0}} \tag{2.4}$$

where, $\left. \frac{dU}{dz} \right|_{z=0}$ is the mean streamwise velocity gradient at the wall.

The turbulent kinetic energy is computed using the relation,

$$E_K = \frac{3}{4}\left(u'^2 + w'^2\right) \tag{2.5}$$

where, the cross-stream component of velocity (v') is assumed to equal the average of the horizontal and vertical velocity components.

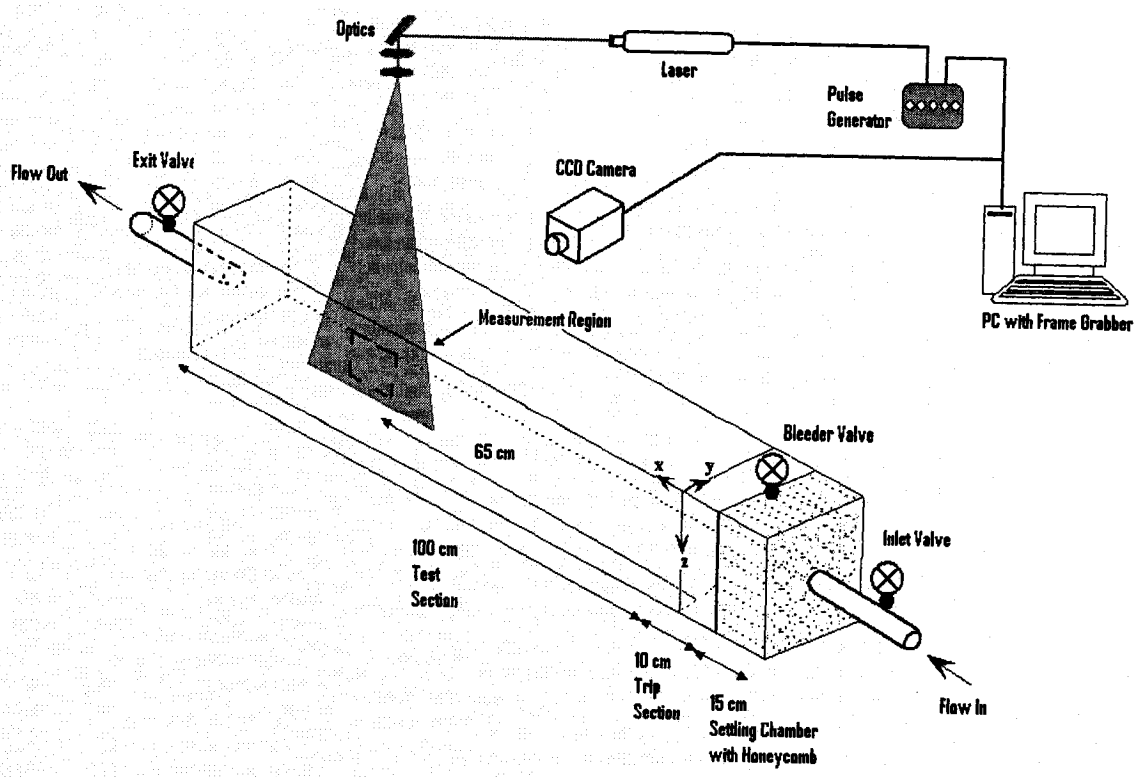

Figure 2.1: Schematic of the experimental set-up for phase I experiments (not to scale). The dashed lines show the measurement region, i.e. 9.4 cm horizontal and 7 cm vertical.

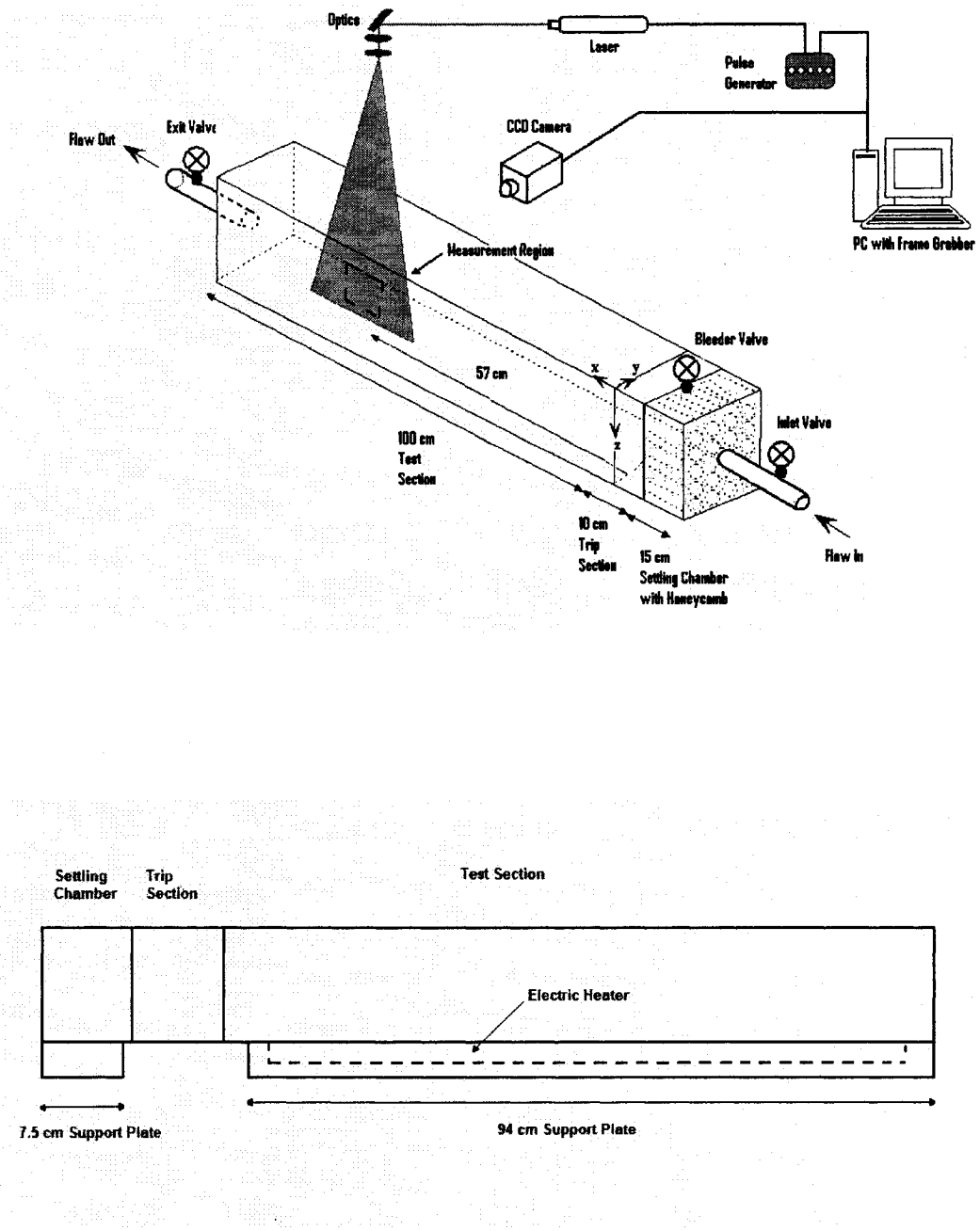

Figure 2.2(a): Schematic of the experimental set-up for phase II (not to scale). The dashed lines show the measurement region, i.e. 3.2 cm horizontal and 2.4 cm vertical, (b) two-dimensional view of the square channel (not to scale). The dashed lines represent the electric heater.

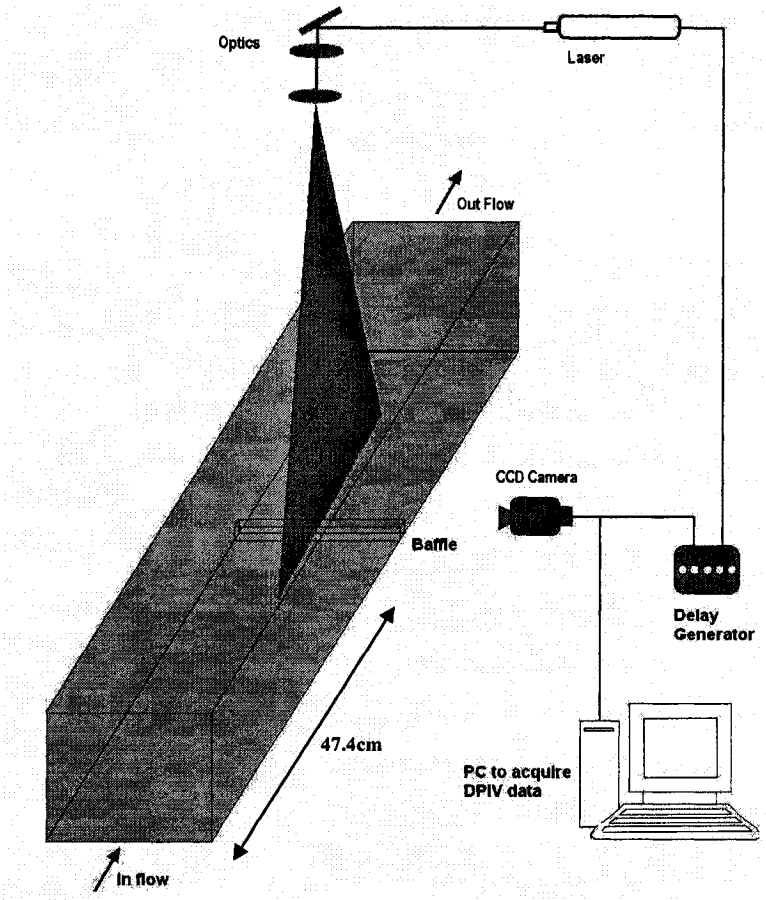

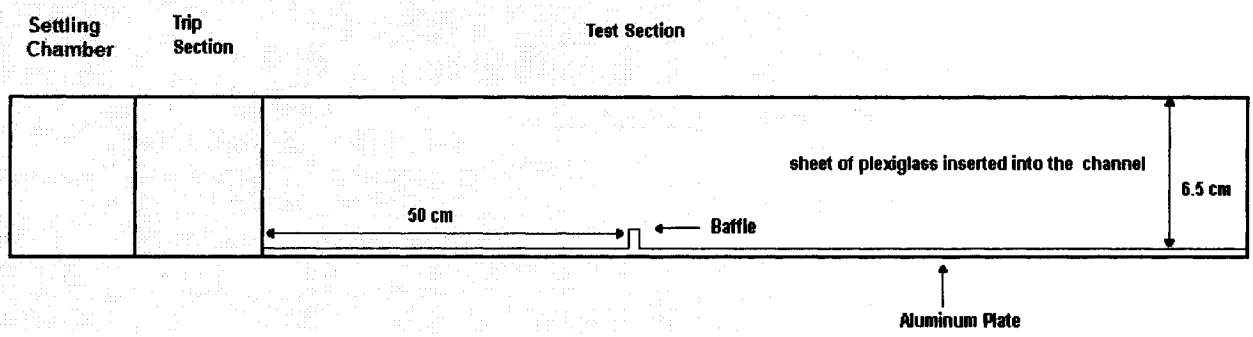

Figure 2.3: Schematic of the test section only for phase III (not to scale). The dashed lines show the measurement region, i.e. 12.2 cm horizontal and 5.4 cm vertical. The other components of the channel are the same as in Figure 2.1 and 2.2, (b) two-dimensional view of the square channel showing the baffle (not to scale).

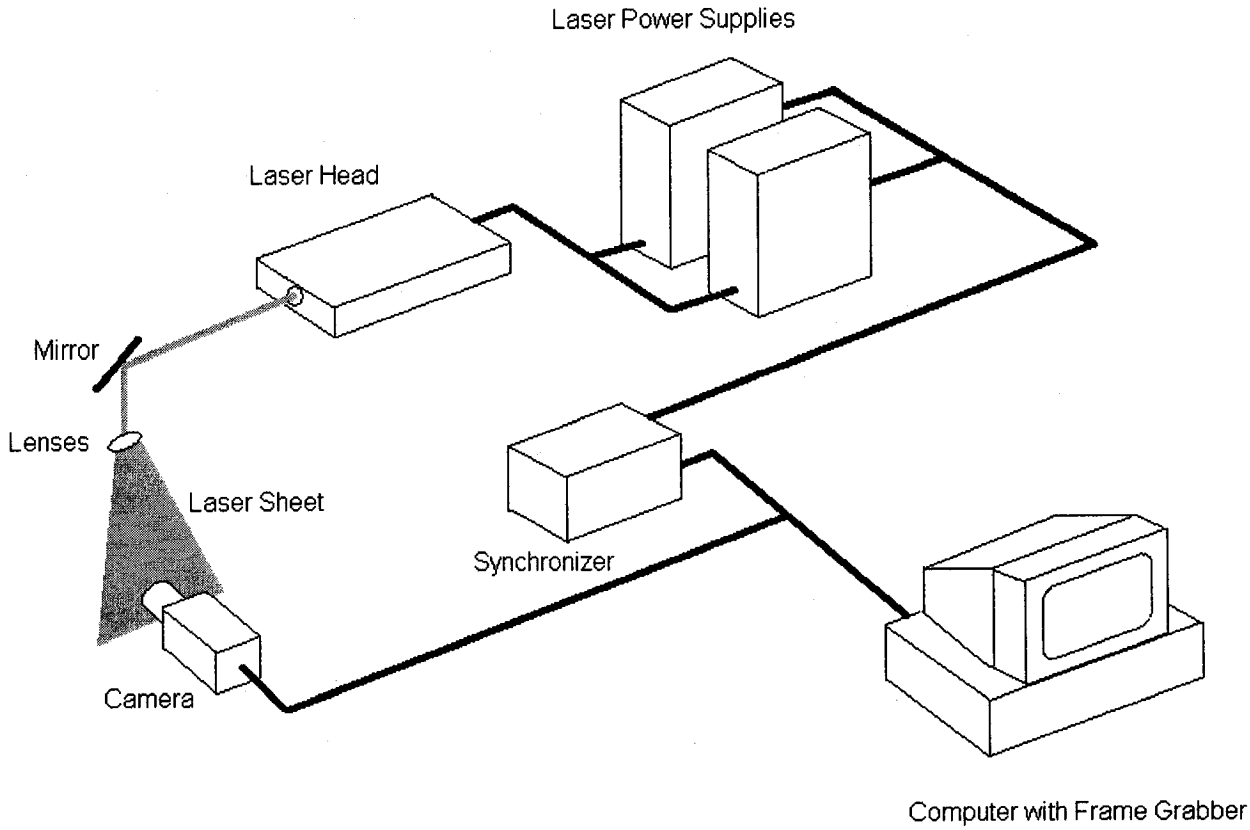

Figure 2.4: Schematic of a typical DPIV set-up

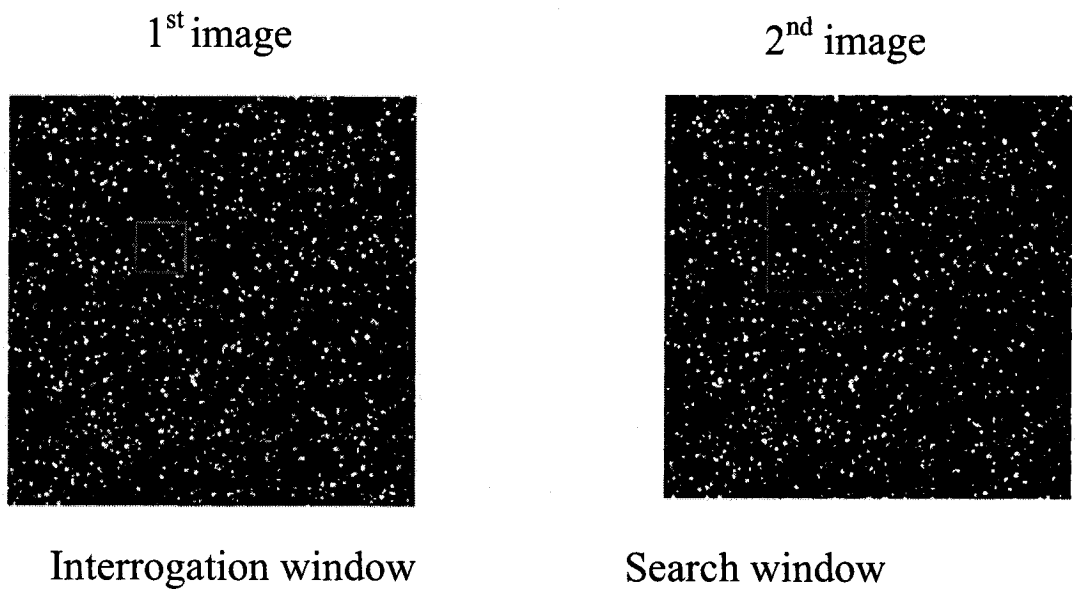

Figure 2.5: DPIV image pair (a) first image of image pair, red box represents the interrogation window; (b) second image of image pair, red box represents the corresponding search window

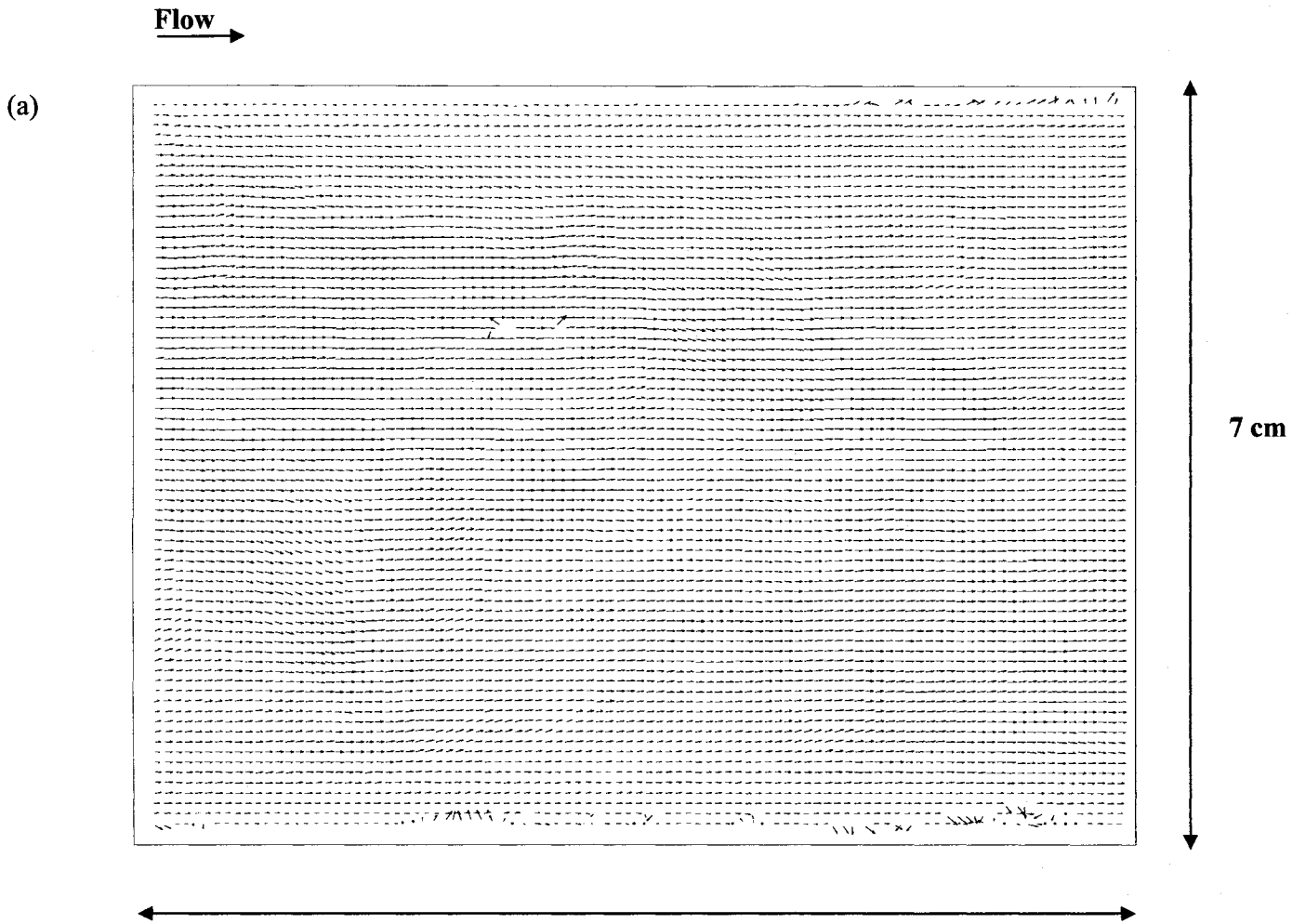

Figure 2.6: DPIV velocity vector field (a) before correction; (b) after correction scheme

(b)

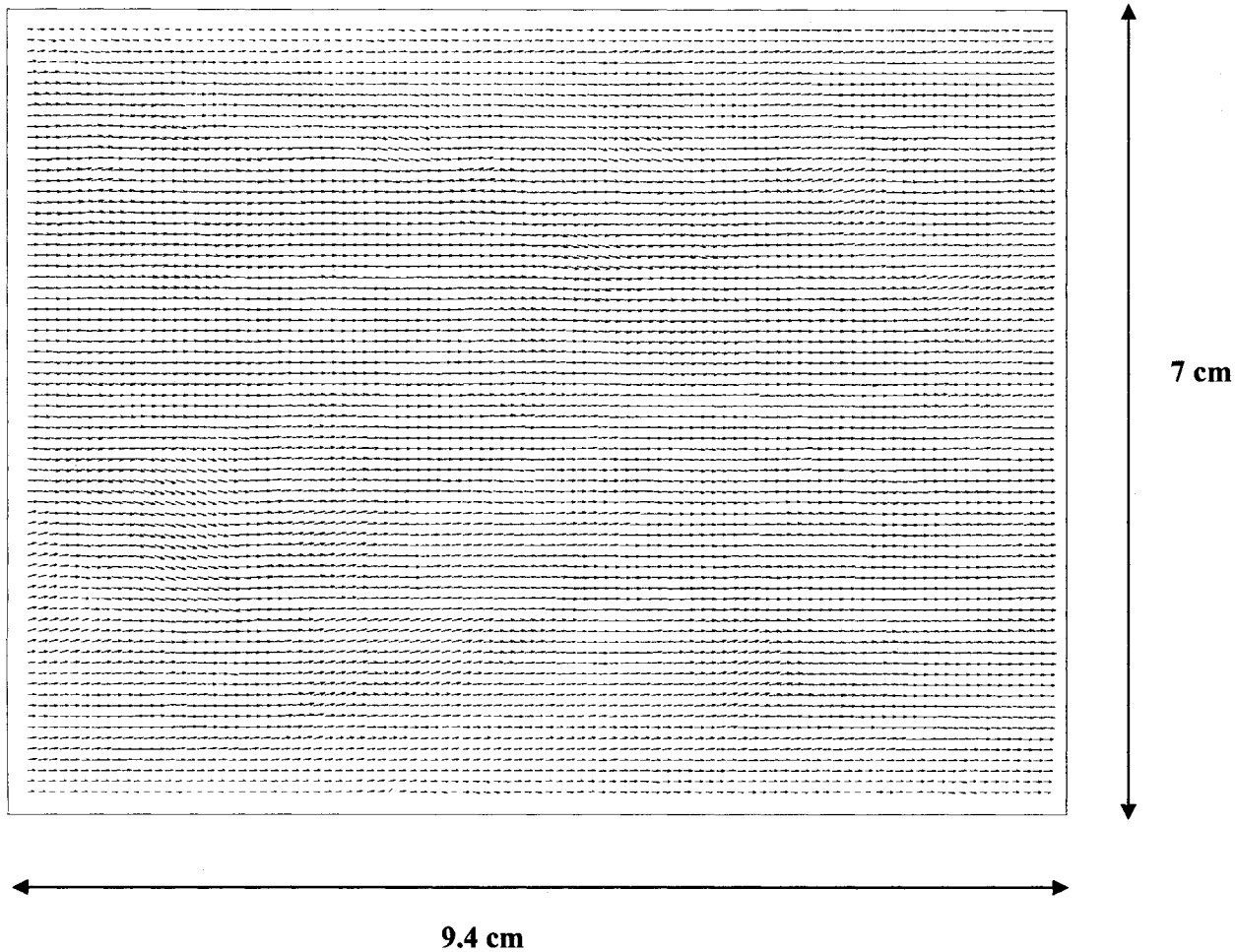

Chapter 3 - Flow Behavior in a Channel Bounded by Walls of Different Roughness

(Gajusingh and Siddiqui, 2006A)

The present chapter is focused on the investigation of the simultaneous impact of different wall roughness on the overall mean and turbulent characteristics in a channel flow. This would help in understanding the discrepancy in the flow behavior in the outer region reported in previous studies and also to understand the overall flow characteristics in a channel with different wall roughness. The experimental apparatus used for these experiments is described in chapter 2 sections 2.1 and 2.2.1. The bottom wall of the test section was made of aluminum and the top wall was made of glass. The roughness on both surfaces was measured using Surftest SJ-301 (Mitutoyo), which measures the surface height with the accuracy of 0.01 μm. The RMS roughness length for the glass plate is equal to 0.02 μm and that of the aluminum plate is 0.56 μm. The roughness length normalized by the viscous length scale (ν/u_*) is given in Table 3.1. The results show that the roughness length at both walls is significantly less than the viscous length scale and both surfaces are considered to be smooth. However, the relative roughness which is defined as the ratio between the roughness lengths of aluminum to that of glass walls was very large. That is, the aluminum wall was approximately 28 times rougher than the glass wall. Thus, herein after, among the two walls, the glass wall is considered as the smooth wall and the aluminum wall is considered as the rough wall.

Four experimental cases were considered that covered the range from laminar to fully turbulent. To check whether the flow was developed at the measurement location, the

mean streamwise velocity profiles near the upstream and downstream ends of the camera field of view (9 cm apart) were compared. The difference in the velocity profiles was less than 4% for all cases. This confirmed that for all cases the flow was developed. The friction velocity was computed based on the mean velocity gradient at the wall. The values of the friction velocity for both walls are presented in Table 3.1. The Reynolds number was calculated based on the rough wall friction velocity and the channel half-height or half of hydraulic diameter. The values of Reynolds number (Re_τ) for all cases are also presented in Table 3.1.

3.1 Mean Velocity

The mean streamwise velocity was computed by averaging the velocity data at each depth temporally and spatially. That is, for each experimental run, the time series were extracted at each grid point. The average velocity was obtained at each grid point by time-averaging. The time-averaged velocities at all grid points at a particular depth were then spatially averaged. This provided the spatial-temporal averaged velocity at each depth. In the present study, the depth, z, is referenced from the inner surface of the glass wall, with the positive z-axis pointing downwards. That is, $z/D_h = 0$ corresponds to the inner surface of the glass wall and $z/D_h = 1$ corresponds to the inner surface of the aluminum wall, where D_h is the hydraulic diameter of the channel. The vertical profiles of the mean streamwise velocity normalized by the maximum mean velocity are plotted in figure 3.1. The plot shows an asymmetry in the mean velocity profiles for all cases, that is, the maximum velocity is shifted towards the glass wall that has smaller roughness compared to the aluminum wall (roughness length of the glass wall is 28 times smaller

than that of the aluminum wall). The plot also shows that for fully turbulent cases (i.e. Re_τ = 144 and 164), the mean velocity profiles collapsed very well, which started to deviate at Re_τ = 71. The maximum velocity for these cases was observed at z/D_h in the range 0.3-0.35. The profile at Re_τ = 17 deviated significantly from the other cases with a prominent asymmetry. The maximum velocity for this case was located at z/D_h = 0.2. At Re_τ = 17, the flow was in the laminar regime, therefore, the influence of viscous forces was significant and thus, the impact of higher surface roughness was extended over a significantly large distance from the wall by viscous forces. At higher Reynolds numbers, the influence of viscous forces decreases and thus, the profiles became more symmetric.

Hanjalic and Launder (1972) also studied the influence of different wall roughness on the mean velocity profile for fully turbulent flow at Reynolds numbers of 18700, 36400 and 56000 (based on the maximum velocity and half the distance between the walls). In their experiments, the roughness length at the rough wall was several orders of magnitude larger than that at the smooth wall. They also observed an asymmetry in the mean velocity profile. Their mean velocity profile at Re = 18700 is also plotted in figure 2 for comparison. The plot shows that near the smooth wall in the region $0 < z/D_h \leq 0.3$, their profile is similar to that observed for fully turbulent cases in the present study. The location of the maximum mean velocity has also coincided. At higher Reynolds numbers (i.e. at Re = 36400 and 56000), the shape of their mean velocity profiles was also similar; however, the location of the maximum velocity was slightly shifted towards the smooth wall. From the location of the maximum velocity towards the rough wall (i.e. $0.3 < z/D_h \leq 0.8$), their profile deviated and lied in between the profiles for the laminar and turbulent cases. This indicates that their mean velocity profile was influenced more by the rough

wall compared to the turbulent cases in the present study, but this influence was smaller than that for the present laminar case. The relative difference in the roughness length between the two walls in the present study is significantly less than that in Hanjalic and Launder (1972). Thus, based on the results in figure 3.1 it can be argued that, in fully turbulent flows, when the relative roughness between the two walls is very large, significant asymmetry in the mean flow is observed even at very high Reynolds numbers. However, as the relative roughness between the two walls decreases, the mean velocity profiles tends to become more symmetric even at lower range of Reynolds numbers in the turbulent regime. In the laminar regime, however, the influence of comparatively lower relative roughness is more profound on the mean flow than the higher relative roughness in the turbulent regime. Thus, it can be concluded that from the location of maximum velocity towards the smooth wall, the trends in the mean velocity profiles are similar for different Reynolds numbers (in both laminar and turbulent regimes) and for different relative roughness. However, from the location of the maximum velocity towards the rough wall, different Reynolds numbers and relative roughness have a significant influence on the mean velocity behavior.

3.2 Vertical Mean Streamwise Velocity Gradient

Figure 3.2 shows the vertical profiles of the normalized mean streamwise velocity gradients. The plot shows that for all cases, the mean velocity gradients are relatively large in the near-wall regions and decreased with the distance away from the wall, as expected. For the three higher Reynolds number cases, the velocity gradients become almost negligible in the central region of the channel i.e. at non-dimensional depth

greater than 0.15 from each wall. Comparison of the velocity gradients magnitudes near smooth and rough walls shows that the gradients are stronger near the smooth wall compared to the rough wall for all cases. At the three higher Reynolds numbers, the velocity gradients near the glass wall are 1. 4, to 1.8 times higher than that near the rough wall. However, at $Re_\tau = 17$, the magnitude of the velocity gradient near the smooth wall is 5.6 times larger than that near the rough wall.

3.3 Turbulent Velocities

The DPIV measurements provide instantaneous velocity fields. The turbulent velocity fields were computed by subtracting the time-averaged mean velocity at each grid point, from the corresponding instantaneous velocity. Various turbulent characteristics were computed from the turbulent velocity fields. At $Re_\tau = 17$, the magnitudes of all turbulent properties were almost zero as the flow at this Reynolds number is laminar. Therefore, the turbulent properties are plotted for the three higher Reynolds numbers. The profiles of the normalized root-mean-square (RMS) streamwise and vertical turbulent velocity components are shown in figure 3.3 (a) and (b), respectively. Figure 3.3(a) shows that at the two higher Reynolds numbers, the profiles are relatively symmetric in the outer region, however, in the near-wall region, the magnitude of turbulent intensity is higher near the rough wall. It indicates that for the given relative roughness and the range of Reynolds numbers, the influence of wall roughness is restricted to the inner region. The plot also shows that for the fully turbulent cases (i.e. $Re_\tau = 164$ and 144), the values of the maximum streamwise turbulent intensity adjacent to the rough and smooth walls are 2.75 and 2.5, respectively. Bhaganagar *et al.* (2004) presented the vertical profiles of

turbulent intensities in a channel bounded by walls of different roughness obtained through DNS at Re_τ = 400. They also found that the RMS turbulent velocities were increased near the rough wall. In their case, the magnitudes of the maximum streamwise turbulent intensity near rough and smooth walls were approximately 3.1 and 2.5, which are in good agreement with the present study. They observed an asymmetry in the turbulent intensity profile in the outer region and argued that the different wall roughness affects the flow in the outer region as well. Hanjalic and Launder (1972) also observed higher streamwise turbulent intensity near the rough wall compared to that near the smooth wall, with the normalized intensity magnitude of approximately 2.1 and 1.0, respectively. However, they concluded that the profile of streamwise turbulent intensity is similar to that in a smooth symmetric channel. The results in the present and these previous studies indicate that in fully turbulent regime, if the roughness of the opposite walls are different, the streamwise turbulent intensity in the near-wall regions of both walls are affected. However, the influence of different wall roughness in the outer region may depend on the relative roughness of both walls and the Reynolds number.

The profile of streamwise turbulent intensity at Re_τ = 71 did not collapse with the data at higher Reynolds numbers, with the turbulent intensity magnitude less than that for the fully turbulent cases. This could be due to the reason that the flow at Re_τ = 71 is in the transition regime and the turbulence is not fully developed. The plot also shows that the turbulent intensity profile at this Reynolds number is non-symmetric. That is, at the smooth wall, the streamwise turbulent intensity was increased over a larger distance from the wall (i.e. up to z/D_h = 0.08) which is significantly large compared to all other cases,

and then started to decrease. At the rough wall, the streamwise turbulent intensity increased significantly within a thin layer at the wall (similar to higher Reynolds number cases) and then decreased sharply over a shorter distance, stayed almost constant over the next 1 cm layer, and then decreased gradually towards the core. An explanation for this trend is discussed later in context with other turbulent properties observed at this Reynolds number.

The RMS vertical turbulent velocity profiles in figure 3.3(b) show symmetric trend in the central region of the channel. The results also show that the magnitude of the vertical turbulent intensity increases with the distance from a wall. That is, the vertical turbulent intensity is higher in the outer region compared to the inner region for both smooth and rough cases. Bhaganagar *et al.* (2004) found that the trend of vertical turbulent intensity profile was similar to that of the streamwise intensity profile. That is, the vertical turbulent intensity was increased sharply near both walls and decreased towards the channel core from both sides with an asymmetry in the profile near the channel core. Hanjalic and Launder (1972) observed a decrease in the vertical turbulent intensity from the rough wall to the smooth wall. In the near-wall region, the magnitude of the vertical turbulent intensity in the present study for fully turbulent cases is comparable with that of Hanjalic and Launder (1972) at both rough and smooth walls and less than that in Bhaganagar *et al.* (2004). However, the overall trend of the vertical intensity profile is different in all three studies. Previous studies have also shown different trends of the vertical turbulent intensity profile. For example, Antonia and Krogstad (2001), Bakken *et al.* (2005) and Keirsbulck *et al.* (2002) found an increase in vertical turbulent intensity

within the inner region, which gradually decreased in the outer region, similar to Bhaganagar *et al.* (2004). Lee and Lee (2001) used PIV to measure velocity field in a turbulent boundary layer over smooth and riblet surfaces. For both smooth and rough surfaces, they observed the trend similar to figure 3.3(b) for the RMS vertical turbulent velocity. Romano (1992) measured the turbulent characteristics in a fully turbulent rectangular channel using PIV and LDA techniques. He observed similar trends in the profiles of streamwise turbulent intensity obtained from both techniques. However, the trends in the vertical turbulent intensity profiles were different from both techniques. The vertical turbulent intensity obtained from the PIV technique showed trend similar to that in figure 3.3(b), where that from the LDA showed trend similar to Antonia and Krogstad (2001), Bakken *et al.* (2005) and Keirsbulck *et al.* (2002). PIV provides two-dimensional instantaneous velocity fields with high spatial resolution. To further investigate this discrepancy, we analyzed the two-dimensional turbulent velocity fields. It was found that in the near-wall region, the streamwise turbulent velocity component dominates the flow with very weak vertical velocity fluctuations. As the distance from the wall increases, the magnitude of the vertical turbulent velocity component increases and in the outer region, it becomes almost comparable with the streamwise velocity component. A turbulent velocity field showing the typical flow behavior is plotted in figure 3.4 at $Re_\tau = 164$. The plot shows the predominantly streamwise flow near both walls. The strong vertical motions were observed mostly in the outer regions. Keirsbulck *et al.* (2002) showed snapshots of PIV turbulent velocity fields over smooth and rough walls. Their velocity plot over the smooth wall was similar to that in figure 3.4, that is, the flow was predominantly horizontal in the near-wall region and the vertical velocity component

grows with the distance from the wall (consistent with the trends observed in figure 3.3). Note that the turbulent intensity profiles in Keirsbulck *et al.* (2002) were not computed from their PIV measurements. Further experiments involving the simultaneous velocity measurements using PIV and other point measuring techniques should be conducted to resolve this discrepancy.

3.4 Reynolds Stress

The vertical profiles of the normalized Reynolds stress are plotted in figure 3.5. The plot shows that the magnitude of Reynolds stress increased up to a certain distance from the wall and then decreased towards the outer region where it almost vanished. Comparison of the Reynolds stress profiles shows that the Reynolds stress is higher near the rough wall at Re_τ = 144 and 164. The maximum Reynolds stress is approximately 0.5 and 0.8 near smooth and rough walls, respectively. Hanjalic and Launder (1972) also observed similar trend. Near the rough wall at $z/D_h \sim 0.85$, they found maximum normalized Reynolds stress equal to approximately 0.7, whereas, at $z/D_h \sim 0.05$, the Reynolds stress was equal to 0.2, which are comparable with the present study. However, they did not observe a peak in the Reynolds stress near the smooth wall. Miyake *et al.* (2001) simulated the flow in a channel with smooth and rough bounding walls at Re_τ = 150. They also observed a trend similar to figure 3.5 with the maximum normalized Reynolds stress approximately equal to 1.1 and 0.3 near rough and smooth walls, respectively. The maximum Reynolds stress was located at $z/D_h \sim 0.1$ from each wall which is consistent with the present study. At Re_τ = 71, the magnitude of the Reynolds stress is almost the same near both walls.

The analysis of the Reynolds stress behavior in the channel indicates that the wall surface roughness has a significant impact on the overall magnitude of the Reynolds stress. On the rougher wall side, the Reynolds stress is propagated deeper into the outer region. As a result, the location of the zero stress is shifted towards the smoother wall. This indicates that the Reynolds stress produced by the rougher wall dominates in the channel. Hanjalic and Launder (1972) argued that the interaction of dissimilar flow generated at both walls results in strong diffusional transport of turbulent shear stress and kinetic energy from the rough towards the smooth wall.

Another interesting feature observed in figure 3.5 is that the zero stress remained at the same vertical location i.e. $z/D_h = 0.4$ that corresponds to a distance of approximately 3 cm from the smoother wall, for all Reynolds numbers studied here. Previous studies investigating the effect of different wall roughness have also observed a shift in the location of zero stress from the channel centerline towards the smooth wall. Hanjalic and Launder (1972) observed that the location of zero stress moved to $z/D_h \approx 0.2$. They also found that the location of zero shear stress shifted slightly towards the smooth wall with an increase in the Reynolds number. They observed that as the Reynolds number increased by almost a factor of four, the location of zero stress was shifted by approximately 15%. Miyake *et al.* (2001) found the location of zero stress at $z/D_h \approx 0.3$. The results in figure 3.5 and these previous studies indicate that the dominance of the Reynolds stress in the turbulent flow is governed by the relative magnitudes of the surface roughness between the two walls and it is not dependent on the Reynolds number.

Keirsbulck *et al.* (2002) observed that the turbulent intensities and Reynolds stress are affected by the wall roughness only in the inner region and remain unaffected in the outer region. However, in the inner region, they observed that the streamwise turbulent intensity and Reynolds stress are higher for the smooth wall, whereas, vertical turbulent intensity is higher for the rough wall. Antonia and Krogstad (2001) found that the streamwise turbulent intensity is not affected by the wall roughness, whereas, the vertical turbulent intensity and Reynolds stress are higher at the rough wall. They argued that the wall roughness affects the outer layer and the momentum transport. On the other hand, Bakken *at al.* (2005) observed that the wall roughness influence the turbulent properties only in the inner region. It should be noted that Bakken *et al.* (2005) conducted measurements in a channel with the same roughness on both sides. The present results have shown that the relative roughness between the two bounding surfaces has a significant impact on the Reynolds stress distribution, particularly in the outer layer. Thus, when the flow behavior is investigated by increasing the roughness of one surface while keeping the other surface at the same roughness, the turbulent stresses are expected to increase in both the inner and outer layers at the former.

3.5 Turbulent Energy Production

The turbulent kinetic energy production can be computed using equation (2.2). The PIV system used in the present study measured two velocity components (u and w). We can compute only one component of Reynolds stress i.e. $\overline{u'w'}$. In the given measurement plane (i.e. middle of the channel bounded by upper and lower walls), the only velocity

gradient that primarily contributes to turbulence production is dU/dz. Thus, equation (2.2) provides good estimation of the turbulent kinetic energy production in the given measurement plane. The vertical profiles of the normalized turbulent kinetic energy production are plotted in figure 3.6. The plot shows that the energy production is almost zero in the central region of the channel due to very small magnitudes of Reynolds stress and mean velocity gradients in this region. Comparison of the energy production magnitudes in the regions near the smooth and rough walls show that at $Re_{\square} = 71$, the energy production is 1.5 times higher near the glass wall. At $Re_\tau = 144$, the energy production near this rough wall is approximately 25% higher than the smooth wall. At $Re_\tau = 164$, comparable magnitudes of energy production are observed near both walls. Hanjalic and Launder (1972) observed a relatively large enhancement of energy production near the rough wall compared to the smooth wall. Their closest measurement relative to the rough wall was at $z/D_h \approx 0.85$, where the magnitude of normalized energy production was approximately 12, which is comparable to the energy production in the present study at the same location. Near the smooth wall at $z/D_h \approx 0.05$, they found normalized energy production equal to 3 which is significantly less than that in figure 3.6 at the same location. They also observed minimum energy production near the location of zero stress. The profiles in figure 3.6 also show that the enhanced energy production rate is observed up to 30% of the channel's height along both walls. Bhaganagar *et al.* (2004) also observed the enhanced energy production up to the similar distance from walls, and almost zero production at greater heights. They however, found relatively large magnitude of energy production near the rough wall compared to the smooth wall. At $Re_\tau = 71$, the opposite trend is observed, that is, the enhanced energy production is

observed up to greater distance from the smooth wall compared to the rough wall. This behavior is consistent with that in figures 3.3(a) and 3.5 at $Re_\tau = 71$. Thus, it can be concluded that in the transition regime, the magnitude of turbulent intensity, Reynolds stress and the rate of energy production are relatively large near the smooth wall. However, in fully turbulent flow, the turbulence is stronger near the rough wall.

3.6 Turbulent Energy Dissipation

The rate of turbulent kinetic energy dissipation was computed using equation (2.3). The normalized rate of energy dissipation is plotted in figure 3.7 as a function of normalized depth. The plot shows that in the outer region, the dissipation rate remains almost constant and lower than that in the near-wall region. Comparison of the dissipation rate in the near-wall regions shows that the dissipation rate is a factor of 2-3 higher near the rough wall. Hanjalic and Launder (1972) observed an enhancement in the dissipation rate by approximately a factor of three. Their estimate of normalized dissipation closest to the rough wall was comparable with the present study, but it was lower near the smooth wall. Bhaganagar *et al.* (2004) found an enhancement in the rate of energy dissipation by approximately a factor of two near the rough wall. Their dissipation rate profile is similar to that in figure 3.7.

In order to compare the magnitudes of the turbulent kinetic energy production and dissipation, the production-dissipation ratio (P/ε) is plotted in figure 3.8 versus the depth. The plot shows that for all cases and at both walls, the dissipation is significantly higher than production immediately adjacent to the wall. This is due to the relatively large

magnitudes of the turbulent velocity gradients near the wall. As the distance from the wall increases, the ratio increases, that is, the magnitude of the energy production becomes larger. With a further increase in the distance from the wall, the ratio started to decrease again and approaches zero in the central region of the channel. This is consistent with the typical profile of P/ε observed in the channel flows (Pope 2000). For example, Kim *et al.* (1987) reported that at Re = 13750, P/ε = 1.81. For the given range of Reynolds numbers, the peak values of P/ε in figure 3.8 are within reasonable agreement. Comparison of the peak P/ε values between the two walls show that at the largest Reynolds number (Re_τ = 164), the peak values are comparable. At Re_τ = 144, the ratio is larger near the rough wall. However, at Re_τ = 71, the peak value of P/ε near the smooth wall is a factor of 2.5 larger than that at the rough wall.

As seen earlier in figure 3.3(a), the vertical profile of the RMS streamwise turbulent velocity at Re_τ = 71 exhibits a non-symmetric trend. That is, at the smooth wall, the streamwise turbulent intensity was increased over a larger distance from the wall (i.e. up to z/D_h = 0.1) compared to other cases and then decreased gradually towards the channel core. At the rough wall, the streamwise turbulent velocity stayed almost constant for 0.78 < z/D_h < 0.93 and then decreased gradually towards the core. This behavior can be explained on the basis of the production-dissipation (P/ε) ratio as follows. Near the smooth wall at Re_τ = 71, the energy production is 1.5 times higher and the rate of energy dissipation is approximately a factor of four smaller than the corresponding values near the rough wall. A higher production rate and very small dissipation rate resulted in an increase in the turbulent intensity near the smooth wall. This increase in turbulent

intensity is manifested in the streamwise velocity component as the turbulence is predominantly streamwise in the near-wall region. Near the rough wall, in the region 0.78 < z/D_h < 0.93, the ratio between P and ε remains the same thus, no significant change is observed in the magnitude of the streamwise turbulent velocity. It should also be noted that at this Reynolds number the flow is in the transition regime, and the turbulence is not fully developed.

3.7 RMS turbulent vorticity

The normalized RMS turbulent vorticity is plotted in figure 3.9 as a function of normalized depth. The plot shows that for any given Reynolds number, the turbulent vorticity is maximum near the wall and decreased away from the wall. In the central region, the vorticity magnitude is almost constant. Comparison near the smooth and rough walls shows that the turbulent vorticity is more than 50% stronger near the rough wall compared to the smooth wall. The trend in figure 3.9 is similar to Bhaganagar *et al.* (2004), who also observed significant enhancement of turbulent vorticity near the rough wall.

3.8 Discussion

Comparison between the present and previous studies shows that the influence of different wall roughness on the flow behavior in the inner region is similar, however, the extent to which the difference in roughness influences the flow behavior in the outer region varied for different properties. The Reynolds stress profile in the present study in both inner and outer regions are similar to that of Miyake *et al.* (2001) and Hanjalic and

Launder (1972), however the zero stress location in the latter studies was slightly shifted towards the smooth wall. The trends of streamwise turbulent intensity and turbulent vorticity in the present study are similar to those in Bhaganagar *et al.* (2004), however, they observed a slight asymmetry in the turbulent intensity profile in the outer region. The profiles of energy production and dissipation show a relative enhancement near the rough wall, but both parameters decreased sharply with the distance from both walls and become negligible in the outer region. These trends are similar to Bhaganagar *et al.* (2004) who also observed that the production and dissipation are enhanced near the rough wall and become negligible in the outer region. Miyake *et al.* (2001) also observed maximum production and dissipation in the inner region which decreased sharply towards the outer region. These trends are however, different from that of Hanjalic and Launder (1972) who observed an asymmetry in the profiles of energy production and dissipation that is, both the energy production and dissipation influenced the outer region of the rough wall.

In a square channel, the corner effect which induces a secondary flow could influence the flow behavior in the channel. Huser and Biringen (1993) conducted numerical simulations in a square duct at Re_τ = 600. They have shown that at low Reynolds numbers, the secondary flow is very weak near the wall bisector or the center plane of the channel. Hirota *et al.* (1997) also observed a similar trend from their experimental study in a 5 cm × 5 cm square channel. The side walls in the present setup are made of glass, which is very smooth in terms of absolute roughness. Thus, the impact of side walls on the flow at the mid-channel measurement location would be small.

The present chapter investigated the flow behavior in a channel bounded by an aluminum wall and a glass wall. The roughness of both walls in the absolute term is very small and the flow is considered to be smooth. However, from the aspect of relative roughness, the aluminum wall is about 28 times rougher than the glass wall. In previous studies investigating the impact of different wall roughness, in the absolute terms, one bounding wall was rough and the other was smooth and the relative roughness was very large. The flow structure obtained in the present study is to a large extent, similar in shape and magnitude to that reported in the previous studies. Thus, it can be concluded that the relative difference, i.e. the ratio between the roughness at both walls has a major impact on the overall flow behavior in the channel even if the absolute roughness in very small.

Table 3.1: Properties for different cases; E, uncertainty in velocity measurements; Re_τ, Reynolds number based on friction velocity at the rough wall and half channel height; u_{*R}, friction velocity at the aluminum wall; u_{*S}, friction velocity at the glass wall; h_R^+, roughness length at the aluminum wall normalized by ν/u_{*R}; h_S^+, roughness length at the glass wall normalized by ν/u_{*S}

Δt (ms)	10	12	20	66.67
E (%)	2.49	2.55	3.56	6.51
Re_τ	164	144	71	17
u_{*R} (cm/s)	0.437	0.383	0.190	0.046
u_{*S} (cm/s)	0.575	0.480	0.287	0.129
h_R^+	0.003	0.002	0.001	0.0003
h_S^+ (10^4)	1.2	1.0	0.6	0.3

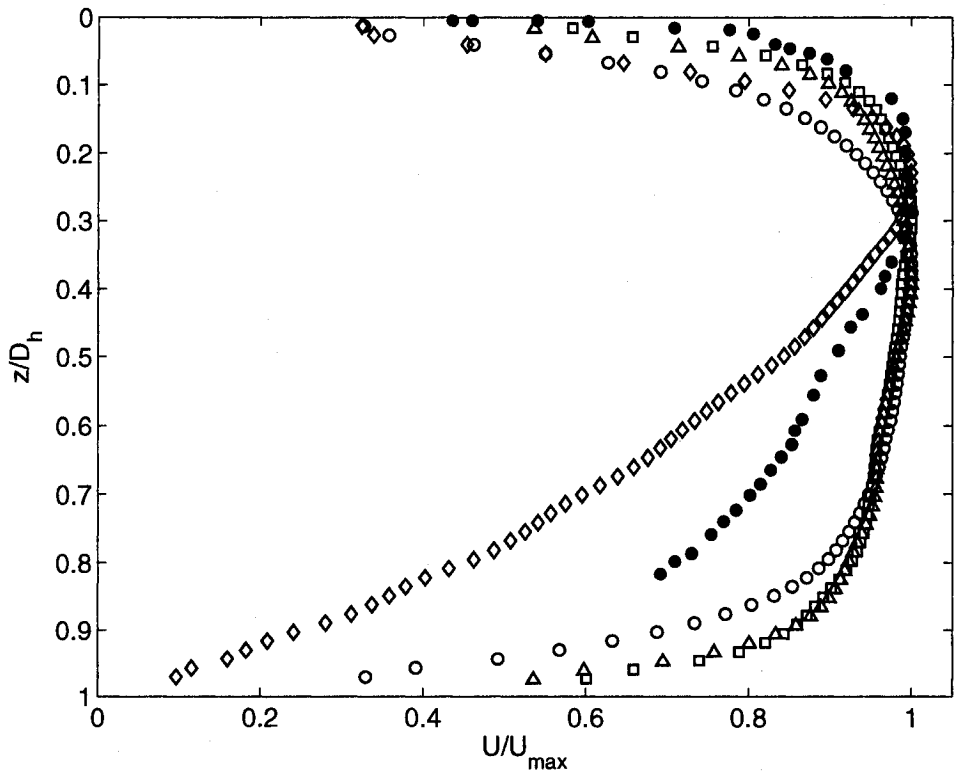

Figure 3.1: The mean streamwise velocity normalized by the maximum of the mean streamwise velocity versus the channel depth normalized by the hydraulic diameter. Re_τ = 164 (□), Re_τ = 144 (Δ), Re_τ = 71 (○) and Re_τ = 17 (◊). z/D_h = 0 corresponds to the glass surface and z/D_h = 7 cm correspond to the aluminum surface. Hanjalic and Launder [8] at Re = 18000 (●).

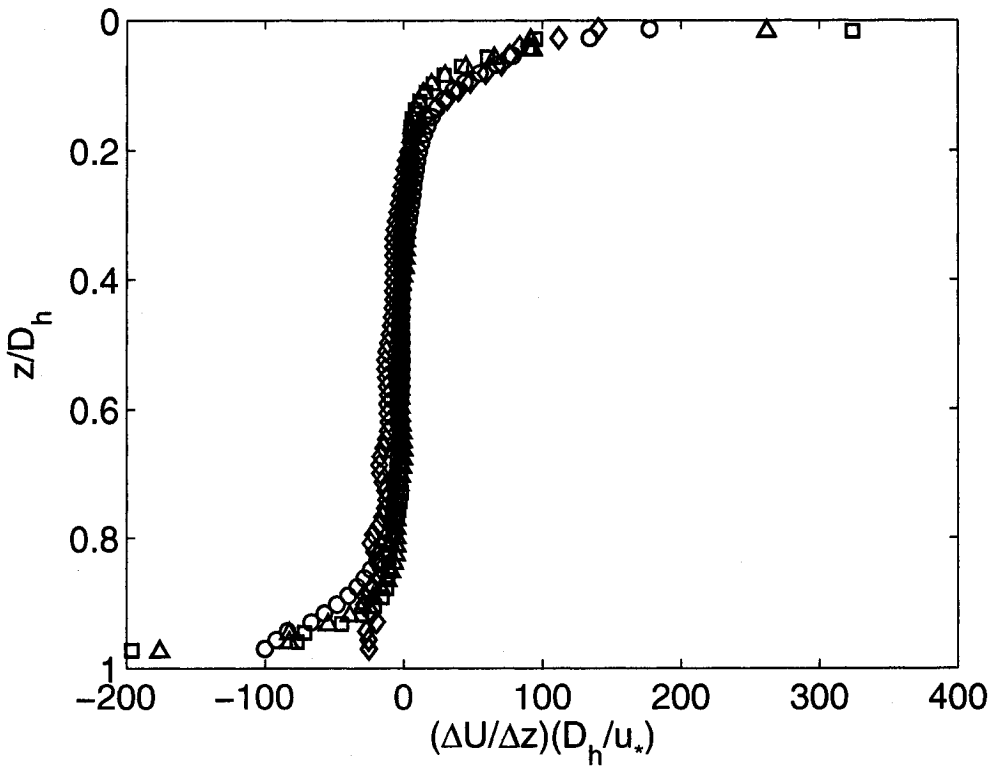

Figure 3.2: The vertical profiles of the mean streamwise velocity gradients normalized by the rough surface friction velocity and hydraulic diameter. Dashed, $Re_\tau = 164$ (□), $Re_\tau = 144$(Δ), $Re_\tau = 71$ (○).

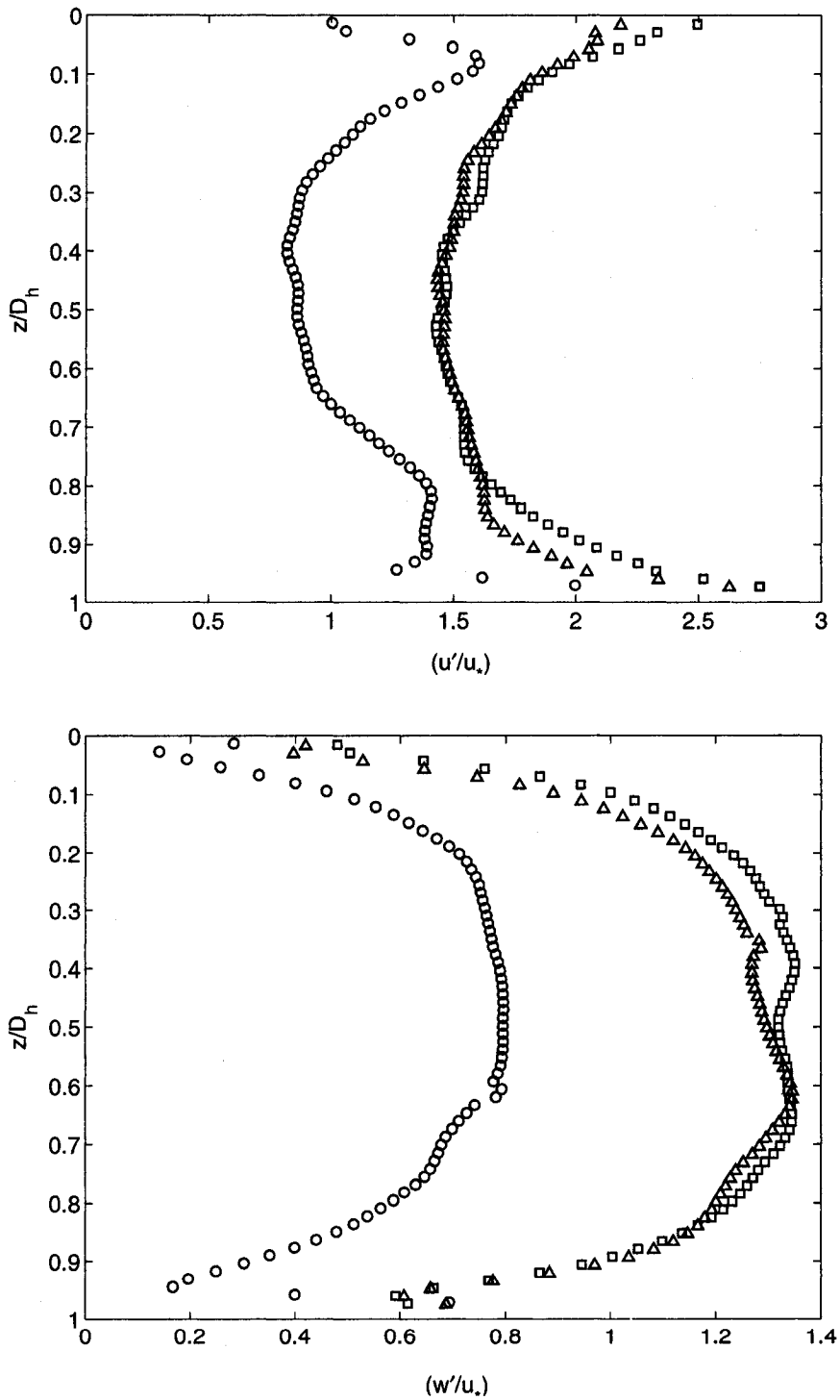

Figure 3.3: The plots of (a) RMS streamwise turbulent velocity, (b) RMS vertical turbulent velocity, versus the normalized depth. The turbulent velocities are normalized by the rough surface friction velocity. Re_τ = 164 (□), Re_τ = 144(Δ), Re_τ = 71 (○).

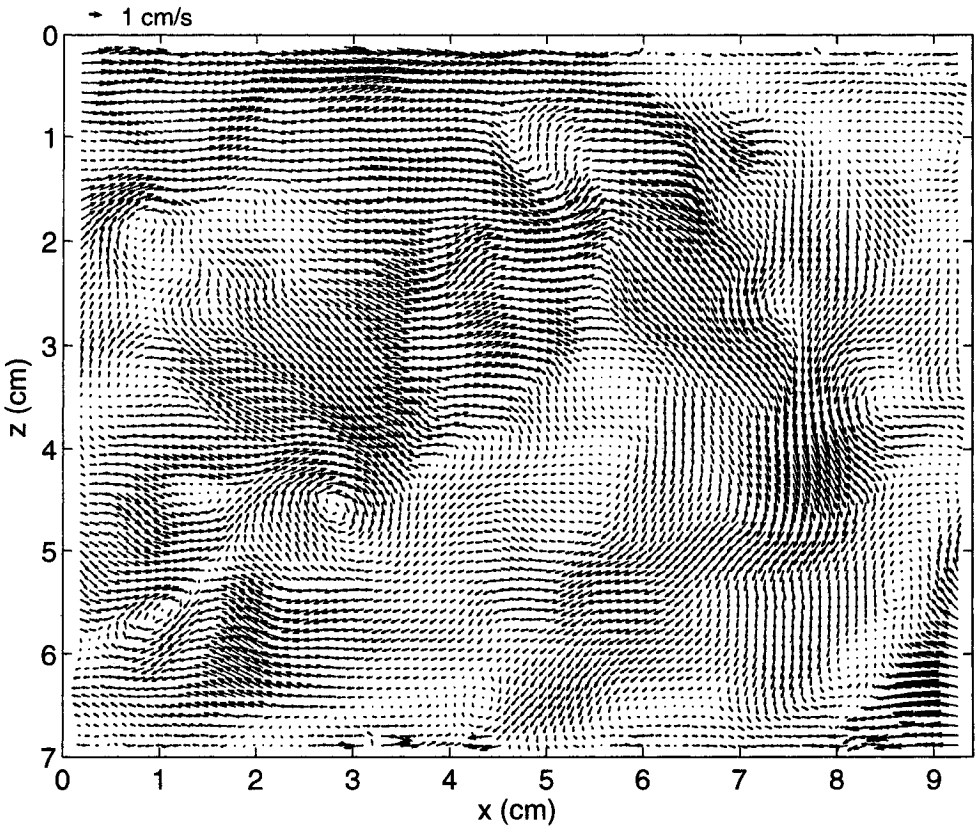

Figure 3.4: Two-dimensional turbulent velocity field at $Re_\tau = 164$.

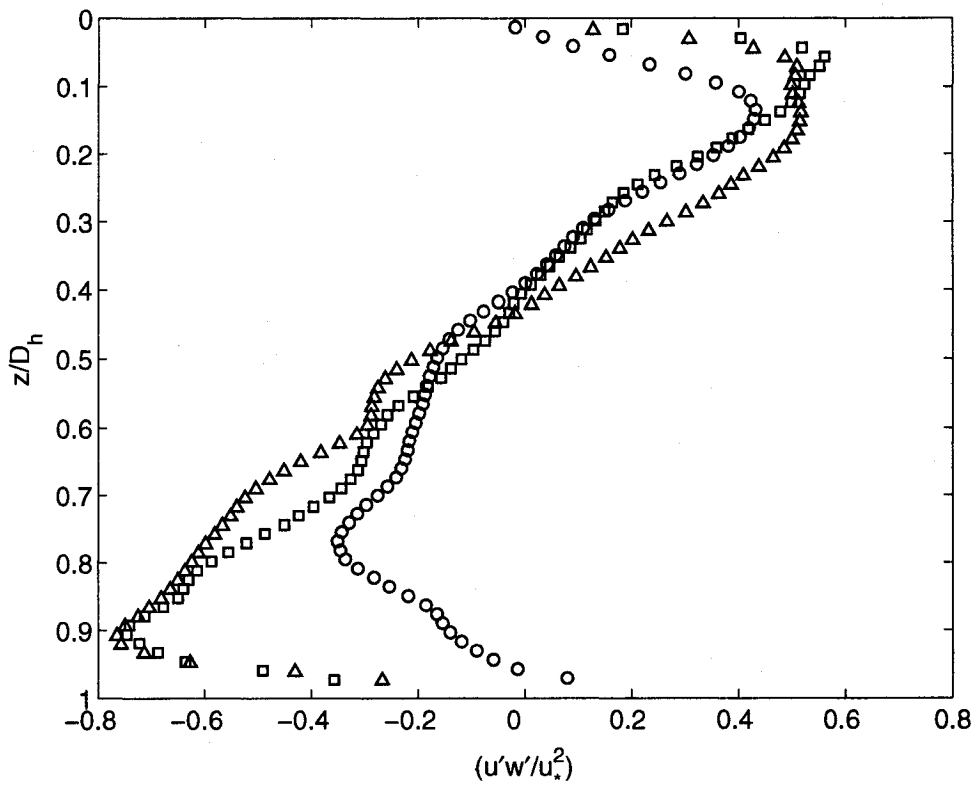

Figure 3.5: The Reynolds Stress normalized by the rough surface friction velocity, versus the normalized channel depth. $Re_\tau = 164$ (□), $Re_\tau = 144$(Δ), $Re_\tau = 71$ (○).

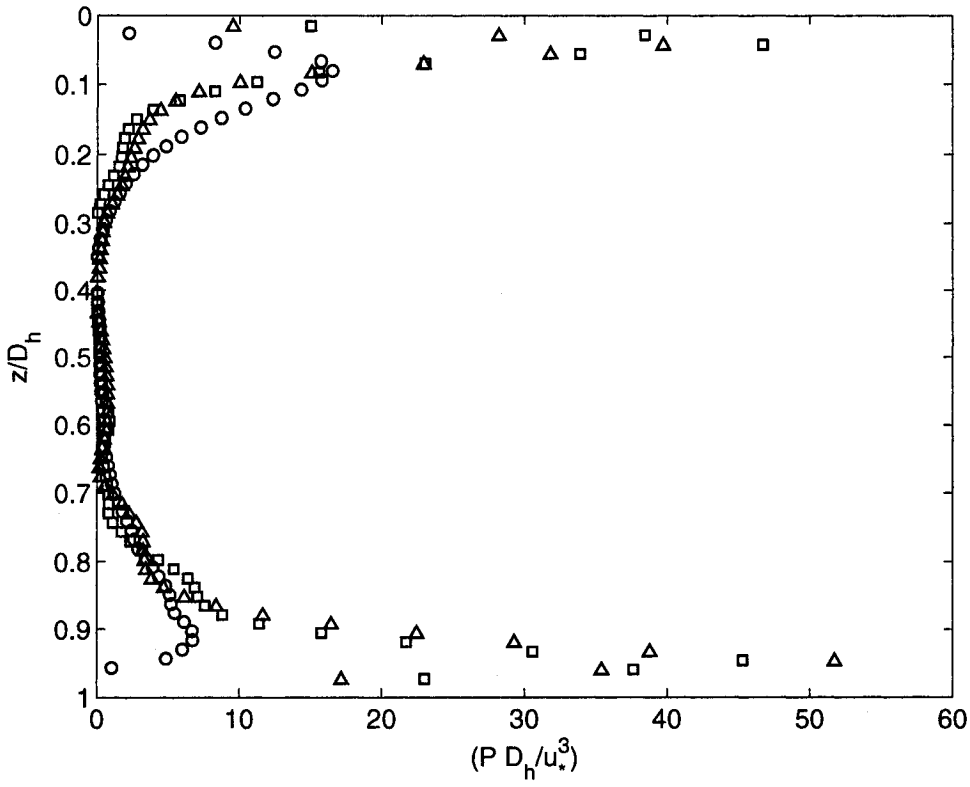

Figure 3.6: The rate of turbulent kinetic energy production normalized by the rough surface friction velocity and hydraulic diameter is plotted versus the normalized channel depth. $Re_\tau = 164$ (□), $Re_\tau = 144$(Δ), $Re_\tau = 71$ (○).

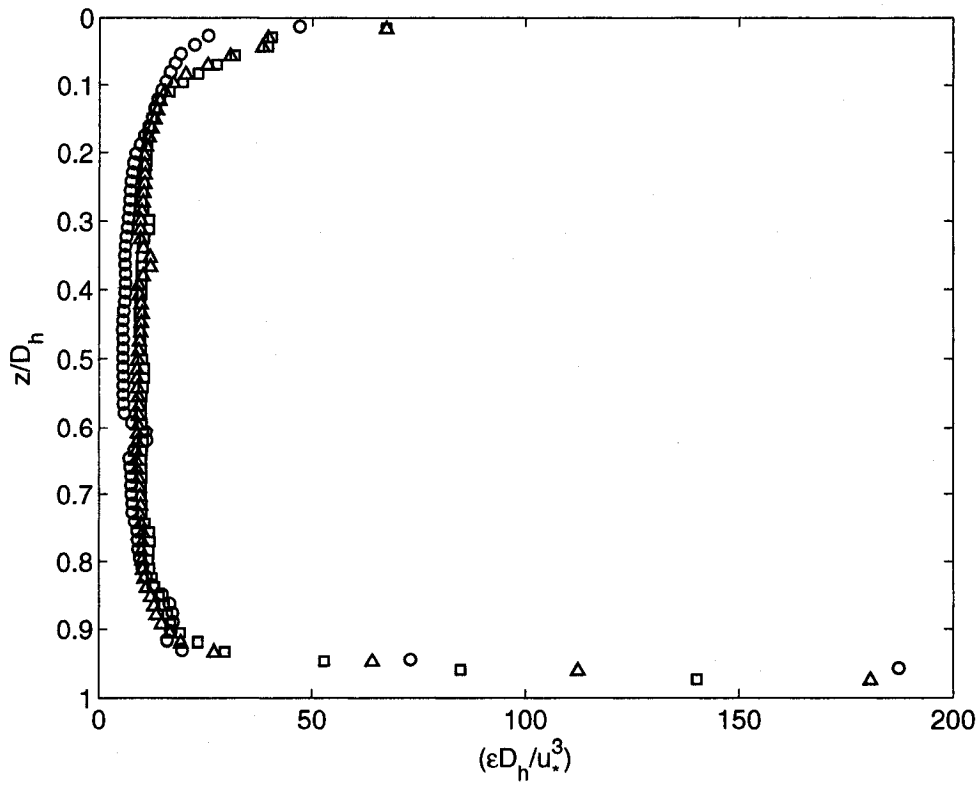

Figure 3.7: The rate of turbulent kinetic energy dissipation normalized by the rough surface friction velocity and hydraulic diameter is plotted versus the normalized channel depth. $Re_\tau = 164$ (□), $Re_\tau = 144$(Δ), $Re_\tau = 71$ (○).

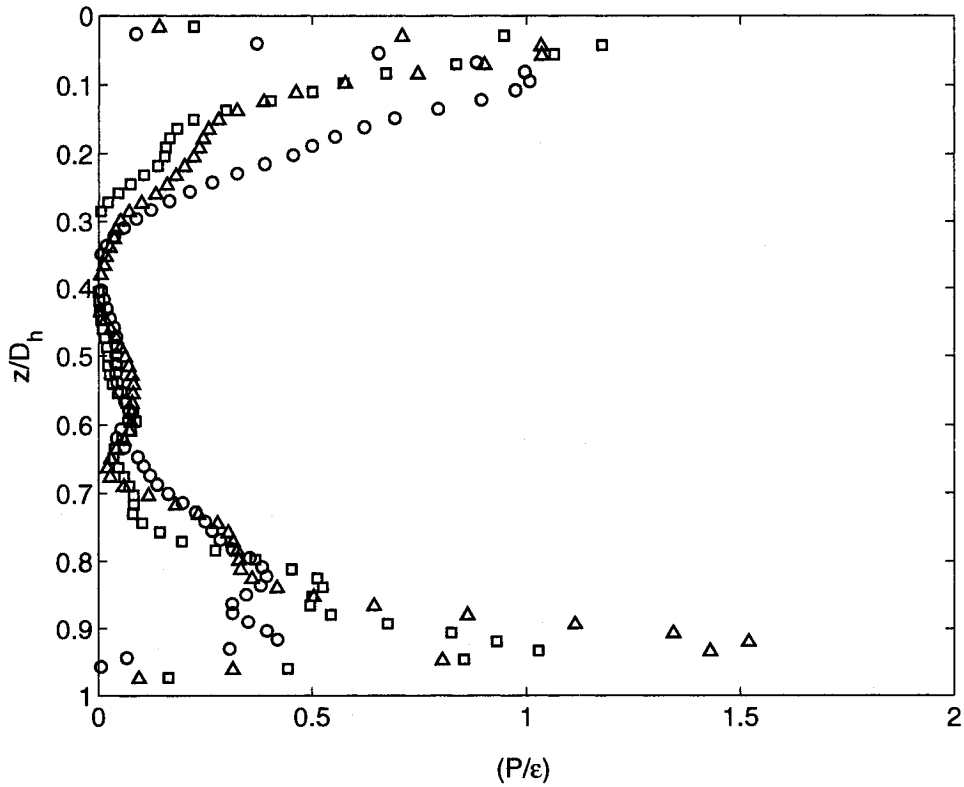

Figure 3.8: The production-dissipation ratio (P/ε) is plotted versus the channel depth. Re_τ = 164 (□), Re_τ = 144(Δ), Re_τ = 71 (○).

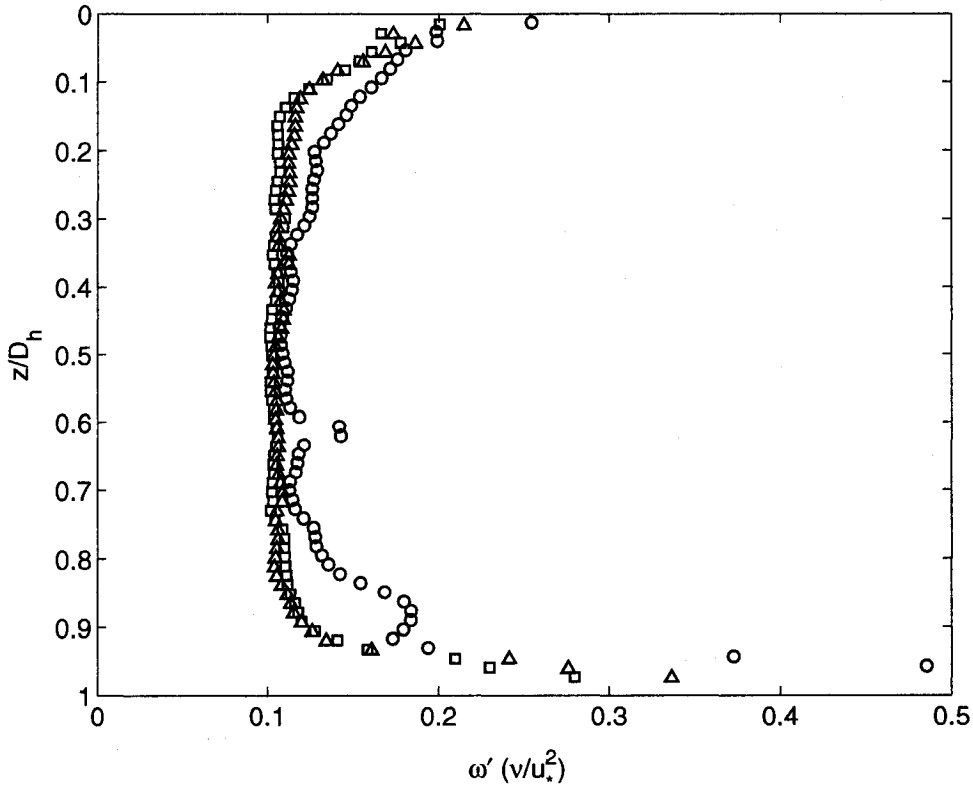

Figure 3.9: The RMS turbulent vorticity normalized by the rough surface friction velocity and kinematic viscosity versus the normalized channel depth. Dashed, $Re_\tau = 164$ (□), $Re_\tau = 144$(Δ), $Re_\tau = 71$ (○).

Chapter 4 - Influence of Wall Heating on the Flow Structure in the Near-wall Region

(Gajusingh and Siddiqui, 2006B)

The present chapter is focused on the experimental investigation of the impact of wall heating on the flow structure in the near-wall region inside a channel. Special emphasis has been paid on the direct comparison of the flow characteristics at the same location for the same inlet hydrodynamic conditions, in the presence and absence of wall heating. In addition, both laminar and turbulent flows were considered. This leads to a better insight into the physical mechanism(s) involved in this process for both flow regimes. A better knowledge of the influence of wall heating on the flow structure would help in improving the design and performance of thermal systems in particular, the heat exchangers. The experimental setup for this phase of experiments is presented in section 2.1 and 2.2.2. Four experimental runs were considered that correspond to the mass flow rates of 0.11, 0.70, 1.63 and 2.01 kg/s. Hereinafter, case I refers to 0.11 kg/s, case II to 0.70 kg/s, case III to 1.63 kg/s and case IV to 2.01 kg/s. For each mass flow rate two cases were studied, one with the aluminum plate unheated, and the other with the aluminum plate heated. Since with the addition of heat the volumetric flow rate and Reynolds number change due to the change in density and viscosity, the mass flow rate is considered as the reference parameter for each case for both heated and unheated conditions.

4.1 Mean Velocity

To check whether the flow was developed at the measurement location, the time-averaged streamwise velocity profiles near the upstream and downstream ends of the

camera field of view (3.2 cm apart) were compared for all cases. The average difference between the two velocity profiles was less than 5% for all cases except for the heated profile of case I where the difference was 6.7%. These differences were relatively small and thus, it was concluded that for all cases, the flow was developed.

Figure 4.1 shows the vertical profiles of the mean streamwise velocity. The mean streamwise velocity was computed by averaging the velocity data at each depth temporally and spatially. That is, for each experimental run, the time series were extracted at each grid point. The average velocity was obtained at each grid point by time-averaging. The time-averaged velocities at all grid points at a particular depth were then spatially averaged. This provided the spatial-temporal averaged velocity at each depth. In the present study, the depth, z, is referenced from the inner surface of the aluminum wall. That is, $z = 0$ is at the wall with the positive z-axis pointing upward towards the middle of the channel. The plot in figure 4.1 shows that for both heated and unheated cases, the mean streamwise velocity increased with an increase in the flow rate which is an expected behavior. It also shows that the mean streamwise velocity component for the unheated condition is greater than that for the heated condition for cases III and IV. The plot shows that within the measurement region, the streamwise velocity was reduced on average by 15% for case IV and 13% for case III when heat was added from the bottom plate. However, the opposite trend is observed for the two lower flow rates (i.e. cases I and II). That is, when heat was added, the mean streamwise velocity at these flow rates was increased by a factor of more than 2.5 in the close vicinity of the wall. However, as the distance from the wall increased, the magnitude of

the streamwise velocity became almost constant for some distance, and then started to decrease. It was also observed that at a distance of 1.8 to 2 cm from the wall, the velocity magnitudes for both heated and unheated cases became equal and further away from the wall, the velocity magnitude for unheated case become greater than the heated case.

The crossing of the velocity profiles for heated and unheated cases at a certain distance from the wall can be explained as follows. At a given condition, the mass flow rate of water was the same. For cases I and II, the average velocity in the near-wall region for heated condition was more than a factor of 2.5 larger than that for the unheated condition. The percentage decrease in the density due to heating was significantly lower than the percentage increase in the velocity. Thus, in the near-wall region, the mass flow rate for heated condition was greater than that for the unheated condition. To satisfy continuity, the mass flow rate of water for heated case must be decreased in some other region. Thus, the decrease in the streamwise velocity magnitude away from the wall for the heat case is to satisfy mass conservation. The same physical argument is also applicable to the higher flow rates (i.e. cases III and IV). In these cases it was observed that the mass flow rate in the near wall region for the heated condition is lower than the unheated condition, therefore, it is expected that in a region away from the wall (outside the measurement region), the streamwise velocity magnitude for the heated case would be greater than that for the unheated case. The reasons for the opposite trends in the mean streamwise velocity profiles at higher and lower mass flow rates will be discussed later.

4.1.1 Momentum and Displacement Thickness

The mean velocity profiles in figure 4.1 were used to compute displacement and momentum thicknesses. The values of the momentum and displacement thicknesses and the Reynolds number based on momentum thickness (Re_θ) are presented in Table 4.1 for all cases. The results show similar trend for both heated and unheated conditions. That is, for cases I and II, the displacement and momentum thicknesses increased with the mass flow rate, whereas, for cases III and IV, they decreased with an increase in mass flow rate. A similar trend was observed for Re_θ. Comparison between heated and unheated conditions shows that at a given flow rate, the displacement and momentum thicknesses and Re_θ were larger for the unheated condition. Arya (1975) estimated the boundary layer thickness for stable, unstable and neutral conditions for fully developed turbulent flow. For unstable case, he observed that for a given free stream condition, the boundary layer thickness decreased with the heat addition, which is consistent with our observation. Furthermore, the boundary layer thickness decreased with a reduction in instability. We observed the same trend for the turbulent cases under the heated condition. That is, the momentum and displacement thicknesses decreased from case III to case IV (see Table 4.1).

As mentioned in the experimental set up section, the electric heater was placed under the test section downstream of the trip section. Thus, for the heated cases, the trip section acts as an unheated starting length. Ameel (1997) showed that the average Nusselt number and the average plate temperature when the flow is laminar flow is more affected by an unheated starting length than when the flow is turbulent. As shown later, for unheated condition, cases I and II were in the laminar regime. Thus, it is expected that the

properties for these two cases under the heated condition would be more affected by the unheated starting length compared to cases III and IV.

4.2 Vertical Mean Streamwise Velocity Gradient

Figure 4.2 shows the vertical profiles of the mean streamwise velocity gradients. The plot shows that for all cases, the mean velocity gradients are relatively large in the near-wall regions and decreased with distance from the wall. This is an expected trend due to the no slip condition at the wall. The plot shows that in the near-wall region, the mean streamwise velocity gradient is larger for the heated condition for all Reynolds numbers. This could be due to the decrease in viscosity with the heat addition. The maximum velocity gradient in this region for the heated condition is approximately 1.3 times higher than that for the unheated condition for case III and IV, and more than a factor of two greater for cases I and II. The plot also shows that the strength of the gradients for all cases approaches zero for $z > 1.5$ cm.

The friction velocity was computed using equation (2.4). The mean streamwise velocity gradient was computed between the velocity data nearest to the wall and the velocity at the wall, where the latter is taken as zero due to the no slip condition. The values of the friction velocity for both heated and unheated conditions are presented in Table 4.1 for all cases. The results show that the friction velocity increased with the flow rate as expected. However, at a given flow rate, the comparison of the friction velocities for heated and unheated conditions shows that for case III and IV, the friction velocity decreased when

heat was added from bottom, whereas, for cases I and II, the friction velocity was increased with the heat addition.

4.3 Turbulent Velocities

The PIV measurements provide instantaneous velocity fields. The turbulent velocity fields were computed by subtracting the time-averaged mean velocity at each grid point, from the corresponding instantaneous velocity. From the turbulent velocity fields, a number of turbulent characteristics were computed. The profiles of the root-mean-square (RMS) streamwise and vertical turbulent velocity components are shown in figure 4.3 (a) and (b), respectively. The profiles in figure 4.3(a) show that the magnitude of the horizontal turbulent velocity is larger for the unheated condition for cases III and IV, whereas, the opposite trend (similar to figure 4.1) is observed for case I and II. That is, the horizontal turbulent velocity is larger for the heated condition. The plot also shows that for the unheated condition, the magnitudes of the turbulent velocity for cases I and II are very small except in the near-wall region. This indicates that for these two cases the flow is almost laminar. However, at the same flow rates, when heat is supplied, the turbulent intensity increased. For cases III and IV, the turbulent intensity was decreased with the heat addition. Furthermore, for cases III and IV under both conditions, the horizontal turbulent intensity increased with the distance from the wall up to approximately 3 mm, and then started to decrease towards the centerline. The maximum turbulent intensity was observed approximately at the same distance from the wall for both heated and unheated conditions. With the heat addition, the horizontal turbulent velocity decreased by approximately 25% within the 3 mm depth and by approximately

10% in the region away from the wall for cases III and IV. For cases I and II, the maximum horizontal turbulent intensity was observed in the close vicinity of the wall which decreased sharply up to a distance of 2 mm from the wall, and then remained approximately constant. The same trend was observed for both heated and unheated conditions. With the heat addition, the horizontal turbulent velocity for cases I and II was increased by approximately a factor of two.

The profiles of the RMS vertical turbulent velocity are shown in figure 4.3(b). The impact of heat addition at different flow rates was similar to that observed for the horizontal turbulent velocity. That is, at the two higher flow rates (cases III and IV), the magnitude of the vertical turbulent velocity decreased with the heat addition, whereas, at the two lower flow rates (cases I and II), the magnitude of the vertical turbulent velocity increased with the heat addition. The variation in the vertical turbulent velocity with the distance from the wall is similar for all cases. That is, the vertical turbulent velocity first decreased with the distance from the wall up to 1-2 mm, and then increased at greater heights, except for the unheated case at the two lower flow rates, where it stays almost constant with very small magnitude. As mentioned earlier, this could be due to the reason that the flow was in the laminar regime for these two cases. At the two lower flow rates in the region away from the wall, the vertical turbulent velocity was increased by almost a factor of five with the heat addition. This indicates that the flow that was in the laminar regime before heat addition, and became turbulent when heat was added. For case III in the region away from the wall, the magnitude of the vertical turbulent velocity was approximately the same for both heated and unheated conditions. However, in the near-

wall region, the vertical turbulent velocity was reduced on average by 50% with the heat addition. For case IV, the vertical turbulent velocity was reduced on average by 50% in the near-wall region and by 15% in the outer region when heat was added.

The trend observed in the vertical turbulent velocity profiles can be described as follows. At the low flow rates when the flow is in the laminar regime, the turbulence is produced with the heat addition, and the turbulent intensity is much stronger compared to the no heat case. As the flow rate is further increased, in the turbulent regime, the magnitudes of the vertical turbulent velocity become almost comparable and with a further increase in the flow rate, the vertical turbulent velocity for the heated condition become smaller than that for the unheated profile condition. For the horizontal turbulent velocity the trends are similar except for case III where the turbulent velocity for unheated condition was higher than the heated condition unlike the vertical turbulent velocity where both were almost equal. The results in figure 4.3 show strong turbulent fluctuations for the heated case at low flow rates (cases I and II).

4.4 Mean Kinetic Energy

The turbulent kinetic energy was computed using equation (2.5). The vertical profiles of the turbulent kinetic energy are plotted in figure 4.4. As the results in figure 4.3 shows that the magnitude of the horizontal turbulent velocity is higher than the vertical turbulent velocity in the near-wall region, the shape of the turbulent kinetic energy profiles in this region is similar to that of the horizontal turbulent velocity. In the outer region, the horizontal velocity decreases and the vertical velocity increases, with comparable

magnitudes, which resulted in the almost constant turbulent kinetic energy in the outer region. The comparison between the heated and unheated profiles conditions shows that when heat is added, the turbulent kinetic energy is decreased for cases III and IV, and, increased for cases I and II.

4.5 Reynolds Stress

The Reynolds stress ($-\overline{u'w'}$) profiles are presented in figure 4.5 as a function of depth. The plot shows that at higher flow rates (i.e. case III and IV), the profiles for both heated and unheated cases show the classical behavior. That is, the Reynolds stress increased with the distance in the near-wall region to a peak value and then decreased towards the outer region. The plot also shows that at these Reynolds numbers, the magnitude of the Reynolds stress is higher for the unheated profile condition. At lower flow rates (i.e. case I and II), a different trend is observed. For the unheated profile condition, the Reynolds stress is almost zero, confirming that the flow was in the laminar regime at these two flow rates in the absence of heat. When heat was added at these flow rates, the Reynolds stress profiles showed the classical trend up to a distance of 1 cm from the wall and then the Reynolds stress became negative while its magnitude increased with distance up to z = 2 cm after which it began to decrease. These results indicate that in the near-wall region, the turbulence extracted energy from the mean flow through the positive Reynolds stress, while in the outer region the energy is transferred from turbulence to the mean flow through the negative Reynolds stress.

4.6 Turbulent Energy Production

The turbulent kinetic energy production due to the mean shear can be computed using equation (2.2). The vertical profiles of the turbulent kinetic energy production are plotted in figure 4.6 as a function of depth. The overall trend in the production profiles is similar to the classical profiles of wall bounded flows. That is, the turbulent energy production increased very sharply from zero to a peak value in the near-wall region and then decreased towards the outer region. The higher production in the near-wall region is due to the higher magnitudes of the Reynolds stress and the mean velocity gradients in this region. As the distance from the wall increases, the magnitudes of both the Reynolds stress and the mean streamwise velocity gradients decrease resulting in a decrease in the energy production, which approaches zero near the channel core. As mentioned earlier, for unheated condition at the two lower flow rates, the flow was in the laminar regime. The results in figure 4.6 further confirm this by showing that the energy production is zero for these two cases. The plot also shows that for the heated condition at the same flow rates, the energy production is also almost zero except in the near wall region where energy production due to the mean shear (although very small in magnitude) exists. The Reynolds stress profiles for these cases in figure 4.4 showed negative Reynolds stress at heights $z > 1$ cm. Thus, we expect negative production in this region. However, the mean stream velocity gradients in this region for these two cases are also negative although very small in magnitude (see figure 4.2). Thus, the net effect is positive energy production with a negligible magnitude in this region. The results in figure 4.6 indicate that for these cases (i.e. cases I and II), the turbulence due to the mean shear is negligible and the turbulence is primarily generated by the buoyancy flux. Thus, it can be concluded that in channel flows which are initially laminar in the absence of heat transfer, when heat

is supplied to create unstably stratified regime, the turbulence generation is almost entirely due to the buoyancy flux.

For the two higher flow rate cases (i.e. cases III and IV), the plot shows that for a given flow rate, the energy production is higher for the unheated condition compared to the heated one. The mean velocity gradients are higher for the heated condition, but the Reynolds stress is higher for the unheated condition. Since the percentage increase in the mean velocity gradients is lower than the percentage decrease in the Reynolds stress when heat is added, the overall effect is a reduction in the energy production. The plot shows that at both higher flow rates, the maximum energy production is reduced by approximately 30% when heat is added to the flow.

4.7 Turbulent Energy Dissipation

The rate of turbulent kinetic energy dissipation was computed using the direct method of equation (2.3). The rate of energy dissipation is plotted in figure 4.7 as a function of depth. The plot shows, as expected, that the rate of energy dissipation is largest adjacent to the wall, which decreased with the distance from the wall and became almost constant in the outer region. For cases I and II, the dissipation is almost negligible, except near the wall, where the dissipation rate for the heated condition is higher than the unheated one. For cases III and IV, the plot shows that the dissipation rate is higher for the unheated condition.

4.8 Discussion

Results in the previous section show that when a flow is unstably stratified via heating through a bottom wall, both the mean and turbulent characteristics are affected. We have considered four cases, two of which correspond to the laminar regime in the absence of heat (cases I and II) and the other two correspond to the turbulent regime (cases III and IV). The results have shown that the impact of wall heating on the flow behavior is significantly different for the laminar and turbulent flows. It was found that when a flow that is originally laminar is heated, the mean streamwise velocity in the near-wall region is significantly increased and turbulence is generated in the flow. Thus, a flow that is originally laminar becomes turbulent with the heat addition. However, when the flow is in the turbulent regime, addition of heat reduces the magnitudes of mean streamwise velocity and turbulent properties.

For the heated cases in the present study, there are two mechanisms of the turbulence production, one is the mean shear and the other is the buoyancy flux. The relative magnitudes of the turbulence production due to the buoyancy and mean shear is quantified in terms of the gradient Richardson number (R_i) which is defined as,

$$R_i = -g\frac{\partial \rho}{\partial z}\Big/\rho\left(\frac{\partial U}{\partial z}\right)^2 \tag{4.1}$$

where, $\partial\rho/\partial z$ is the vertical density gradient and g is the acceleration due to gravity (Turner 1973). When $R_i < 0$, the flow becomes thermally unstable. As mentioned in the experimental setup section, the temperature was measured in the near-wall region in a separate set of experiments under the identical conditions. The values of R_i were

computed from the temperature data. The values of R_i in the near-wall region for all heated cases are presented in Table 4.1. The results show that the magnitude of the Richardson number is largest for case I and decreased monotonically to case IV. This indicates that the turbulence production due to buoyancy is more dominant at the lower flow rates compared to the higher flow rates. When the flow is unheated, the only source of turbulence is the mean shear. The results show that for unheated condition at low flow rates, the turbulent intensities are almost negligible and the turbulence production due to the mean shear is almost zero. This indicates that in the absence of heat transfer, the flow is in the laminar regime. When heat is applied, the magnitude of turbulent intensities increased drastically, however, the magnitude of the turbulent kinetic energy production due to the mean shear remained close to zero. This implies that the strong turbulent intensities observed for these cases are due to the turbulence production by buoyancy. Turner (1973) argued that for thermally stratified flows, the Reynolds number for the transition to turbulence depends on the Richardson number. The present results confirm this argument by showing that a flow in the laminar regime at relatively low Reynolds number could become turbulent when unstable thermal stratification is introduced. That is, when heat is supplied from the bottom. In the present study however, we are not able to estimate the critical Richardson number for the transition.

In the turbulent regime (i.e. cases III and IV), the Richardson number is several orders of magnitude lower than that for cases I and II. This indicates that the impact of buoyancy on turbulence production is relatively small and mean shear is the dominant mechanism of turbulence production. The results show that in this regime, the magnitude of the

turbulent characteristics decreased when heat is added. This trend is opposite to that observed at lower flow rates. Turner (1973) argued that in stratified fully developed turbulent flows where the Richardson number is small, the turbulent kinetic energy is systemically removed over a range of wavenumbers by working against buoyancy forces. He further argued that the energy production due to the mean shear is balanced by the rate of working against the buoyancy forces and the viscous dissipation. Townsend (1958) estimated the ratio of the total energy loss to energy production (due to the mean shear) in a stratified flow and plotted it versus the turbulent intensity for various buoyancy effects. The plot shows that the total energy loss to energy production ratio increases with an increase in the buoyancy effects. The plot also shows that for a given turbulent intensity, this ratio is always higher for the stratified flow compared to the unstratified flow, where in the latter the energy loss is entirely due to viscous dissipation. This indicates that in a fully turbulent flow at a particular flow rate (i.e. case III or IV), when the flow becomes stratified, the turbulence works against the buoyancy forces resulting in a decrease in the turbulent intensity as observed in Figs. 4.3 and 4.4. A decrease in the turbulent intensities resulted in a decrease in Reynolds stress and thus, the energy production as seen in Figs. 4.5 and 4.6. Similarly, due to the reduction in energy production and turbulent intensities, the rate of viscous dissipation is also reduced as evident in figure 4.7.

These results indicate that the effect of stratification on the flow structure is significantly different for the flow that is originally in the laminar regime compared to that in the turbulent regime. For the same flow rate, in the laminar regime, stratification leads to the

transition to turbulent regime if the Richardson number is higher than certain critical value. However, in the turbulent regime, stratification leads to the decrease in turbulence level due to its work against the buoyancy forces. Furthermore, in unstratified flows the transition from laminar to turbulent regimes occurs with an increase in the Reynolds number and turbulence is produced by the mean shear. However, when a laminar flow becomes turbulent due to the stratification (in the same range of Reynolds number), the turbulence production due to the mean shear remains negligible and the turbulence is produced almost entirely due to buoyancy.

The mean velocity profiles in figure 4.1 also show a trend similar to that of the turbulent properties. That is, for cases I and II, the mean velocity is increased in the near-surface region when heat is added, whereas, for cases III and IV, the mean velocity is decreased with the addition of heat. One plausible explanation for this tend is that in the laminar regime where the Reynolds number is low, the viscous effects are relatively more significant than that at in the turbulent regime where the Reynolds number is high. Thus, when heat is added, the viscosity of the fluid is reduced which resulted in an increase in the mean velocity in the near-wall region. At higher Reynolds numbers in the fully turbulent regime where the viscous effects are insignificant, the decrease in viscosity has no significant impact on the mean velocity in the near-wall region. However, this reason cannot explain the trend of decrease in mean velocity with the heat addition. The reason for this trend is still under investigation.

Table 4.1: Properties for different cases; E, uncertainty in velocity measurements; Re_θ, Reynolds number based on maximum velocity of the channel the momentum thickness.

Case		**I**	**II**	**III**	**IV**
Mass Flow rate (kg/s)		0.11	0.70	1.63	2.01
Wall Temperature (°C)		32.6	31.2	29.7	29.9
Richardson Number		-0.4684	-0.2773	-0.003	-0.001
Δt (ms)	Unheated	25	10	4	3
	Heated	20	8	4	3
E (%)	Unheated	4.14	6.43	2.86	2.96
	Heated	4.39	6.71	3.08	3.34
Momentum Thickness (cm)	Unheated	0. 209	0.249	0.212	0.161
	Heated	0.118	0.135	0.179	0.143
Displacement Thickness (cm)	Unheated	0.366	0.506	0.289	0.204
	Heated	0.154	0.178	0.241	0.187
Re_θ	Unheated	18	28	127	120
	Heated	11	16	93	89
u_* (cm/s)	Unheated	0. 100	0.094	0.280	0.318
	Heated	0.133	0.176	0.300	0.327

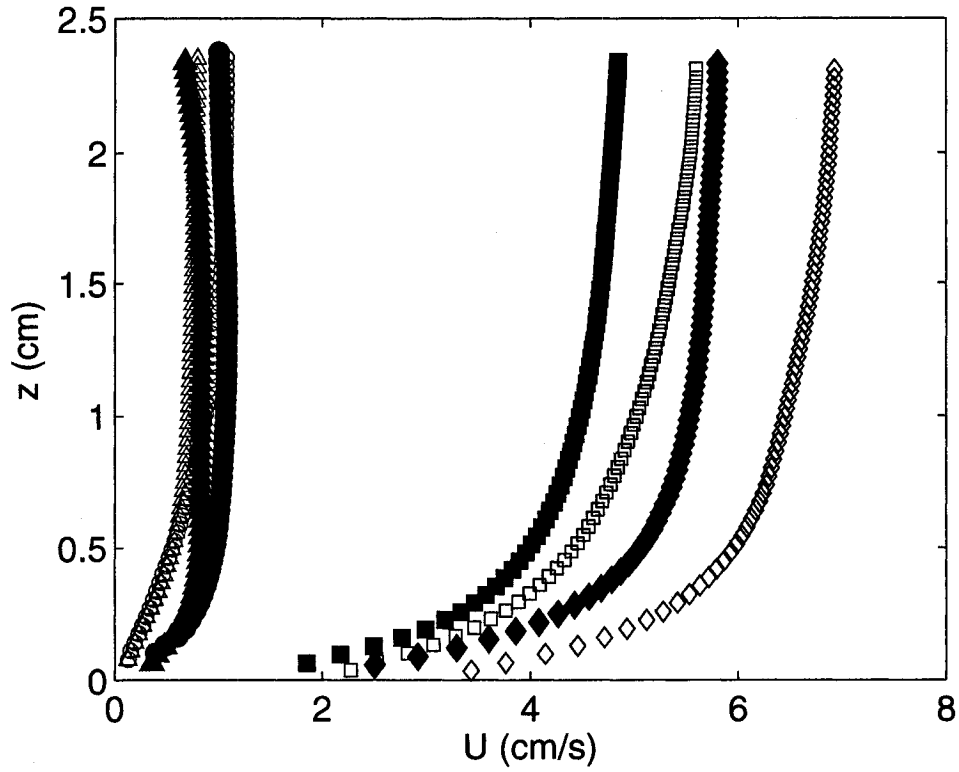

Figure 4.1: Vertical profiles of the mean streamwise velocity. Case I (-Δ-), Case II (-o-), Case III (-□-) and Case IV (-◊-). Open symbols: unheated condition; closed symbols: heated condition.

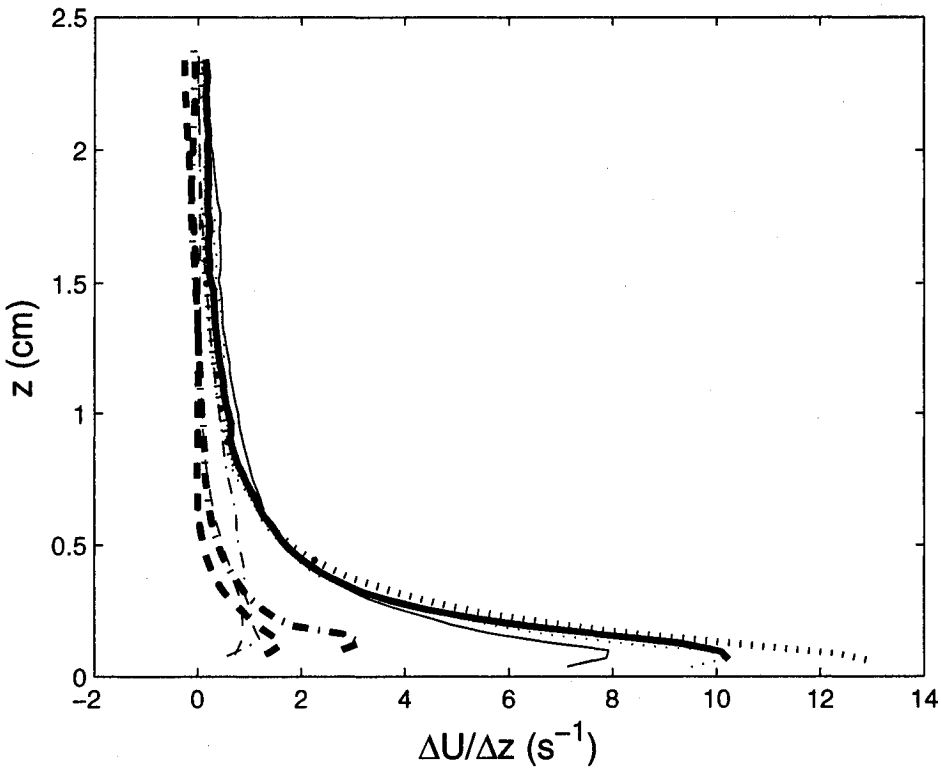

Figure 4.2: Vertical profiles of the mean streamwise velocity gradients ($\Delta U/\Delta z$). Dashed, Case I; dash-dotted, Case II; solid, Case III; dotted, Case IV. Thin line: unheated condition, thick line: heated condition.

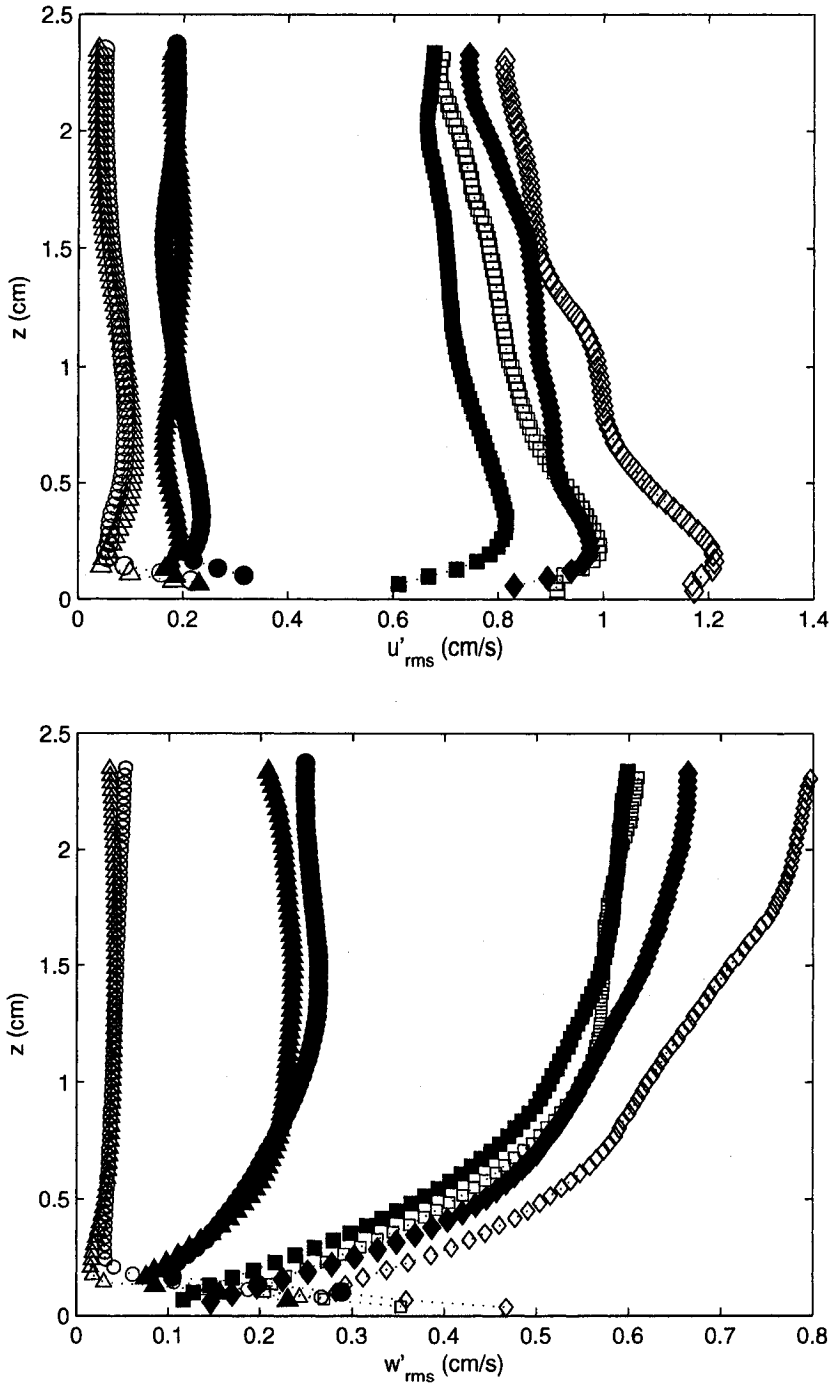

Figure 4.3: The plots of (a) RMS streamwise turbulent velocity, (b) RMS vertical turbulent velocity, versus the height from the wall. Case I (-Δ-), Case II (-o-), Case III (-□-) and Case IV (-◊-). Open symbols: unheated condition; closed symbols: heated condition.

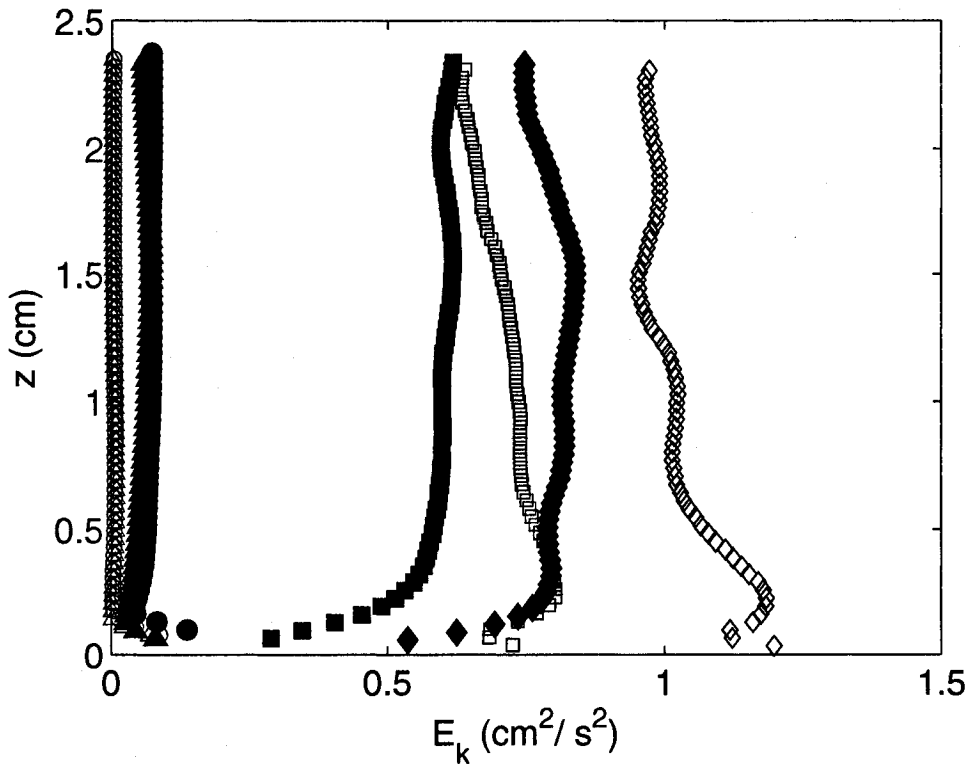

Figure 4.4: The mean kinetic energy is plotted versus the height from the wall. Case I (-Δ-), Case II (-o-), Case III (-□-) and Case IV (-◊-). Open symbols: unheated condition; closed symbols: heated condition.

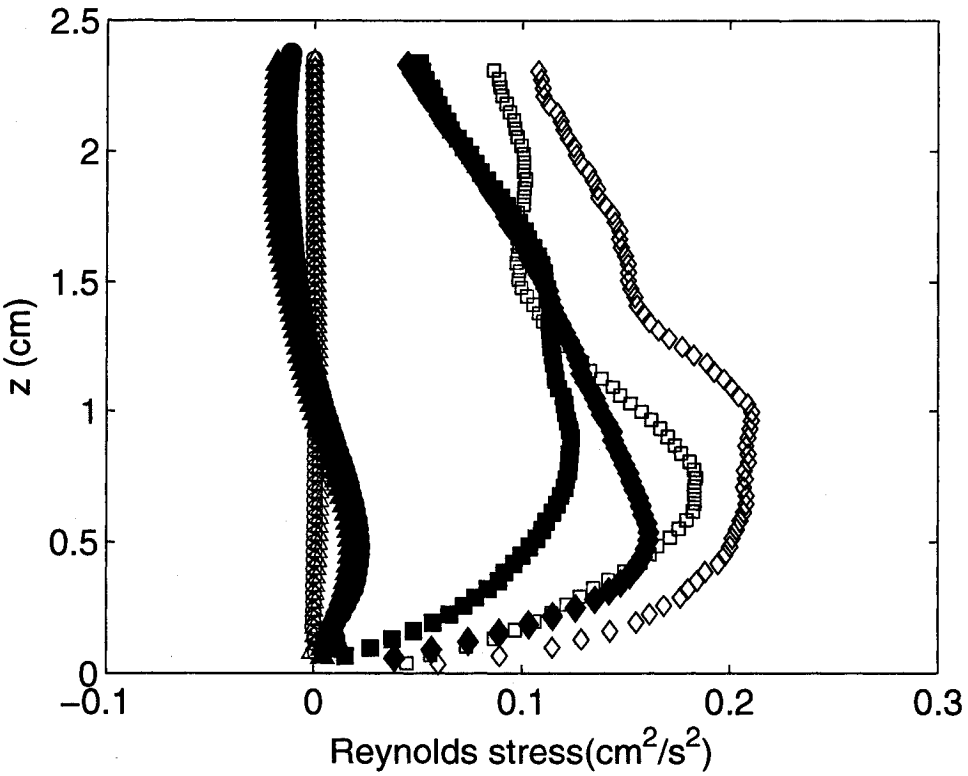

Figure 4.5: Vertical profiles of the Reynolds Stress. Case I (-Δ-), Case II (-o-), Case III (-□-) and Case IV (-◊-). Open symbols: unheated condition; closed symbols: heated condition.

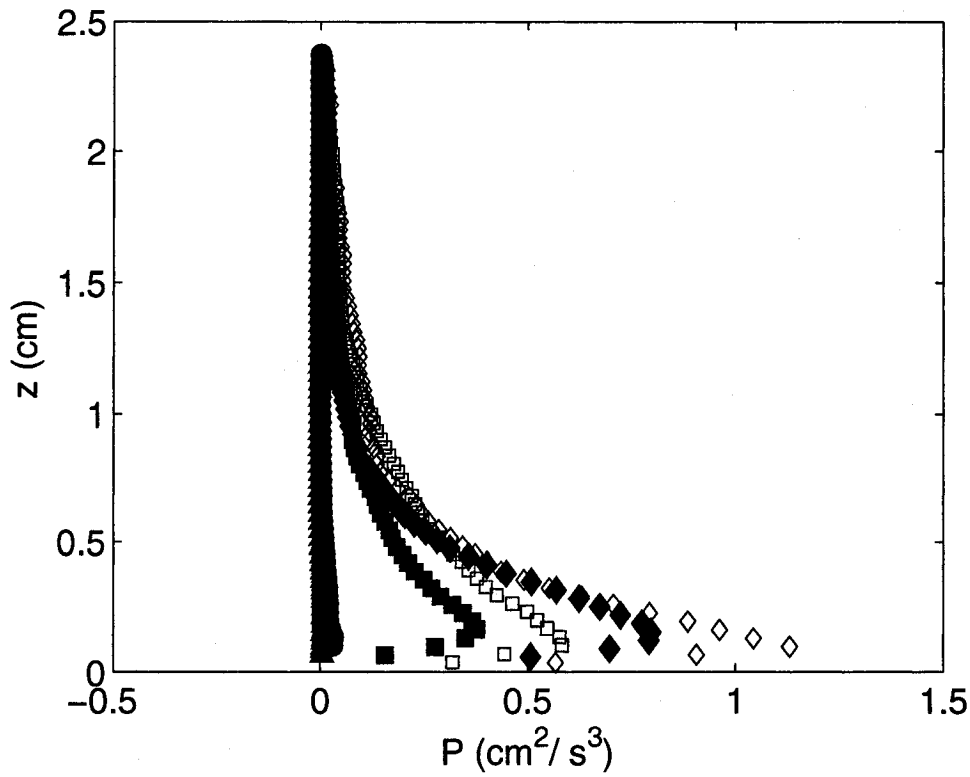

Figure 4.6: Vertical profiles of the rate of turbulent kinetic energy production. Case I (-Δ-), Case II (-o-), Case III (-□-) and Case IV (-◊-). Open symbols: unheated condition; closed symbols: heated condition.

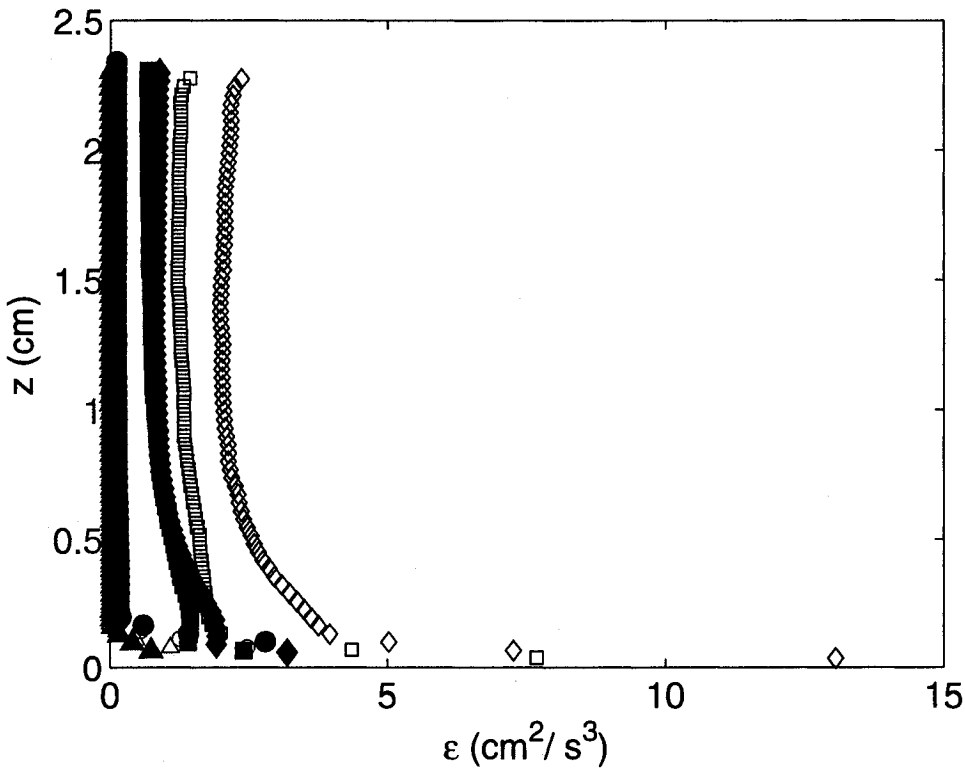

Figure 4.7: Vertical profiles of the rate of turbulent kinetic energy dissipation. Case I (-Δ-), Case II (-o-), Case III (-□-) and Case IV (-◊-). Open symbols: unheated condition; closed symbols: heated condition.

Chapter 5 - Influence of a Single Baffle on the Downstream Flow Structure

The present chapter is focused on the investigation of the impact of a single rectangular baffle (which acts as a vortex generator), on the overall mean and turbulent characteristics of a flow in a channel downstream of a baffle. This would help in understanding how the flow characteristics are affected locally by the insertion of a vortex generator. The experimental apparatus used for these experiments is already described in chapter 2 (see sections 2.1 and 2.2.3). In this set of experiments, three experimental cases were considered. The Reynolds numbers (Re_τ) based on the friction velocity and half of the hydraulic diameter for these cases are 66, 134 and 152, respectively. Hereinafter, they are considered as cases I, II and III, respectively. For all plots presented in this chapter, the streamwise length, x, is referenced from the upstream end of the test section. Thus, the upstream edge of the PIV field of view corresponds to x = 47.4 cm and the downstream edge of the PIV field corresponds to x = 59.6 cm.

5.1 Mean Velocity

The mean streamwise velocity was computed by time-averaging the velocity data at each grid point. The two-dimensional mean velocity fields at the lowest and highest Reynolds numbers (Re_τ = 66 and 152) are presented in figures 5.1(a) and (b), respectively. The plots represent the typical flow behavior past a vertical obstruction. The plots show that in both cases, the flow appears to be most affected by the baffle in the surrounding region

with the flow separation off the upper edge of the baffle. Both plots exhibit strong vertical motion just downstream of the baffle. The magnitude of the separation vortex, as expected, increased with the Reynolds number. The plot also shows stagnation areas adjacent to the baffle near the wall, which is also observed in previous studies for example, Leonardi *et al.* (2004). The longitudinal vortex induced by the baffle enhances mixing and thus, the surface heat transfer. Since we are interested in the flow structure modified by the baffle, the results in all subsequent plots are focused in the region downstream of the baffle. As the plots in figure 5.1 have shown that in the region downstream of the baffle, there is a significant spatial variation in the flow. Thus, any horizontally-averaged parameter will not be able to correctly quantify these variations in this region. Therefore, in order to capture the true dynamics in this region, various parameters are analyzed at specific spatial locations. The selected spatial locations are at x = 51.4, 52.2, 53.7 and 58 cm. These locations cover the spatial extent of the flow within the given field of view from x = 51.4 cm which is immediately downstream of the baffle to x = 58 cm which is close to the downstream end of the field of view where the flow reattaches itself.

The influence of baffle on the flow structure can be quantified by comparing the flow characteristics downstream of the baffle with that of the flow without a baffle. In Chapter 3, we measured flow characteristics in the same channel without any obstruction under similar conditions. Thus, the comparison of flow characteristics downstream of baffle with that presented in Chapter 3 would provide the influence of the baffle on the flow behavior quantitatively. Although the experimental conditions were similar during both

sets of experiments, however, the Reynolds numbers were not exactly the same. Similarly, the roughness of bottom wall in both cases was different (aluminum for no baffle case and Plexiglas for baffle case). Therefore, the flow properties for both cases are compared in the non-dimensional form at different spatial locations mentioned above. It should be noted that the flow characteristics for no baffle case presented in Chapter 3 are for the developed flow. Therefore, for no baffle case, the same properties are presented at all spatial locations.

The mean velocity profiles normalized by the friction velocity at different Reynolds numbers are plotted in figure 5.2 (a)-(d) at the streamwise locations x = 51.4, 52.2, 53.7 and 58 cm, respectively. The profiles are normalized with their respective friction velocity. The friction velocity at different Reynolds numbers for the baffled case was computed the same way as for the cases in Chapters 3 and 4. That is, the mean velocity gradient at the wall was computed between the bottom wall and the mean streamwise velocity at the first data point above the wall, where, the velocity at the wall was taken as zero due to the no slip condition. The mean streamwise velocity was computed by spatially and temporally averaging the instantaneous streamwise velocity in the region downstream of the baffle. The values of friction velocity for all Reynolds number cases are presented in Table 5.1.

The plots in figure 5.2 shows that for all three cases, the two closest locations to the baffle, i.e. x = 51.4 to 53.7cm, contain a negative streamwise velocity component in the near wall region. This is an expected trend due to the increased circulation in this region

caused by the baffle. This region is also clearly seen in figure 5.1. It is shown that the flow begins to recover from the disturbance at x = 53.7cm and the profiles return a classical profile of a flow over a flat plate by x = 58cm, although the magnitude has been significantly increased when compared to the no-baffle case. The slight decrease in magnitude above $z/D_h = 0.6$ is attributed to the fact that the flow is approaching the other bounding wall at which the velocity must equal zero to satisfy the no slip condition. The plots show some discrepancies in the data in the region $0.5 < z/D_h < 0.7$ at $x = 51.4$ for $Re_\tau = 134$. This is due to localized errors in the data set caused by bubbles that had adhered to the wall during the acquisition at $Re_\tau = 134$ only. In the outer region of the flow, just downstream of the baffle, the velocity was increased by 3, 6 and 7 times for Re = 66, 134 and 152, respectively, when compared to the no-baffle case. This is due to the reason that the baffle cases a reduction in cross-sectional area and for mass conservation, the flow accelerates. The significant variation in the mean streamwise velocity was found up to approximately $z/D_h = 0.3$ in figure 5.2 (a) – (c) for the baffle case at all three Reynolds numbers. This is approximately three times further away from the bottom wall compared to that for the no-baffle case where it was observed around $z/D_h = 0.1$ in all three profiles. This distance increased to $z/D_h = 0.5$ at x = 58cm, i.e. five times the distance of the no-baffle case.

5.2 Vertical Mean Streamwise Velocity Gradients

The vertical profiles of the mean streamwise velocity gradients normalized by the hydraulic diameter (D_h) and friction velocity are presented in absolute form in figures 5.3 (a) – (d) at the streamwise locations $x = 51.4$, 52.2, 53.7 and 58 cm, respectively. The

profiles of the mean streamwise velocity gradients for the no baffle case are also plotted in the figure for comparison. The plots show that the mean velocity gradients for the baffle case increased with the distance from the wall to a peak value at $z/D_h \approx 0.17$ and then decreased towards the channel core. The gradients again started to increase with z as they approach the upper wall. The gradient profiles at different streamwise locations show that immediately downstream of the baffle (i.e. at $x = 51.4$ cm), the increase in the magnitude of velocity gradient is very sharp. They increased by more than an order of magnitude from $z/D_h = 0$ to $z/D_h \approx 0.17$ and then decreased by more than two orders of magnitude to a height $z/D_h \approx 0.3$ where they almost vanished. As the downstream distance from the baffle increased, the magnitude of the maximum velocity gradient decreased. At $x = 58$ cm, the increase in the gradient magnitude was reduced to a factor of two. However, at all downstream distances, the peak stays at approximately the same height from the wall (i.e. $z/D_h \approx 0.17$) which is equal to the height of the baffle. Although the minima shifted away from the wall as the streamwise distance from the baffle increased. The minima shifted from $z/D_h \approx 0.3$ immediately downstream of the baffle to $z/D_h \approx 0.46$ at $x = 58$ cm. These heights correspond to two and three times the baffle height, respectively. The profiles of the mean velocity gradients for the no-baffle case show that the gradients reach a peak value immediately above the wall and then continue to decrease towards the channel core. Comparison of the profiles for both cases shows that when a baffle is inserted into the flow, within a distance equal to two to three baffle height from the wall, the mean velocity gradients are increased on average by almost an order of magnitude.

5.3 Turbulent Velocities

The PIV measurements provide instantaneous velocity fields. The turbulent velocity fields were computed by subtracting the time-averaged mean velocity at each grid point, from the corresponding instantaneous velocity. Various turbulent characteristics were computed from the turbulent velocity fields. The normalized profiles of the root-mean-square (RMS) streamwise turbulent velocity components are shown in figure 5.4 (a) - (d) at different spatial locations. The profiles of the RMS streamwise velocity for no baffle case are also plotted for comparison.

The plots show that the normalized profiles of turbulent intensity for the fully turbulent cases (Re_τ = 134 and 152) collapsed well, however, the profile at Re_τ = 66 did not collapse. This could be due to the reason that the flow at this Reynolds number is in the transition regime and therefore, the turbulence is not fully developed. Comparison of the streamwise turbulent intensity for baffle and no-baffle cases shows that at all spatial locations presented here, the streamwise turbulent intensity is enhanced by an order of magnitude when the baffle is inserted in the flow. In the region immediately downstream of the baffle, a sharp peak in the streamwise turbulent intensity was observed at a distance of z/D_h = 0.17, at all Reynolds numbers (see figure 5.4(a)), which is equal to the baffle height. The plot shows that the turbulent intensity was increased by almost a factor of three from the wall to the peak value and then decreased sharply to a distance z/D_h = 0.3 (correspond to twice the baffle height) and then decrease slowly towards the channel core. At further downstream locations, the plots show that the sharpness of the peak is decreased, however, the location of the peak was almost the same. These results indicate

that when a baffle is inserted into the flow, the turbulence is enhanced throughout the channel. However, sharp increase in streamwise turbulent intensity was observed in a layer adjacent to the wall. The thickness of this enhanced turbulence layer is approximately equal to twice the baffle height at the location immediately downstream of the baffle, which increased to approximately three times the baffle height as the downstream distance increased to x = 58 cm. These results indicate that the enhanced turbulence layer grows with the distance from the baffle. This trend is significantly different from the no baffle case, where the streamwise turbulent intensity has a peak very close to the wall and then decreased gradually towards the channel core. Figure 5.4 (a) shows that at x = 51.4 cm, the magnitude of the turbulent intensity is almost constant at the two higher Reynolds numbers up to $z/D_h = 0.05$. This is due to the reason that this region represents a stagnation area where the flow re-circulates (see figure 5.1). A similar trend in the turbulent intensity profile in this region was also observed by Leonardi *et al.* (2004). The results also show that the magnitude of the normalized turbulent intensity at the two higher Reynolds numbers (Re_τ = 152 and 134) is twice that at Re_τ = 66 for the entire depth. This is most likely due to the reason that at Re_τ = 66, the flow is in the transition regime and the turbulence is not fully developed.

Similar trends were observed for the normalized RMS vertical turbulent velocity profiles shown in figure 5.5(a) – (d). The location of the peak of vertical turbulent velocity was also at the same height (i.e. the baffle height) and the thickness of the enhanced vertical turbulent velocity layer was also increased with the streamwise distance from the baffle. Similar to the streamwise turbulent velocity, the profiles of the vertical turbulent velocity

for the baffle and no-baffle cases show that the vertical turbulent velocity was enhanced by approximately an order of magnitude when a baffle is inserted into the flow. The lower magnitude of the normalized vertical turbulent velocity at $Re_\tau = 66$ could be due to the same reason as mentioned above, that is, the flow is in the transition regime and the turbulence is not fully developed. Comparison of the magnitudes of streamwise and vertical turbulent velocities for baffle case at two higher Reynolds numbers shows that throughout the vertical region, the streamwise turbulent velocity was larger in magnitude than the vertical turbulent velocity.

5.4 Turbulent Kinetic Energy

The turbulent kinetic energy can be computed using equation (2.5). The profiles of the normalized turbulent kinetic energy for baffle and no-baffle cases are presented in figures 5.6 (a) – (d), for the three Reynolds number cases. Since the turbulent kinetic energy depends on the streamwise and vertical turbulent intensities, the trends in the profiles of the turbulent kinetic energy are similar to those of the streamwise and vertical turbulent intensities, presented in figures 5.4 and 5.5. Comparison of the turbulent kinetic energy magnitude for baffle and no baffle cases shows that the turbulent kinetic energy is increased by almost two orders of magnitude when a vertical baffle is inserted into the flow. Similar to figures 5.4 and 5.5, the plots in figure 5.6 show that the turbulent kinetic energy is sharply increased in the near-wall region to a peak value and then decreased sharply to a distance approximately equal to twice the baffle height and then decreased very slowly with height. The maximum kinetic energy is observed at a distance from the

wall equal to the baffle height and the peak tends to get flatted as the streamwise distance from the baffle increases.

5.5 Reynolds Stress

The profiles of the normalized Reynolds Stress for baffle and no-baffle cases are presented in absolute form in figures 5.7(a) – (d) for all Reynolds number cases. The results show that the Reynolds stress is significantly enhanced in the presence of baffle for all cases. In conventional channel flows as depicted in the profiles of no-baffle case, the Reynolds stress increases sharply near the wall and then decreases gradually towards the channel core where it almost diminishes. However, as the results in figure 5.7 shows, the vertical profiles of Reynolds stress change drastically in the presence of a baffle. The first major difference was the shift in the Reynolds stress peak away from the wall to a height approximately the same as the baffle height. Unlike the no-baffle case where the Reynolds stress decrease gradually towards the channel core, the Reynolds stress decreased sharply towards the core for the baffle case. The results also show that the trend of the Reynolds stress profile changed significantly as the downstream distance from the baffle increased. Immediately downstream of the baffle (i.e. at x = 51.4 cm), the Reynolds stress increase sharply to a distance equal to the baffle height and then decreased sharply to a distance approximately equal to twice the baffle height. The Reynolds stress started to increase again with a further increase in the distance from the wall to a peak value and then decreased to a minimum value at a height $z/D_h \approx 0.68$ (which correspond to 4.5 cm from the wall) and then started to increase towards the upper wall. The magnitude of the second peak is significantly smaller than the first peak which

is located at a distance equal to the baffle height. This indicates that in the region immediately downstream of baffle, three layers exist inside the channel. In each of the three layers, the Reynolds stress increases towards the center of the layer. However, the most significant enhancement in the Reynolds stress is observed in the bottom layer. With an increase in the streamwise distance from the baffle, the thickness of the bottom layer increases and at a farther distance (i.e. x = 58 cm), the middle layer is merged partially into the top and bottom layers and the profiles appear similar to that of the no baffle case. However, the peak in the bottom layer stays at the same height. The results in figure 5.7 also show that Reynolds stress in all these layers was significantly enhanced compared to the no baffle case. Results in figure 5.7 also indicate that the normalized magnitude of Reynolds stress for $Re_\tau = 66$ is lower than the other two cases, which is due to the same reason as mentioned earlier, that is, the transition regime.

5.6 Turbulent Energy Production

The rate of turbulent kinetic energy production can be computed using equation (2.2). The normalized turbulent energy production profiles for baffle and no baffles cases are presented in absolute form in figures 5.8(a) – (d) at different streamwise locations. The data was normalized with the hydraulic diameter and the friction velocity. As equation (2.2) indicates that the rate of turbulent energy production is the product of the Reynolds stress and mean streamwise velocity gradients, the trend and magnitude of the production profiles are similar to those of the mean velocity gradients (figure 5.3) and Reynolds stress (figure 5.7). The results in figure 5.8 show that the rate of turbulent kinetic energy production is enhanced by three to four orders of magnitude when a baffle is inserted in a

channel. The maximum energy production is observed at a distance equal to the baffle height. The thickness of this enhanced layer of energy production is equal to twice the baffle height in the region immediately downstream of the baffle, which increased to three times the baffle height at a distance further downstream. Similar to the previously presented turbulent characteristics, the results in figure 5.8 also indicate that the baffle influenced the flow not only in the vicinity of the baffle but throughout the channel as the rate of turbulence production away from the baffle i.e. $z/D_h > 0.5$ is still more than an order of magnitude higher than the no baffle estimates.

5.7 Turbulent Energy Dissipation

The rate of turbulent kinetic energy dissipation was computed using equation (2.3). The normalized rate of energy dissipation for both baffle and no baffle cases is plotted in figure 5.9 (a) – (d) as a function of normalized depth at different streamwise locations. The plots show that the dissipation rate is significantly enhanced when a baffle is inserted in a channel. However, the trend of the dissipation rate profile in the presence of a baffle is different from that of the no baffle case, in the near-wall region. The plots show that for the no baffle case, the rate of turbulent kinetic energy dissipation is maximum immediately adjacent to the wall, which decreases with the distance from wall to a height $z/D_h \approx 0.3$ and then stays almost constant over the remaining height presented in the plots. However, in the presence of a baffle, the dissipation rate is first decreased in a thin layer immediately adjacent to the wall and then started to increase with the distance from the wall to a location equal to the baffle height. With a further increase in the distance the dissipation rate decreased to a location two to three times the baffle height (depending on

the streamwise location) and then becomes almost constant over the remaining distance. Within the thin layer immediately adjacent to the wall, the dissipation rates for the no-baffle was one order of magnitude smaller than that in the absence of baffle. However, in the region, $0.05 < z/D_h < 0.3$, the dissipation rate in the presence of baffle was more than two orders of magnitude higher than that in the absence of baffle, with the peak value approximately three orders of magnitude higher in the region near the baffle. At heights $z/D_h > 0.4$ where the dissipation profiles are almost constant for both cases, the dissipation rate in the presence of a baffle was enhanced by approximately two orders of magnitude. The plots show some outliers in the data in the region $0.5 < z/D_h < 0.7$ at x = 51.4 and 53.7cm for $Re_\tau = 134$. These are due to the bubbles that had adhered to the wall during the data acquisition for this case.

5.8 Discussion

In the present study, we have introduced a single obstruction, that is, a vertical baffle of 1 cm height. The results presented in the previous section have demonstrated that the introduction of the baffle into the flow, which acts as an obstruction, has significantly altered the flow characteristics downstream of the baffle. The main objective of the present work was to quantify the influence of an obstruction on the flow behavior in the channel. As mentioned earlier, in the introduction section, no previous study had reported any detailed quantitative analysis of this nature. To fully explore this issue it is important to find the relationships between the geometrical properties of the obstruction and the downstream flow characteristics. This is recommended for the future work. There are

however, few studies who investigated the relationship between the size of the obstruction and its impact on the flow behavior.

Shafiqul *et al.* (2002) conducted experiments using PIV in a rib-roughened rectangular channel. They conducted experiments for two pitch-to-height ratios i.e. 10 and 20 at Reynolds numbers of 2000 and 7000. They compared the profiles of the mean streamwise velocity and the turbulent kinetic energy for the two pitch-to-height ratio cases at three locations corresponding to immediate upstream of the rib, at the rib and immediate downstream of the rib, to investigate how this ratio affects these properties. They observed negative velocity in the near wall region for the location downstream of the baffle, which is consistent with our results in figure 5.2. In the plots of Shafiqul *et al.* (2002), when the p/k ratio is low there is an excellent collapse of the profiles away from the wall whereas when the p/k ratio was higher the profiles did not collapse for both Reynolds numbers. In the present study, the mean velocity profiles collapse very well in the near-wall region, however, the difference in magnitude increased with the distance from the wall.

The plots of the turbulent kinetic energy show similar results as well. In the region away form the wall, the magnitude is highest for the upstream position regardless of Reynolds number. The profiles upstream and at the baffle collapse in the near wall region and gradually moves apart as the depth is increased. In the region close to the wall there is a sharp peak at the wall for the upstream profile after which the magnitude decreases to just

after the height of the baffle (or rib) and then peaks again. The downstream position peaks at the height of the baffle (or rib) and then decreases in both studies.

The results presented in the preceding section have shown that the flow characteristics are significantly modified by inserting a baffle inside the channel. Although the baffle was attached to the bottom wall of the channel and it obstructed almost 15% of the lower cross-section of the channel, the results show that it influenced the flow structure throughout the channel. Comparison of the turbulent characteristics in the presence and absence of the baffle has demonstrated that all turbulent characteristics are enhanced throughout the channel in the presence of the baffle. However, the most significant turbulence enhancement was observed in the region within a distance of two baffle heights from the bottom wall. The turbulence in this region was one to three orders of magnitude higher than that without a baffle. As turbulence contribute significantly to mixing and heat transfer, higher levels of turbulence indicates that the heat transfer across the wall would also be enhanced if heat is added or removed through the wall in the presence of a baffle. The results presented in this chapter are consistent with the results of Nasiruddin and Siddiqui (2006) who numerically investigated the impact of a baffle on the heat transfer rate inside a heat exchanger tube. They studied three different baffle orientations and found that for all orientations, the Nusselt number was enhanced by almost a factor of two in the presence of a baffle. They also found that the performance of the heat exchanger is optimal when the baffle is inclined towards the downstream end as the Nusselt number enhancement is almost the same with a minimal pressure loss. Thus, based on the results presented in the chapter it can be concluded that an insertion of a

baffle in a channel would significantly enhance the heat transfer through the wall while other operating conditions remain the same. That is, the effectiveness of a heat exchanger can be improved by installing a baffle at the heat exchanger wall.

Table 5.1: Properties for different cases; E, uncertainty in velocity measurements; Re_τ, Reynolds number based on friction velocity at the rough wall and half channel height.

Case	**I**	**II**	**III**
Re_τ	66	134	152
Δt (ms)	10	8	8
E (%)	10.78	4.67	3.82
u_* (cm/s)	0.19	0.38	0.44

(a)

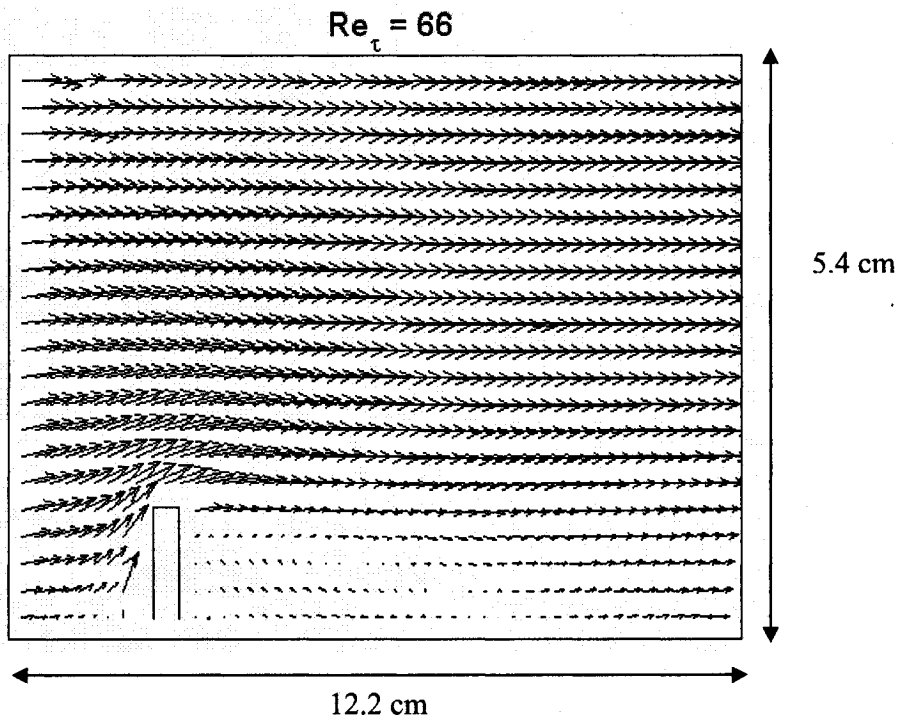

Figure 5.1: The temporally averaged instantaneous velocity vector field. (a) $Re_\tau = 66$ and (b) $Re_\tau = 152$.

(a)

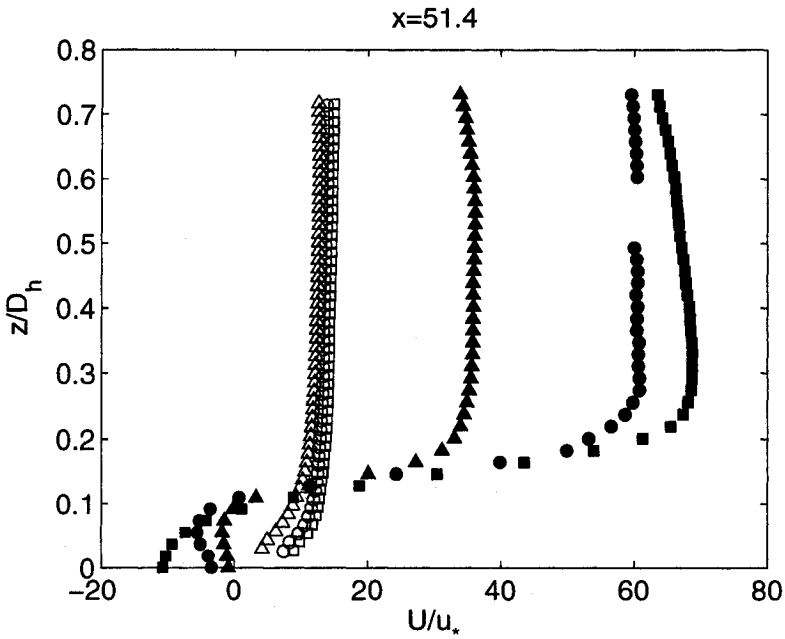

(b)

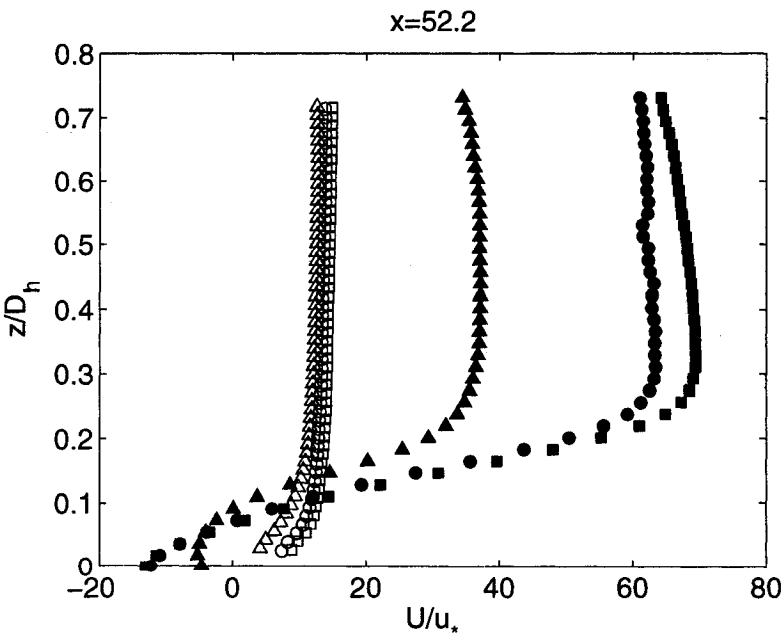

(c)

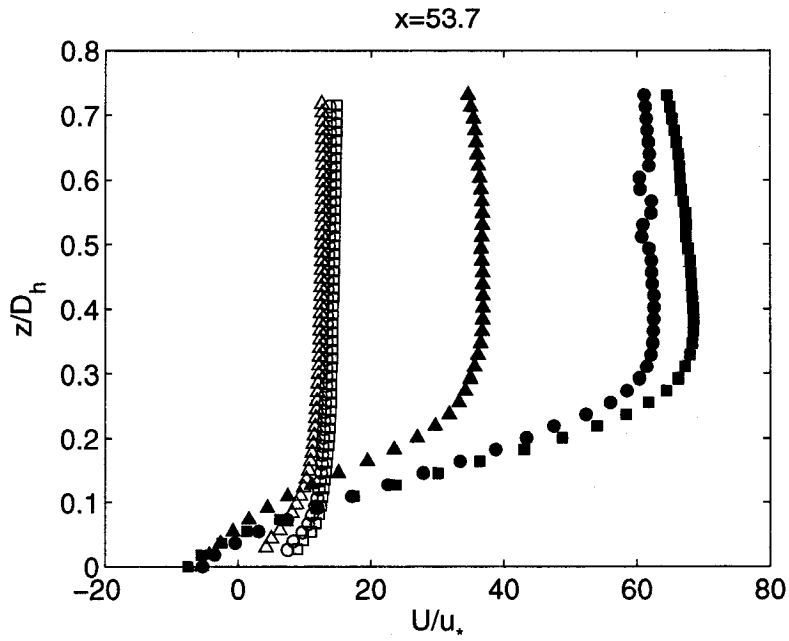

(d)

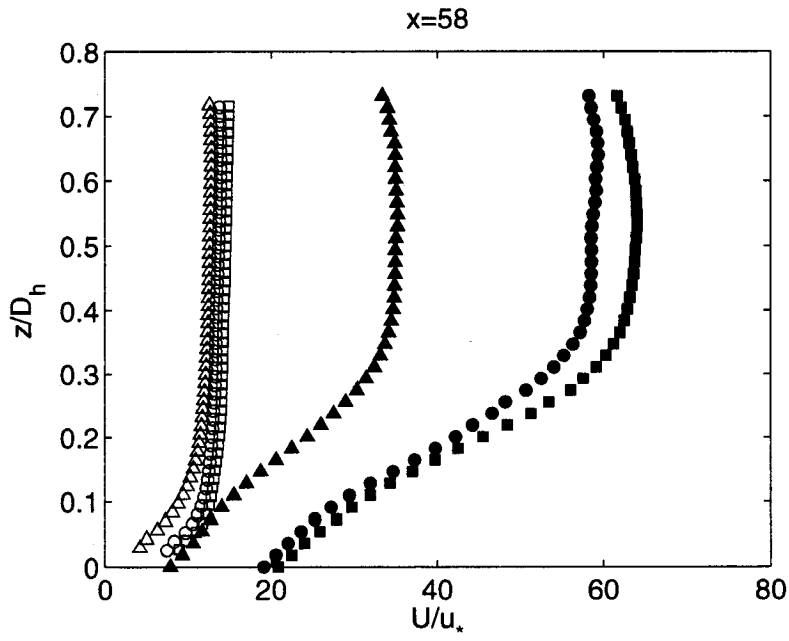

Figure 5.2: Vertical profiles of the mean streamwise velocity. Case I (-Δ-), Case II (-o-) and Case III (-□-). Open symbols: no-baffle case; closed symbols: baffle case. (a) x = 51.4cm, (b) x = 52.2cm, (c) x = 53.7cm and (d) x = 58cm.

(a)

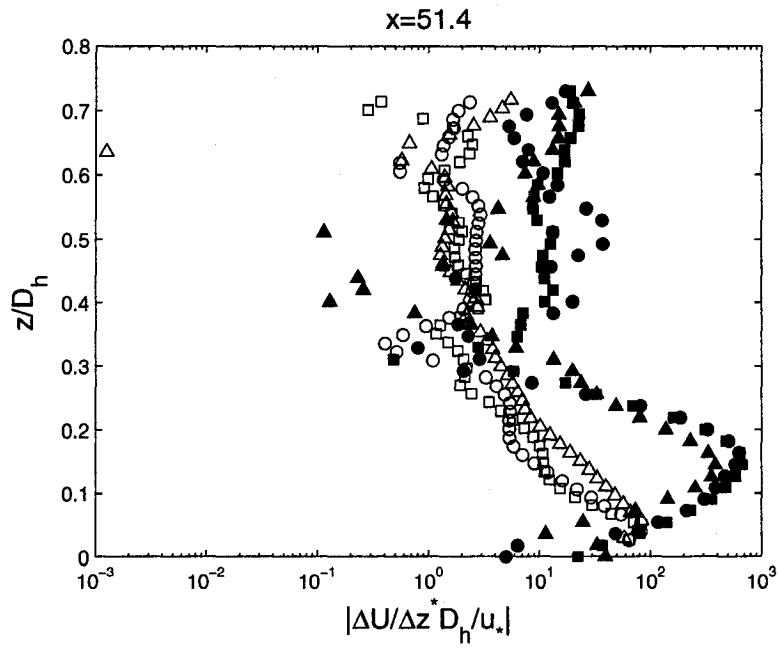

(b)

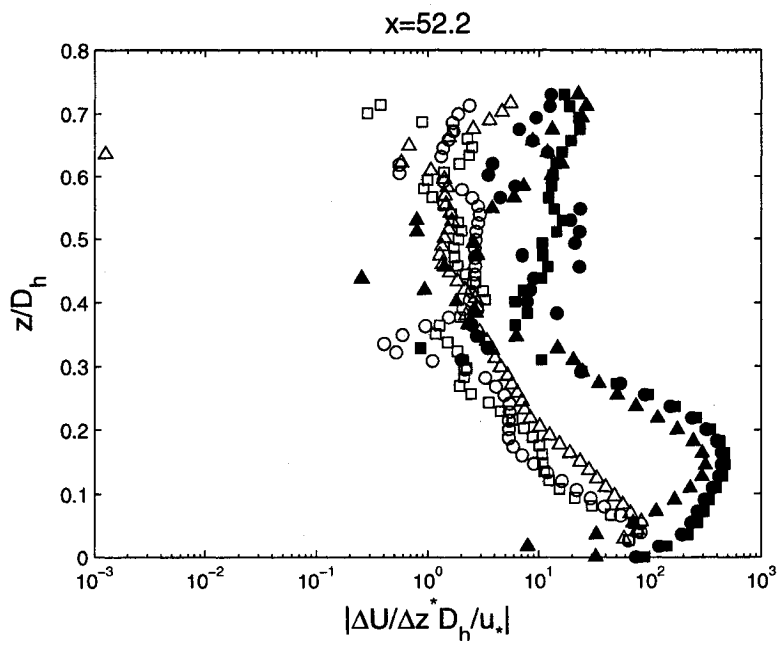

(c)

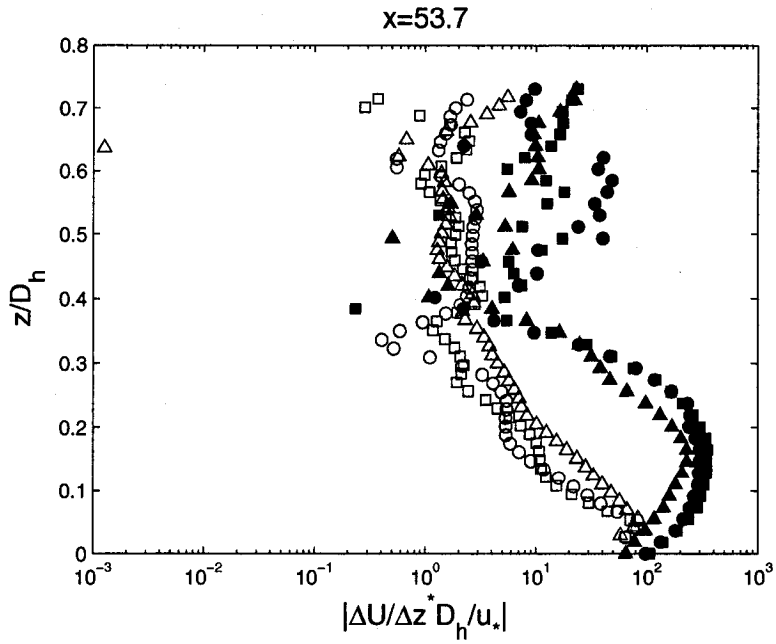

(d)

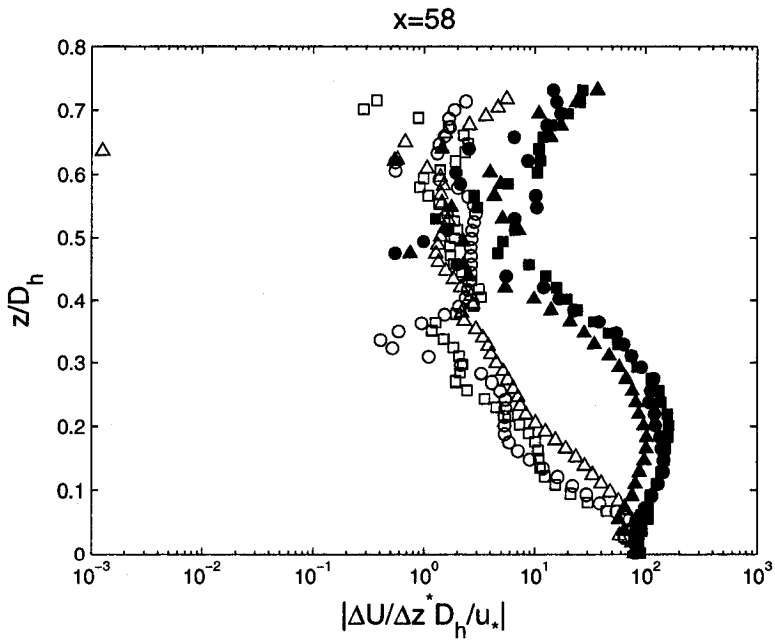

Figure 5.3: Vertical profiles of the mean streamwise velocity gradients ($\Delta U/\Delta z$). Case I (-Δ-), Case II (-o-) and Case III (-□-). Open symbols: no-baffle case; closed symbols: baffle case. (a) x = 51.4cm, (b) x = 52.2cm, (c) x = 53.7cm and (d) x = 58cm.

(a)

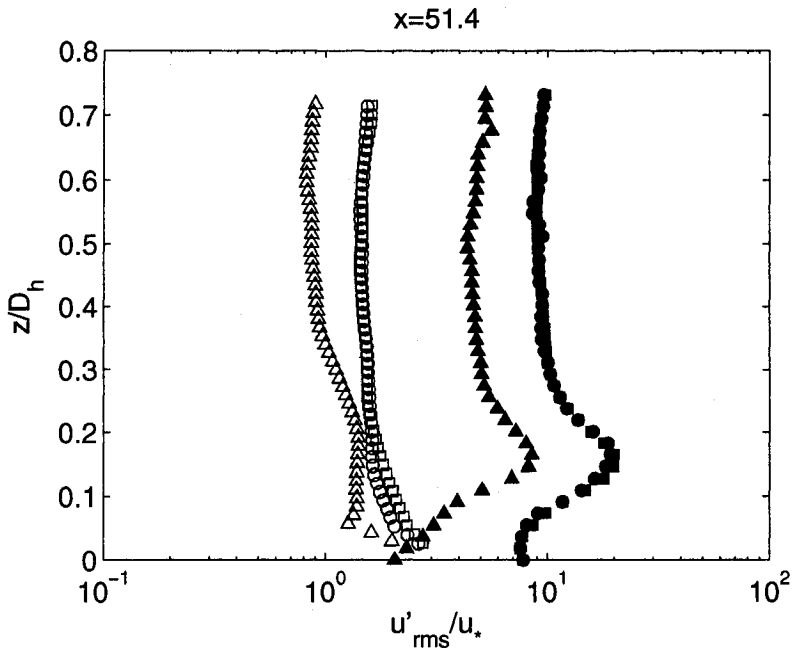

(b)

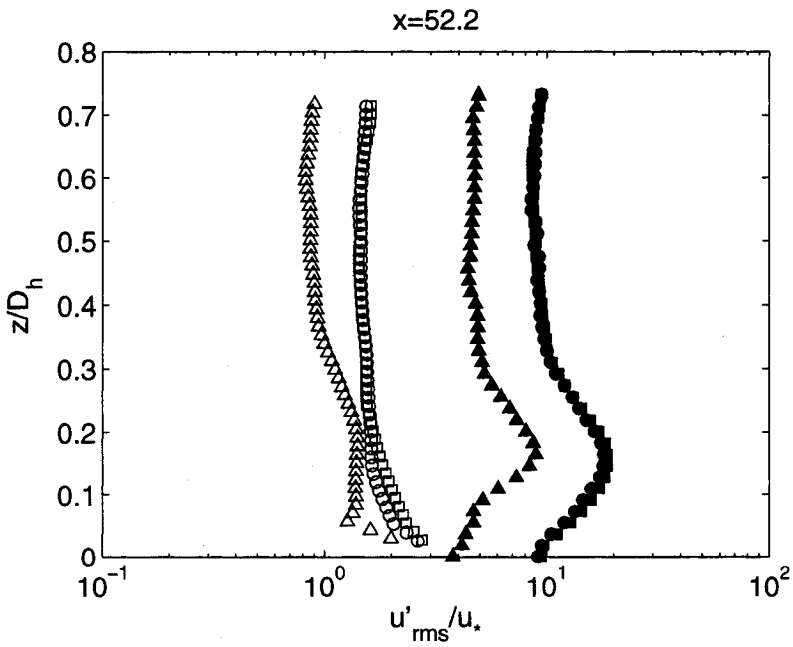

(c)

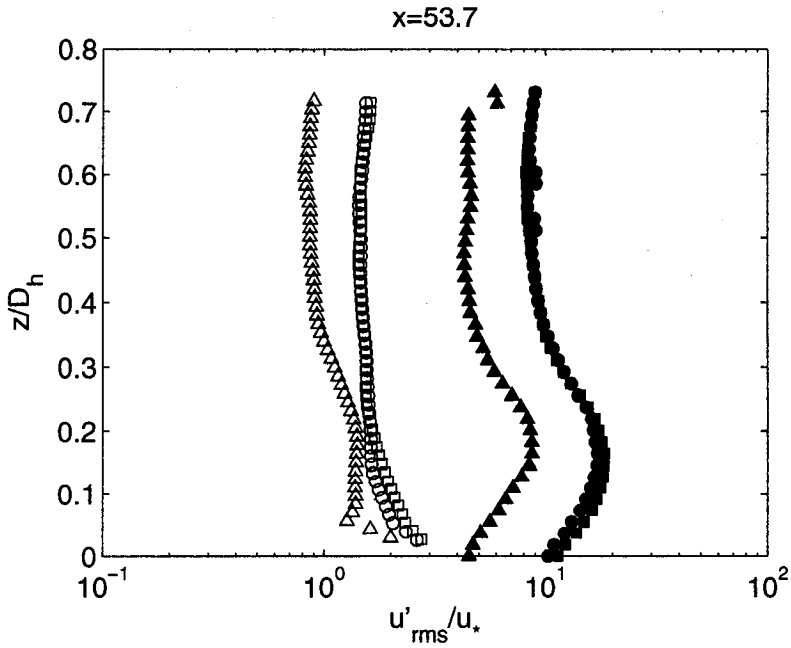

(d)

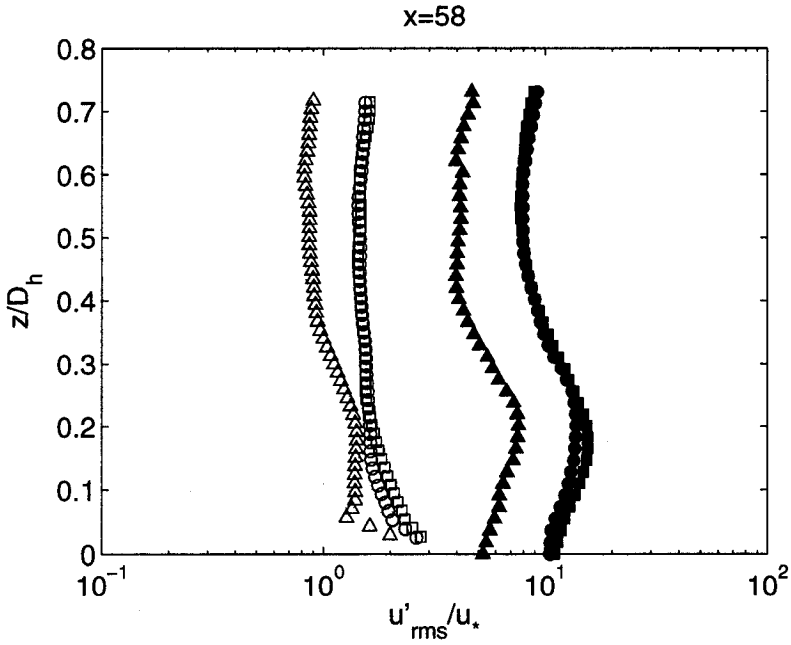

Figure 5.4: Vertical profiles of the RMS streamwise turbulent velocity. Case I (-Δ-), Case II (-o-) and Case III (-□-). Open symbols: no-baffle case; closed symbols: baffle case. (a) x = 51.4cm, (b) x = 52.2cm, (c) x = 53.7cm and (d) x = 58cm.

(a)

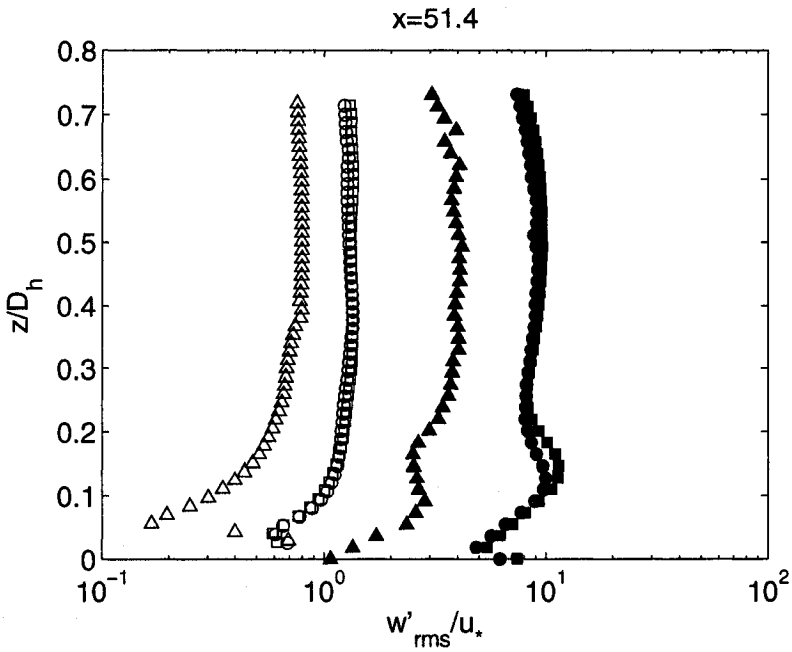

(b)

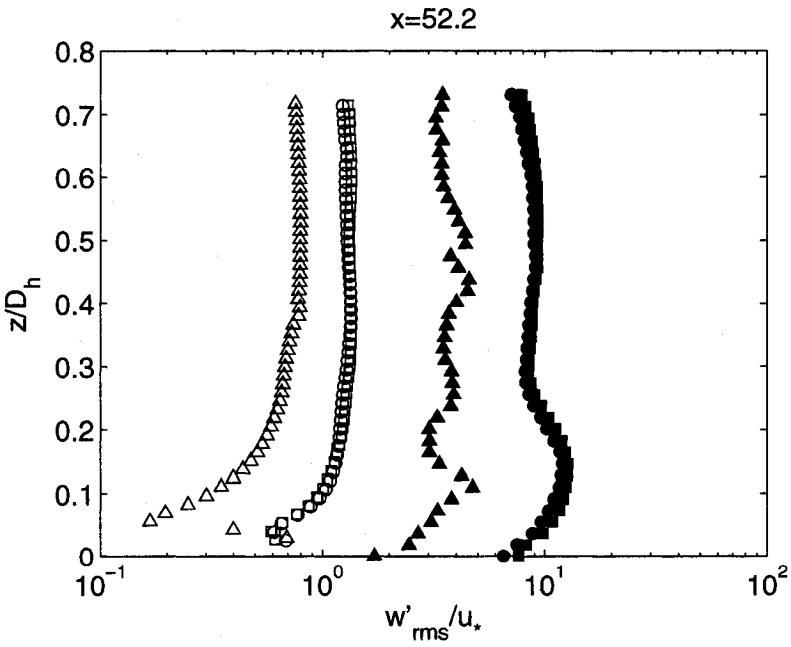

(c)

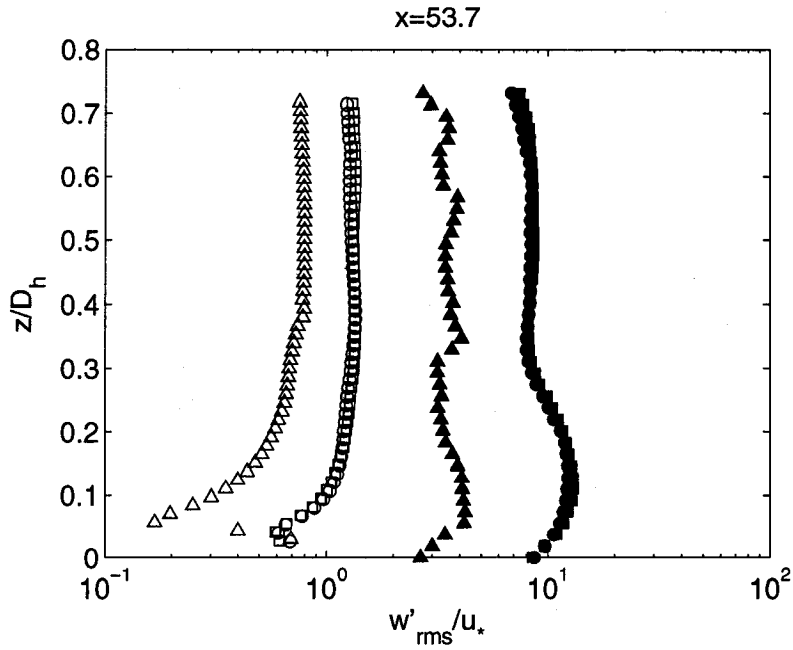

(d)

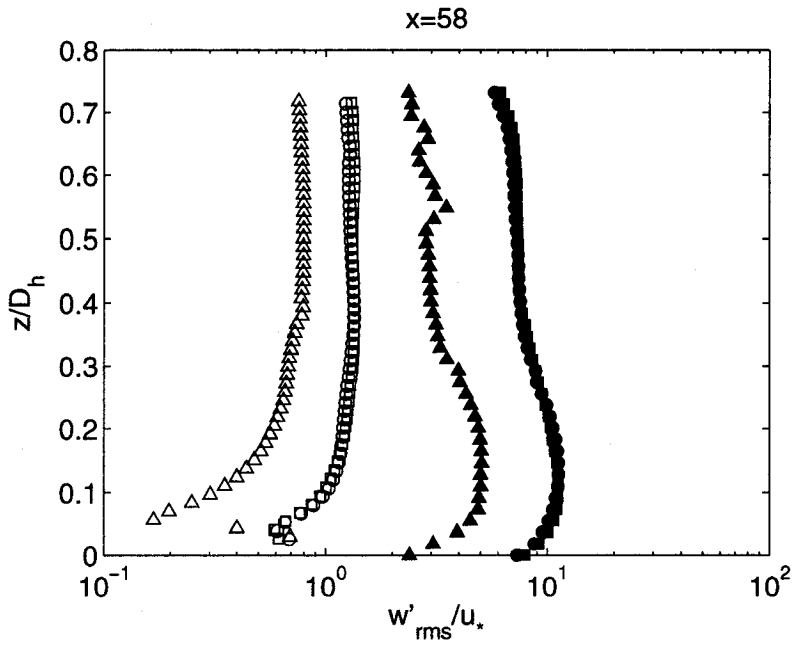

Figure 5.5: Vertical profiles of the RMS vertical turbulent velocity. Case I (-Δ-), Case II (-o-) and Case III (-□-). Open symbols: no-baffle case; closed symbols: baffle case. (a) x = 51.4cm, (b) x = 52.2cm, (c) x = 53.7cm and (d) x = 58cm.

(a)

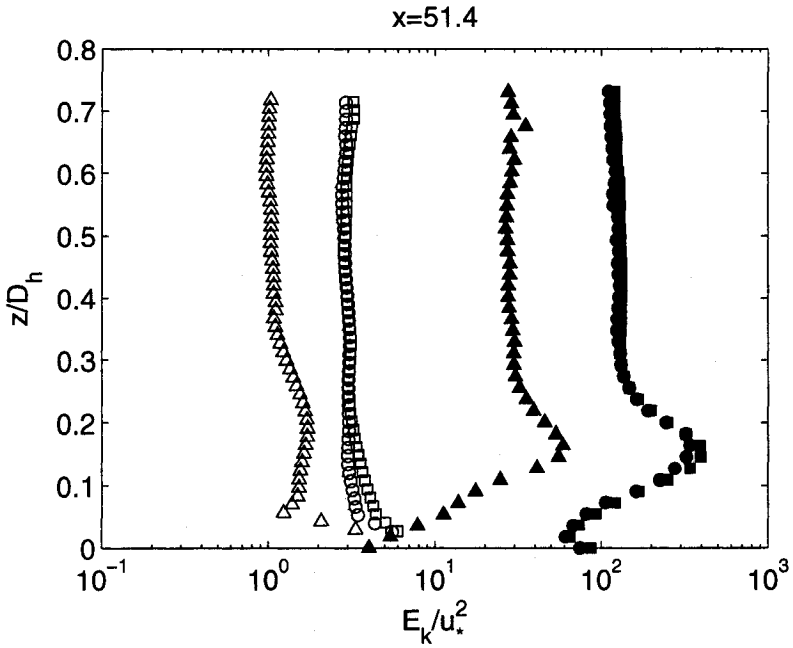

(b)

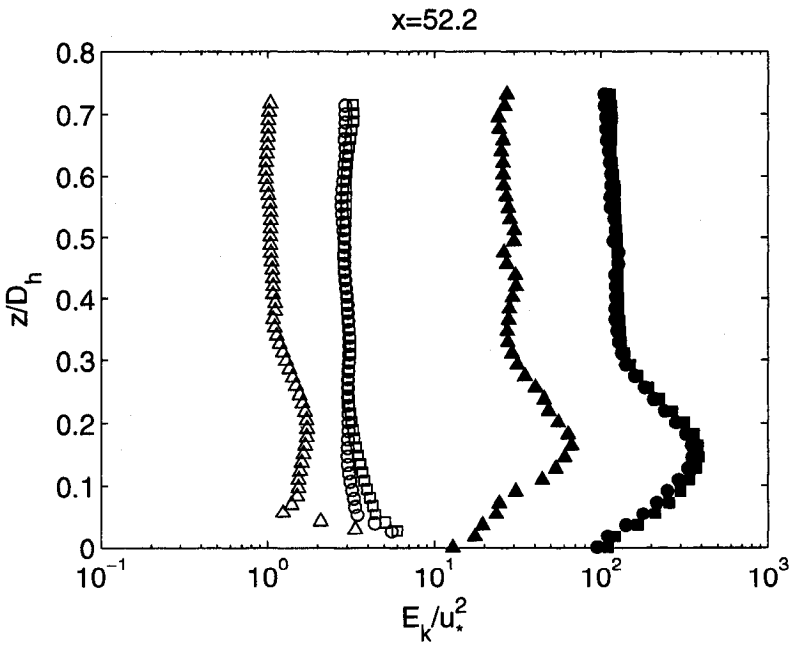

(c)

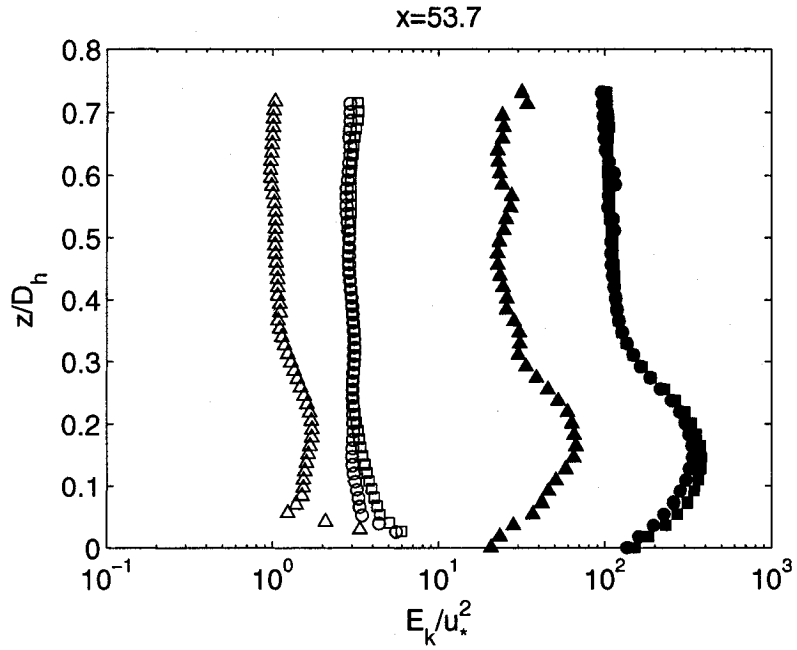

(d)

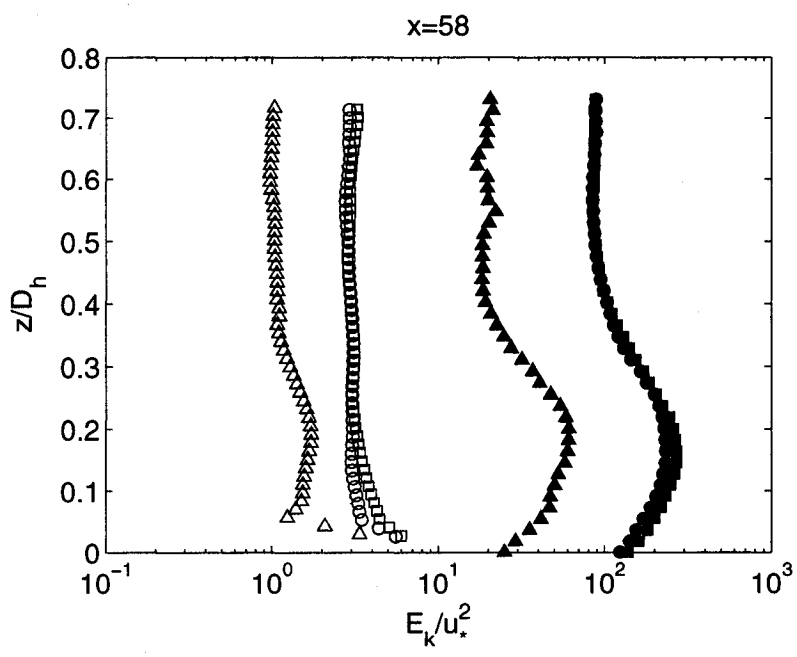

Figure 5.6: The mean kinetic energy is plotted versus the height from the wall. Case I (-Δ-), Case II (-o-) and Case III (-□-). Open symbols: no-baffle case; closed symbols: baffle case. (a) x = 51.4cm, (b) x = 52.2cm, (c) x = 53.7cm and (d) x = 58cm.

(a)

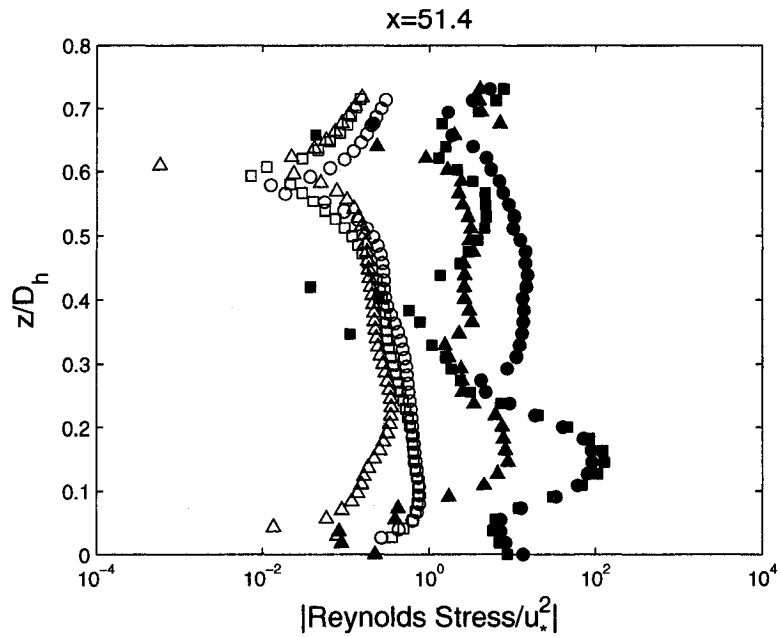

(b)

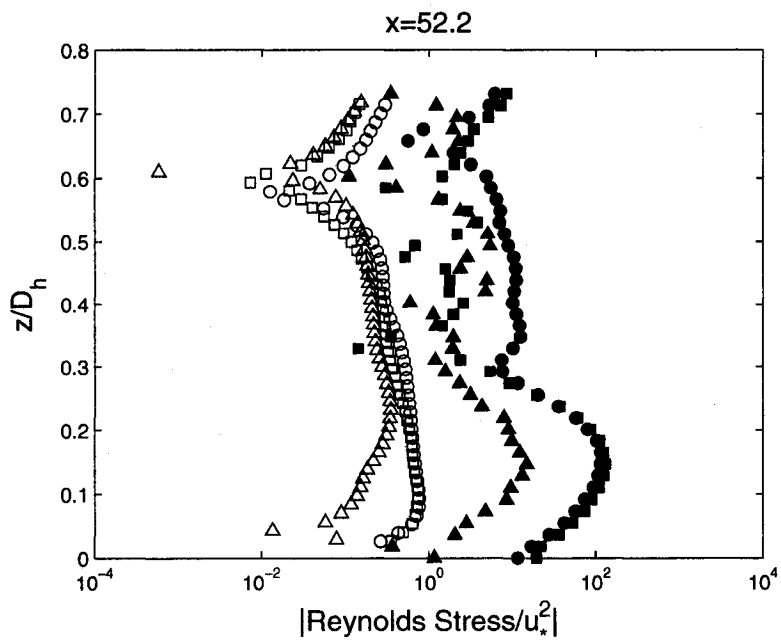

(c)

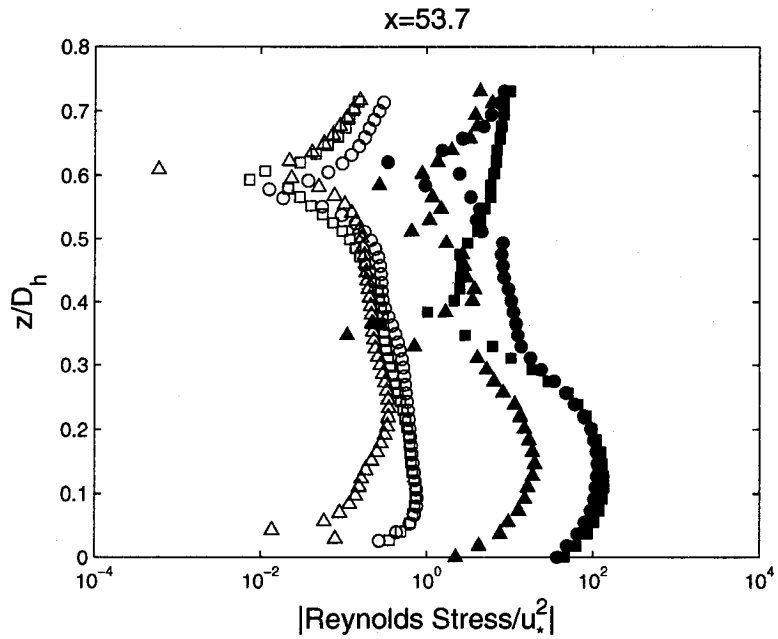

(d)

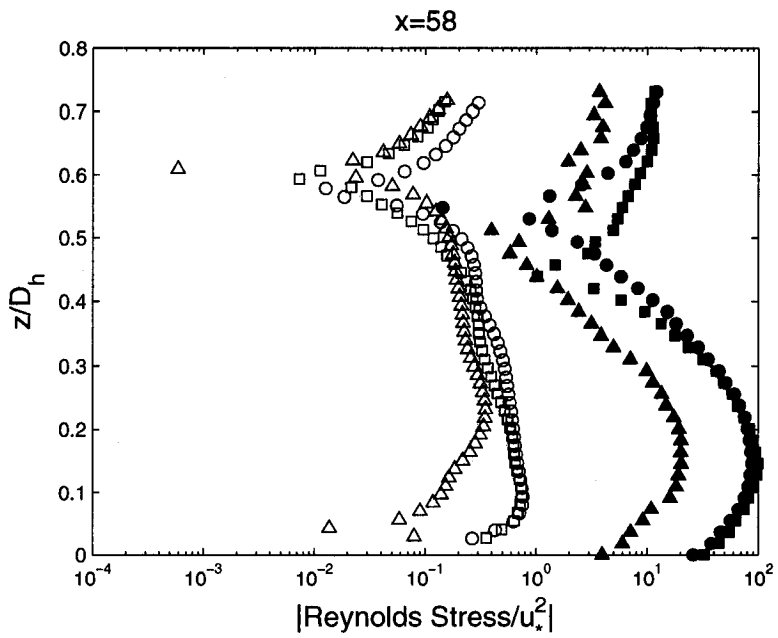

Figure 5.7: Vertical profiles of the Reynolds Stress. Case I (-Δ-), Case II (-o-) and Case III (-□-). Open symbols: no-baffle case; closed symbols: baffle case. (a) x = 51.4cm, (b) x = 52.2cm, (c) x = 53.7cm and (d) x = 58cm.

(a)

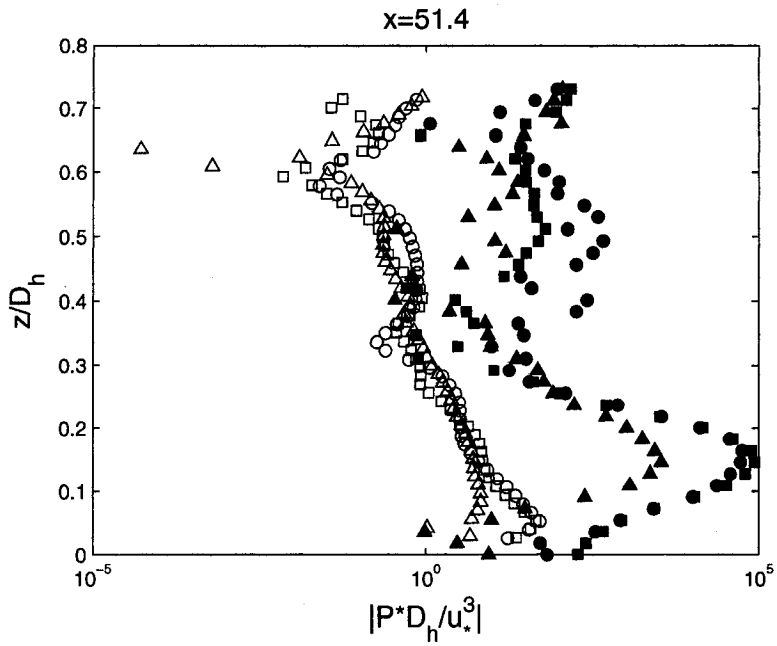

(b)

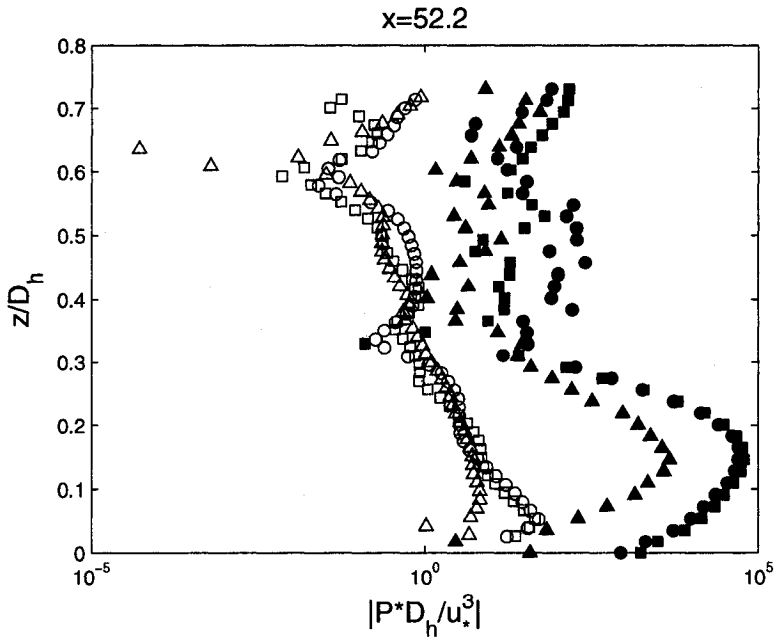

(c)

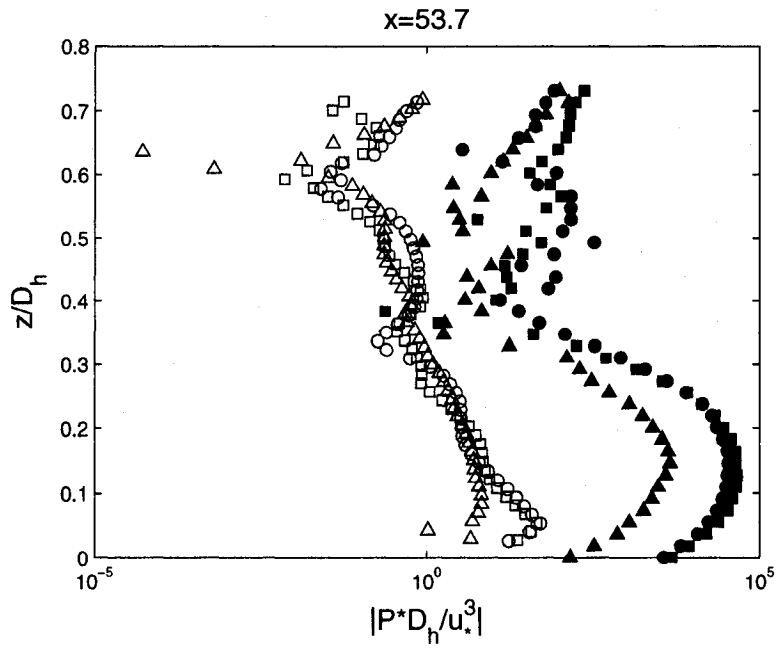

(d)

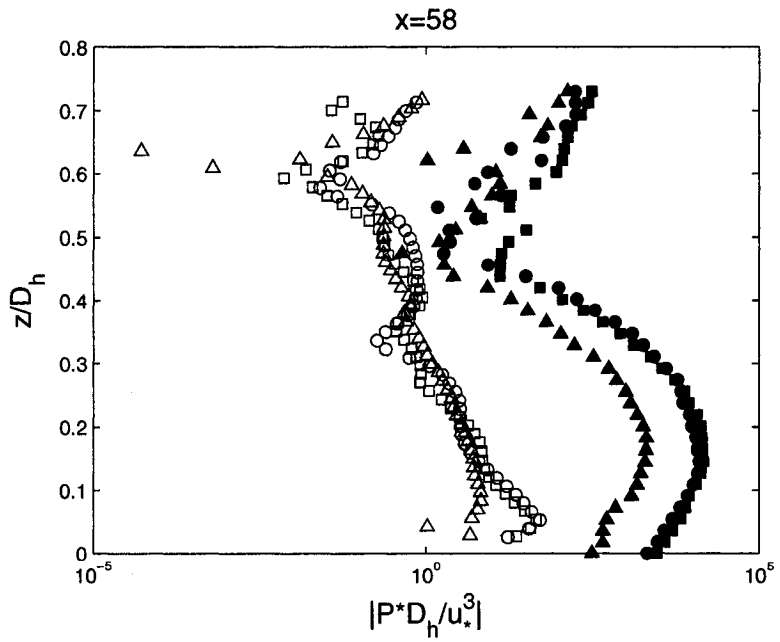

Figure 5.8: Vertical profiles of the rate of turbulent kinetic energy production. Case I (-Δ-), Case II (-o-) and Case III (-□-). Open symbols: no-baffle case; closed symbols: baffle case. (a) x = 51.4cm, (b) x = 52.2cm, (c) x = 53.7cm and (d) x = 58cm.

(a)

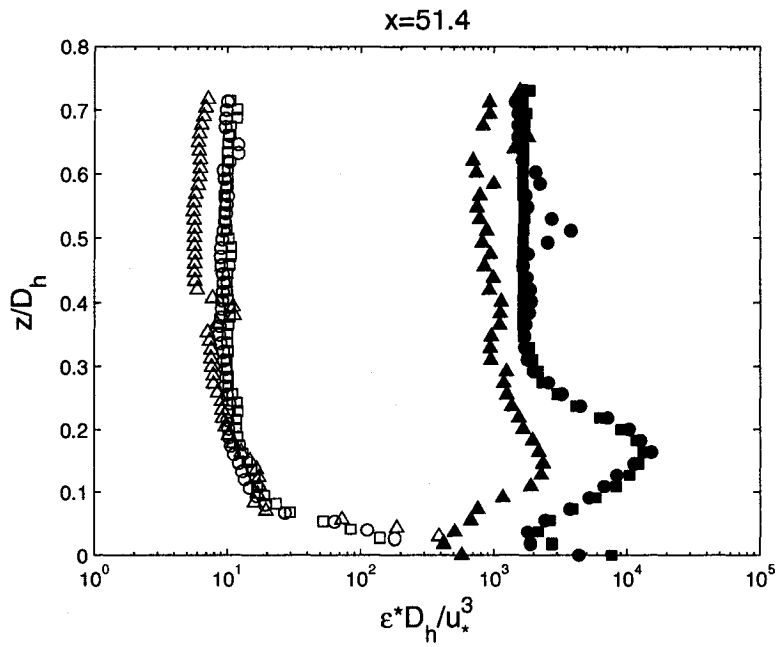

(b)

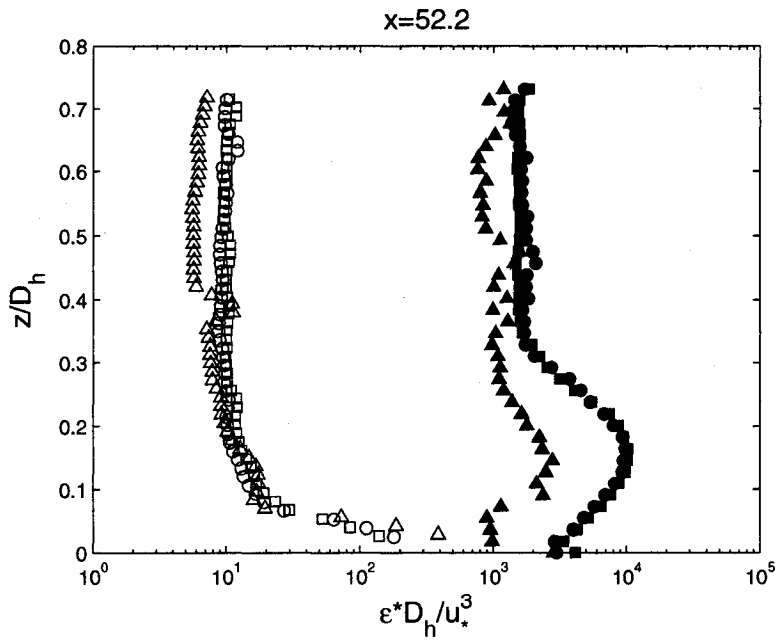

(c)

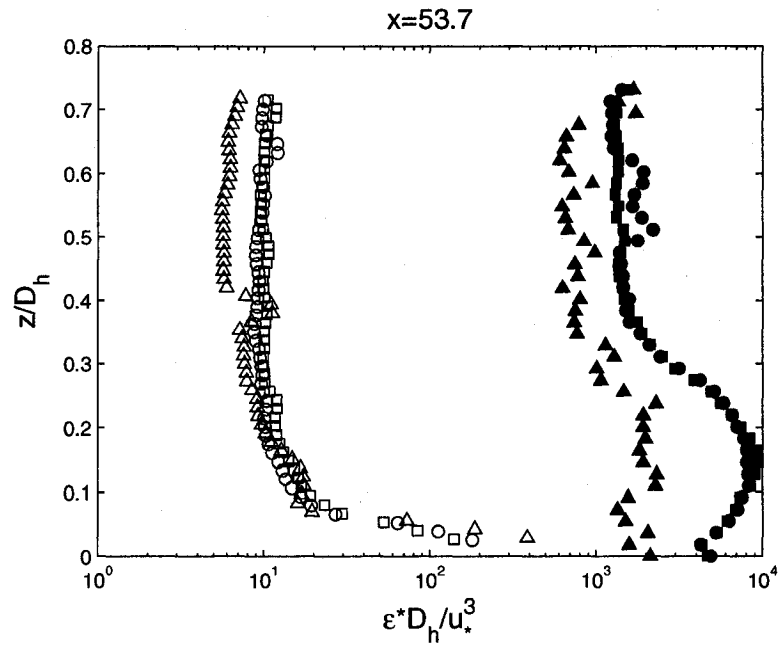

(d)

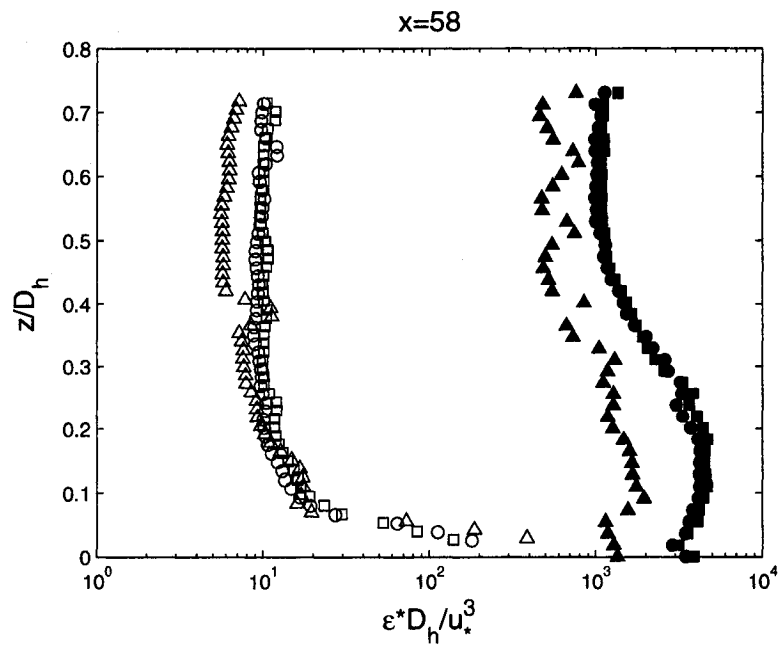

Figure 5.9: Case I (-Δ-), Case II (-o-) and Case III (-□-). Open symbols: no-baffle case; closed symbols: baffle case. (a) x = 51.4cm, (b) x = 52.2cm, (c) x = 53.7cm and (d) x = 58cm.

Chapter 6 – Summary and Conclusion

This thesis has reported on a series of laboratory experiments to investigate the flow field in a square channel. During these experiments, the two-dimensional velocity fields were measured using DPIV. The results presented in this thesis are unique because they provide the first insight into the structure of the flow fields in the near wall region from different perspectives.

The experimental setup and the measurement techniques were described in Chapter 2. The author designed the channel used in the experiments to achieve the thesis objectives. One special consideration for channel design was to allow optical access for the use of DPIV measurement technique. A detailed description of the DPIV technique was also presented. Using the DPIV technique, the velocity flow field is obtained. From this data the turbulent velocities can be computed and turbulent properties can also be obtained. The equations used to compute the two-dimensional properties are given at the end of Chapter 2. The author conducted the experiments, and processed and analyzed all datasets.

The results of phases one through three were presented in Chapters 3 through 5. Chapter 3 presented the results describing the flow behavior in a channel bounded by walls of different roughness. Previous studies investigated this issue with distinctly different surface conditions at both walls. That is, one wall was rough and the other was smooth in the absolute terms. The rough surface in these studies was specially fabricated using the square bars. However, no study investigated the impact of different roughness when both

roughness are natural. In addition, the impact of different roughness in a smooth channel has not been investigated. These issues are investigated for the first time in the present study. The results show that the relative difference in the roughness between the two walls has an impact on the overall flow behavior in the smooth channel. This impact is significant in some characteristics and negligible in others. However, the significant effects of wall roughness on all characteristics are observed in the inner region. The most significant effect of the difference in wall roughness was observed in the mean streamwise velocity distribution across the channel. In both laminar and fully developed turbulent regimes, the location of the maximum velocity was shifted from the channel centerline towards the smooth wall. This affects the flow behavior in the outer region and also resulted in an increased mass and momentum deficit near the rough wall. The profiles of Reynolds stress also show a shift of minima towards the smooth wall. The results also show that for the turbulent regime, the velocity gradients are negligibly small in the central region of the channel and the effect of different wall roughness is restricted only to the near-wall regions. The turbulent properties that are based on the velocity gradients, i.e. turbulent kinetic energy production and dissipation and turbulent vorticity also showed similar behavior. That is, the variation in these properties remained almost negligible in the central region. However, the extent to which these properties varied away from the wall was influenced by the wall roughness. Based on the results, it is also concluded that the investigation of the wall roughness on the flow characteristics is highly dependent on the roughness of the other bounding wall. Further experimental studies with higher roughness lengths are recommended to further explore this trend. The results also confirm the argument of Bakken *et al.* (2005) that the most accurate approach

to study the wall effects on the flow behavior, is by keeping the same roughness of both walls.

Chapter 4 presented the results of the second phase which was conducted to investigate the impact of wall heating on the flow structure in the near-wall region inside a square channel. The unique feature of this study is that it provided the first quantitative comparison of the mean and turbulent properties in the presence and absence of wall heating under same operating conditions. This provided a deep insight into the impact of wall heating on the near-wall flow behavior. The results have shown that when a flow is unstably stratified via heating through a bottom wall, both the mean and turbulent characteristics are affected. The results also shown that the impact of wall heating on the flow behavior is significantly different for laminar and turbulent flow regimes. It was found that when a flow that is originally laminar is heated, the mean streamwise velocity in the near-wall region is significantly increased and turbulence is generated in the flow. The turbulence production due to the mean shear in this flow regime is negligible and the turbulence production is predominantly due to buoyancy. Thus, a flow that is originally laminar becomes turbulent with the heat addition. However, when the flow is in the turbulent regime, addition of heat reduces the magnitudes of mean streamwise velocity and turbulent properties. The reduction in the magnitudes of turbulent properties in this flow regime is due to the working of turbulence against the buoyancy forces.

Chapter 5 presented the results of the final phase in which we experimentally studied the effect of a rectangular baffle on the flow behavior in the downstream region. Over the

past few decades several studies have investigated the impact of a baffle on the downstream flow structure. However, the unique feature of the present study is that it provided the first detailed quantitative comparison of the flow characteristics with and without baffle. The results show that the flow is most affected by the baffle in the immediate downstream region where strong longitudinal vortex is observed. However, the impact of the baffle was observed at all downstream locations within the measurement plane. Comparison of the turbulent characteristics in the presence and absence of the baffle has demonstrated that all turbulent characteristics are enhanced throughout the channel in the presence of the baffle. However, the most significant turbulence enhancement was observed in the region within a distance of two baffle heights from the bottom wall. The turbulence in this region was one to three orders of magnitude higher than that without a baffle. As turbulence contribute significantly to mixing and heat transfer, higher levels of turbulence indicates that the heat transfer across the wall would also be enhanced if heat is added or removed through the wall in the presence of a baffle.

6.1 Recommendations for Future Studies

The three phases considered in the present thesis investigated the flow behavior in a channel from different aspects. The results provided a detailed insight into the flow structure that would improve our understanding of the flow dynamics under these conditions. Each of these phases investigated the flow behavior at different Reynolds numbers, however, the controlling parameters in these experiments were fixed. That is, for the first phase, the flow behavior was investigated for one ratio of relative roughness.

In the second phase, the flow behavior was investigated for one heat flux condition and in the third phase, the investigations were made for one type of baffle. Following are some recommendations for the future work,

(i) The flow behavior should be investigated for different types of roughness to get comprehensive information about the impact of wall roughness on the flow behavior in a channel. This will lead to the development of specific wall roughness for flow control.

(ii) The impact of wall heating should be investigated for different heat fluxes. In addition to the flow measurements, simultaneous temperature measurements in the same plane should also be performed to understand velocity and temperature interactions.

(iii) Different shapes, sizes and orientations of vortex generators should be used and their impact should be quantified with respect to the case with no vortex generator.

(iv) A comprehensive study should be conducted that will consider combined effect of wall roughness, wall heating and vortex generator.

The most significant outcome of the recommended work would be the better understanding of the relationships between flow and thermal parameters, which will lead to the development of improved heat transfer models for more accurate heat transfer predictions. Eventually, this would lead to the development of more efficient heat exchanger.

References

Acharya S., Hibbs R. G., Chen Y. and Nikitopulos D.E., Mass/Heat Transfer in a ribbed passage with cylindrical vortex generators: the effect of generator-rib spacing. Journal of Heat Transfer, 122, 641-652, 2000.

Ameel T.A., Average effects of forced convection over a flat plate with an unheated starting length, Int. Comm. Heat Mass Transfer, vol. 24, pp.1113, 1997.

Anotonia R.A.and Krogstad P.-A, Turbulence structure in boundary layers over different types of surface roughness, Fluid Dynamics Research, vol. 28, pp.139-157, 2001.

Arya S.P.S , Buoyancy effects in a horizontal flat-plate boundary layer Journal of Fluid Mechanics, vol. 68, pp.321, 1975.

Ashrafian A. and Andersson, H. I., The structure of turbulence in a rod-roughened channel, International Journal of Heat and Fluid Flow, vol. 27, pp. 65-79, 2006.

Bakken O.M., Krogstad P.-A. Ashrafian A. and Andersson H.I., Reynolds number effects in the outer layer of the turbulent flow in a channel with rough walls, Physics of Fluids, vol. 17, 065101, 2005.

Bergstrom D. J., Kotey N.A. and Tachie M. F., The effects of surface roughness on the mean velocity profile in a turbulent boundary layer, Journal of Fluids Engineering, vol. 124, pp.664-6670, 2002.

Bhaganagar K., Kim J. and Coleman G., Effect of roughness on wall-bounded turbulence, Turbulence and Combustion, vol. 72, n 2-4 SPEC. ISS., pp 463-492, 2004.

Cowen E.A. and Monismith S.G., A hybrid digital particle tracking velocimetry technique, Experiments in Fluid, vol. 22, pp.199-211, 1997.

Doron P., Bertuccioli L., Katz J. and Osborn T.R., Turbulence Characteristics and Dissipation Estimates in the Coastal Ocean Bottom Boundary Layer from PIV Data. Journal of Physical Oceanography. vol. 31, pp.2108-2134, 2001.

Dupont, F., Gabillet, P. Bot, C., Experimental study of the flow in a compact heat exchanger channel with embossed-type vortex generators. Journal of Fluid Mechanics, vol. 125, pp. 701-709., 2003.

Eibeck P. A. and Eaton J. K., Heat transfer effects of a longitudinal vortex embedded in a turbulent boundary layer, Journal of Heat Transfer, Transactions ASME, vol. 109, pp. 16-24, 1987.

Fiebig M., Kallweit P., Mitra N., Tiggel B. S., Heat transfer enhancement and drag by longitudinal vortex generators in channel flow. Journal of Experimental Thermal Fluid Sciences, 4, pp. 103-114, 1991.

Fincham A.M. and Spedding G.R., Low cost, high resolution DPIV for measurement of turbulent fluid flow, Experiments in Fluid, vol. 23, pp.449-462, 1997.

Fukui K. and Nakajima M., Unstable stratification effects on turbulent shear flow in the wall region, International Journal of Heat Mass Transfer, vol. 28, pp. 2343, 1985.

Gajusingh S.T. and Siddiqui M.H.K., Flow behavior in a channel bounded by walls of different roughness, Experimental Thermal and Fluid Science, (Submitted, 2006A).

Gajusingh S.T. and Siddiqui M.H.K., The influence of wall heating on the flow structure in the near-wall region, Physics of Fluids, (Submitted, 2006B).

Hanjalic K. and Launder B.E., Fully developed asymmetric flow in a plane channel Journal of Fluid Mechanics, vol. 51, pp. 301-335, 1972.

Hirota M., Fujita H., Yokosawa H., Nakai H. and Itoh H., Turbulent heat transfer in a square duct, International Journal of Heat Fluid Flow, vol. 18, pp.170-180, 1997.

Huser A. and Biringen S., Direct numerical simulation of a turbulent flow in a square duct, Journal of Fluid Mechanics, vol. 257, pp.65-96, 1993.

Ichimiya K. and Yamada Y., Mixed convection in a horizontal square duct with local inner heating, Heat Transfer – Asian Research, vol. 34, pp.160, 2005.

Keirsbulck L. Labraga L., Mazouz A. and Tournier C., Surface roughness effects on turbulent boundary layer structures, Journal of Fluids Engineering, vol. 124, pp.127-135, 2002.

Kim J., Moin P. and Moser R., Turbulence statistics in fully developed channel flow at low Reynolds number. Journal of Fluid Mechanics, vol. 177, pp.133-166, 1987.

Krogstad P.-A. and Anotonia R.A., Surface roughness effects in turbulent boundary layers, Experiments in Fluids, vol. 27, pp.450-460, 1999.

Krogstad P.-A., Anotonia R.A. and Browne L.W.B., Comparison between rough-and smooth-wall turbulent boundary layers, Journal of Fluid Mechanics, vol. 245, pp.599-617, 1992.

Krogstad, P.-A., Andersson H.I., Bakken O.M., Ashrafian A., An experimental and numerical study of channel flow with rough walls, Journal of Fluid Mechanics, vol. 530, pp. 327-352, 2005.

Lee S.-J. and Lee S.-H., Flow field anaylsis of a turbulent boundary layer over a riblet surface, Experiments in Fluids, vol. 30, pp.153-166, 2001.

Leonardi S., Orlandi P., Djenidi L. and Antonia R.A., Structure of turbulent channel flow with square bars on one wall, International Journal of Heat and Fluid Flow, vol. 25, pp. 384-392, 2004.

Leonardi S., Orlandi P., Smalley R.J., Djenidi L. and Antonia R.A., Direct numerical simulations of turbulent channel flow with transverse square bars on one wall, Journal of Fluid Mechanics, vol. 491, pp. 229-238, 2003.

Lin C. N., Jang J. Y., Conjugate Heat Transfer and Fluid Flow Analysis in fin tube heat exchangers with wave-type vortex Generators, Journal of Enhanced Heat Transfer, vol. 9, pp.123-136, 2002.

Miyake Y., Tsujimoto K. and Nakaji M., Direct numerical simulation of rough-wall heat transfer in a turbulent channel flow, International Journal of Heat and Fluid Flow, vol. 22, 2001, pp. 237-244

Nasiruddin S. and Siddiqui M. H. K., Heat transfer augmentation in a heat exchanger tube using a baffle, International Journal of Heat and Fluid Flow, (in press, published online June 15th 2006).

Nicholl C.I.H., Some dynamical effects of heat on a turbulent boundary layer, Journal of Fluid Mechanics, vol. 40, pp. 361, 1970.

O'Brien J. E., Sohal M.S., Wallstedt P. C., Local heat transfer and pressure drop for finned-tub heat exchanger using oval tubes and vortex generators J. Heat Transfer, vol. 126, pp.826-835. 2004.

Pauley W. R. and Eaton J. K., Experimental study of the development of longitudinal vortex pairs embedded in a turbulent boundary layer, AIAA Journal, vol. 26, pp. 816-823, 1988.

Perry A.E. and Hoffmann P.H., An experimental study of turbulent convective heat transfer from a flat plate, Journal of Fluid Mechanics, vol. 77, pp.355, 1976.

Perry A.E., Lim K.L. and Henbest S.M., An experimental study of the turbulence structure in smooth- and rough-wall boundary layers, Journal of Fluid Mechanics, vol. 177, pp.437-466, 1987.

Pope S.B., Turbulent Flows, Cambridge University Press, New York, N.Y., pp.269-286, 315, 2000.

Prasad A.K., Adrian R.J., Landreth C.C. and Offutt P.W., Effect of resolution on the speed and accuracy of particle image velocimentry interrogation, Experiments in Fluid, vol. 13, pp.105-116, 1992.

Romano G.P., PIV and LDA velocity measurements near walls and in the wake of a delta wing, Journal of Optics and Lasers in Engineering, vol.16, pp. 293-309, 1992.

Rued K., Murthy J.Y. and Metzger D.E., Turbulent convection heat transfer at the corner intersection of heated and unheated walls in a square channel, ASME, HTD, vol. 87, pp.49, 1987.

Shafiqul I, M., Haga K., Kaminaga M., Hino R. and Monde, M., Experimental analysis of turbulent flow structure in a fully developed rib-roughned rectangular channel with PIV, Experiments in Fluids, vol. 33, pp. 296-306, 2002.

Siddiqui M. H. K., Loewen M.R., Richardson C., Asher W.E. and Jessup A.T., Simultaneous particle image velocimetry and infrared imagery of microscale breaking waves, Physics of Fluids, vol. 13, pp.1891, 2001.

Siegel D.A. and Plueddemann A.J., The motion of a solid sphere in an oscillating flow: an evaluation of remotely sensed Doppler velocity estimates in the sea, Journal of Atmospheric Oceanic Technology, vol. 8, pp. 296-304, 1991

Snyder S.D., Some measurements of particle velocity autocorrelation functions in a turbulent flow, Journal of Fluid Mechanics, vol. 48, pp. 41-71, 1971.

Tiggelbeck S., Mitra N. and Fiebig M., Flow Structure and Heat Transfer in a Channel With Multiple Longitudinal Vortex Generators, Experimental Thermal and Fluid Science, vol. 5, pp. 425-436, 1992.

Tiwari S., Prasad P. L. N., Biswas G., A numerical study of heat transfer in fin-tube heat exchangers using winglet-type vortex generators in common-flow down configuration, Progress in computational fluid dynamics, vol. 3, 32-41, 2003.

Townsend A.A., The Structure of Turbulent Shear Flow, Cambridge University Press, Cambridge, 1976

Townsend A.A., The effects of radioactive transfer on turbulent flow of a stratified fluid, Journal of Fluid Mechanics, vol. 4, pp.361, 1958.

Tsay Y.-L., Chang T.S., Cheng J.C., Heat transfer enhancement of backward-facing step flow in a channel by using baffle installed on the channel wall, Acta Mechanica, vol. 174, pp.63-76., 2005.

Turner J.S., *Buoyancy Effects in Fluids*, (Cambridge University Press, New York, N.Y., 1973.

Wroblewski D. E. and Eibeck, P. A., Measurements of turbulent heat transport in a boundary layer with an embedded streamwise vortex. International Journal of Heat and Mass Transfer, vol. 34, pp. 1617-1631, 1991

Appendix A

Error Estimation for the DPIV measurements

The total error in the DPIV measurements is the sum of the errors due to gradients, particle density, particle diameter, out-of-plane motion, dynamic range, peak locking and AGW interpolation (Cowen and Monismith 1997). The non-dimensional particle diameter in the present study was 0.14 pixels. Particles smaller than one pixel always occupy one pixel area in a DPIV image. As a result, they are not able to resolve the true position of the particle within a pixel.

Ideally, the duration of the light pulse should be as small as possible to avoid imaging streaky particles. One of the main consequences of these streaky images is that the shape of the particle will no longer be Gaussian and this will affect the shape of the correlation peak. The combined effect of the smaller particle diameter and non-Gaussian particle image shape was to increase the peak locking errors.

Peak locking refers to the bias that occurs when the estimated location of the correlation peak is shifted towards the nearest integer value. According to Fincham and Spedding (1997) peak locking occurs in any type of Image Velocimetry technique where sub-pixel determination of the correlation peak is attempted. However, it can be minimized by using a suitable peak-fitting scheme. We tested several different sub-pixel peak fitting schemes including the three-point Gaussian, parabolic and center-of-mass estimators and

found that the three-point Gaussian estimator performed the best (Cowen and Monismith 1997). We found using the three-point Gaussian estimator that on average 15% of the vectors were affected by peak locking, which is consistent with Fincham and Spedding's (1997) results.

The largest errors are expected to occur along the wall surface since the velocity gradients are largest here. We used the results of Cowen and Monismith (1997) and Prasad *et al.* (1992) to estimate the errors in the DPIV data. The errors were estimated using the raw displacement data. A detailed step-by-step procedure to estimate errors in the DPIV data is given below.

1. The mean values of the largest velocity gradients in the streamwise and vertical directions were computed from the raw DPIV data. The mean streamwise velocity gradient was 1% and the mean vertical velocity gradient was zero. The errors were estimated for the streamwise velocity on the basis of the mean streamwise velocity gradient.
2. The errors due to velocity gradient were estimated using figure 5(e) in Cowen and Monismith (1997). This figure gives the approximate errors due to velocity gradients and is based on a particle size of 2.0 pixels. The total error due to velocity gradients is the sum of the mean and RMS errors. The errors due to velocity gradient were estimated to be,

$$\varepsilon_u = 0.08 \text{ pixels (based on 1\% gradient)} \qquad \text{(A.1)}$$

where ε_u is the errors associated with the streamwise velocity.

3. As mentioned earlier, the particle diameter in the present study was 0.14 pixels, therefore, the errors due to smaller particle diameter should be accounted for. We used figure 5(a) in Cowen and Monismith (1997), which is the plot of the errors as a function of the particle size. The errors due to a particle diameter of 1.0 pixel were estimated, since this was the smallest particle diameter that Cowen and Monismith (1997) considered. The errors for a particle diameter of 1.0 pixel and the same velocity gradients were,

$$\varepsilon_u = 0.09 \text{ pixels} \qquad \text{(A.2)}$$

The errors corresponding to a particle diameter of 0.14 pixels were estimated using figure 13 in Prasad *et al.* (1992), which shows the variation in the bias (peak locking error) and RMS errors as a function of particle diameter. Using this figure, we estimated that the errors associated with a particle diameter of 0.14 pixels would be 40% larger than the errors associated with a particle diameter of 1.0 pixel. The estimates of Prasad *et al.* (1992) were based on a center of mass peak-fitting scheme, which is the scheme most susceptible to peak-locking errors (Fincham and Spedding 1997). The errors in the present case would be smaller since we used a three-point

4. Gaussian estimator, which is much less susceptible to peak locking than the center of mass scheme (Cowen and Monismith 1997). Therefore, a more realistic estimate of the increase in the errors is 20% due to the small particle size. Hence, the final error estimate based on a 20% increase in errors was,

$$\varepsilon_u = 0.179 \text{ pixels} \qquad \text{(A.3)}$$

5. The in-plane vertical displacement based on the mean and standard deviation of the vertical displacement was estimated to be,

$$W = \overline{w} + \sigma_w = 0.3353 \text{ pixels} \approx 19.8 \text{ μm} \quad \text{(A.4)}$$

The out-of-plane motion was expected to be less than or equal to the vertical displacement. Since the thickness of the laser light sheet was approximately 200 μm, the out-of-plane motion in the present case was assumed to be negligible.

6. The error due to AGW interpolation was estimated from figure 5(f) in Cowen and Monismith (1997) and it was 0.08 pixels.

Thus the total error in the streamwise velocity was estimated to be,

$$\varepsilon_u = 0.099 + 0.08 = 0.179 \text{ pixels} \quad \text{(A.5)}$$

This RMS error expressed in velocity units is,

$$\varepsilon_u = 0.106 \text{ cm s}^{-1} \quad \text{(A.6)}$$

We assumed that the errors in the vertical velocity (w) were the same as the errors in the streamwise velocity (u). Since the larger gradients in the vertical direction (i.e. $\partial u / \partial z$) will produce errors in both u and w. Therefore, the error in V, where $V = \sqrt{u^2 + w^2}$ is,

$$\varepsilon_V = 0.15 \text{ cm s}^{-1} \quad \text{(A.7)}$$

The errors in the vorticity measurements were estimated from the errors in the velocity measurements. The vorticity (ω) is given by,

$$\omega = \frac{\partial u}{\partial z} - \frac{\partial w}{\partial x} \quad \text{(A.8)}$$

where, $\partial u / \partial z$ and $\partial w / \partial x$ are the streamwise and vertical velocity gradients, respectively. The streamwise velocity gradient can be written as,

$$\frac{\partial u}{\partial z} = \frac{\Delta u}{\Delta z} \tag{A.9}$$

where, $\Delta u = u_1 - u_2$, that is, the difference in the streamwise velocities at two grid points and, Δz is the vertical distance between the two grid points. We used the central difference method to compute vorticity; therefore, Δz in the present case is equal to 0.189 cm (correspond to 32 pixels × 0.0059 cm/pixel). The variance of the errors (ε^2) in Δu can be estimated as,

$$\varepsilon^2(\Delta u) = \varepsilon^2(u_1) + \varepsilon^2(u_2) = 2\,\varepsilon^2(u) = 2\,(0.106)^2 = 0.022 \text{ cm}^2 \text{ s}^{-2} \tag{A.10}$$

where $\varepsilon^2(\Delta u)$, $\varepsilon^2(u_1)$ and $\varepsilon^2(u_2)$ are the variance of the errors in Δu, u_1 and u_2, respectively (Kennedy and Neville 1976). The variance of the errors in $\partial u / \partial z$ is then given by,

$$\varepsilon^2(\Delta u/\Delta z) = \varepsilon^2(\Delta u)/\Delta z = 0.022/0.189 = 0.116 \text{ s}^{-2} \tag{A.11}$$

Since we assumed the magnitude of the errors in w were equal to those in u, the variance of the errors in $\partial w / \partial x$ is given by,

$$\varepsilon^2(\Delta w/\Delta x) = \varepsilon^2(\Delta w)/\Delta x = 0.022/0.189 = 0.116 \text{ s}^{-2} \tag{A.12}$$

where Δx is equal to 0.189 cm (32 pixels × 0.0059 cm/pixel). The variance of the errors in the vorticity, $\varepsilon^2(\omega)$, is then given by,

$$\varepsilon^2(\omega) = \varepsilon^2(\Delta u/\Delta z) + \varepsilon^2(\Delta w/\Delta z) = 0.232 \text{s}^{-2} \tag{A.13}$$

Thus, the RMS error in the vorticity, $\varepsilon(\omega)$, is given by,

$$\varepsilon(\omega) = \sqrt{\varepsilon^2(\omega)} = 0.482 \text{ s}^{-1} \tag{A.14}$$

Hence, the average RMS errors in the instantaneous velocity and vorticity estimates are ± 0.15 cm s^{-1} and ± 0.482 s^{-1}, respectively.